DISCLAIMER

INL/RPT-25-85835
ANL/NSE-25/28

Fluoride-Cooled High-Temperature Pebble-Bed Reactor Reference Plant Model Updates

JUNE 2025

Javier Ortensi,
David Reger, and
Mustafa K. Jaradat

Idaho National Laboratory

Gang Yang,
Ling Zou, and
Rui Hu

Argonne National Laboratory

Cole Takasugi

U.S. Nuclear Regulatory Commission

Idaho National Laboratory

Argonne NATIONAL LABORATORY

Battelle Energy Alliance manages INL for the U.S. Department of Energy's Office of Nuclear Energy

INL/RPT-25-85835 ANL/NSE-25/28

Fluoride-Cooled High-Temperature Pebble-Bed Reactor Reference Plant Model Updates

Javier Ortensi,
David Reger, and
Mustafa K. Jaradat
Idaho National Laboratory
Gang Yang,
Ling Zou, and
Rui Hu
Argonne National Laboratory
Cole Takasugi
U.S. Nuclear Regulatory Commission

June 2025

Idaho National Laboratory
Reactor System Design and Analysis
Idaho Falls, Idaho 83415

http://www.inl.gov

Prepared for the
Office of Nuclear Regulatory Research
U. S. Nuclear Regulatory Commission
Washington, D. C. 20555
Task Order No.:
31310019F0015 and 31310021F0005

Page intentionally left blank

ABSTRACT

This work presents the latest improvements to, and investigations performed with, the Fluoride-Cooled High-Temperature Pebble-Bed Reactor reference plant models for the United States Nuclear Regulatory Commission. These models, developed with the Comprehensive Reactor Analysis Bundle, or BlueCRAB, serve as the foundation for the future development of detailed design evaluation models based on license applications. BlueCRAB is the code suite proposed for non-light-water reactor systems safety analyses, and it incorporates various simulation tools developed by the Nuclear Energy Advance Modeling and Simulation program, including the Griffin code for reactor physics, the Pronghorn and SAM codes for core thermal fluids, the BISON code for solid conduction and fuel performance, and the SAM code for system analysis. The primary objective of this work is to assess the level of readiness of BlueCRAB for modeling fluoride-cooled high-temperature pebble-bed reactors. We first developed numerical models in BlueCRAB that include the key physics for this technology, ensuring an adequate level of fidelity for modeling the core performance during accident scenarios. This was followed by simulation of transient scenarios, two loss-of-forced-cooling events (one protected and one unprotected), and two control rod withdrawal events (one delayed and one prompt supercritical reactivity insertion). The analysis includes comparisons between the 2-D thermal fluid porous media models in Pronghorn and SAM, comparisons between coupled Pronghorn-Griffin and coupled SAM-Griffin models for two loss-of-forced cooling events and one control rod withdrawal event, and comparisons between SAM single-solve and domain-overlapping approaches for multi-scale thermal fluid coupling. In addition, we performed comparisons between 3-D, 2-D, and 0-D neutronic models for the two control rod withdrawal scenarios with Pronghorn-Griffin. The results show that the BlueCRAB models led to physically intuitive solutions for the scenarios examined. The changes in the various scalar and vector fields such as the neutron flux, power, temperatures, densities, pressures, and velocities are all within the expected ranges, and their distributions can be explained from the system response of the transients and the geometric and material variations. Several comparisons suggest that the porous media models in Pronghorn and SAM can lead to similar solutions, even though they are based on different methodologies. The simulations demonstrate that there are differences between the various levels of fidelity, and it is advisable to have flexible tools that can cover the breadth and depth of needs that may arise in future technical evaluations. We believe that BlueCRAB's capabilities represent a significant asset for confirmatory analyses aimed at resolving important safety questions.

Page intentionally left blank

CONTENTS

FIGURES

TABLES

ACRONYMS

AGR	Advanced Gas Reactor Program
AGR	Advanced Gas Reactor
API	Application Programming Interface
CFD	Computational Fluid Dynamics
CR	Control Rod
DB	Dittus-Boelter
EFPD	Effective Full Power Days
FIMA	Fissions per Initial Heavy Metal Atom
IQS	Improved Quasi-Static
LOFC	Loss of Forced Circulation
NEAMS	Nuclear Energy Advanced Modeling and Simulation
PB-FHR	Pebble Bed Fluoride-Cooled High-Temperature Reactor
PBR	Pebble Bed Reactor
PHSS	Pebble Handling and Storage System
PKE	Point Kinetics Equations
RCCS	Reactor Cavity Cooling System
RPS	Reactor Protection System
STH	System Thermal-Hydraulics

Page intentionally left blank

ACKNOWLEDGMENTS

The authors would like to acknowledge the support and assistance from Stephen Bajorek, Tarek Zaki, Andrew Bielen, Nazila Tehrani, Jason Thompson, and Pravin Sawant of the United States Nuclear Regulatory Commission in the completion of this work. This work would not have been possible without the contributions from the Idaho National Laboratory Griffin development team: Yaqi Wang, Josh Hanophy, Olin Calvin, and Namjae Choi. This work would not have been possible without the contributions from members of the Idaho National Laboratory Pronghorn development team: Mauricio Tano and Victor-Coppo Leite. This work was performed in conjunction with Idaho National Laboratory, Argonne National Laboratory and the U.S. Nuclear Regulatory Commission under Task Order Agreement No. 31310019F0015 and 31310021F0005. This research made use of the resources of the High Performance Computing Center at Idaho National Laboratory, which is supported by the Office of Nuclear Energy of the U.S. Department of Energy and the Nuclear Science User Facilities under Contract No. DE-AC07-05ID14517.

Page intentionally left blank

Fluoride-Cooled High-Temperature Pebble-Bed Reactor Reference Plant Model Updates

1. INTRODUCTION

The Pebble Bed Fluoride-Cooled High-Temperature Reactor (PB-FHR) is a novel nuclear reactor design that has garnered significant attention in recent years, due to its potential as a safe, efficient, and sustainable energy source. This reactor concept combines the advantages of a pebble-bed reactor, which features a graphite matrix containing fuel pebbles, with a fluoride salt coolant, which offers excellent heat transfer properties and a high operating temperature.

One key benefit of the PB-FHR design is its ability to operate at extremely high temperatures (i.e., up to 700°C), which makes it an ideal candidate for applications such as hydrogen production, chemical processing, and power generation. Additionally, the PB-FHR design is inherently safe, as the pebble-bed reactor is less susceptible to reactivity accidents and the fluoride salt is an excellent heat transfer coolant. These characteristics make the PB-FHR an attractive option for future nuclear energy applications.

Development of the PB-FHR is being actively pursued by researchers and engineers around the world, with several organizations and governments investing significant resources into its design and testing. The licensing of a PB-FHR is a critical step in its development and deployment. As a new reactor design, the PB-FHR must undergo sufficiently rigorous review and evaluation by regulatory agencies to ensure that it meets all applicable safety requirements. This process often involves a comprehensive analysis of the reactor's design (e.g., safety features, materials, and operating conditions) in order to determine whether it can be safely operated and maintained.

The Comprehensive Reactor Analysis Bundle (CRAB or alternatively BlueCRAB) is the code suite proposed for non-light-water reactor (non-LWR) systems safety analyses by the U.S. Nuclear Regulatory Commission. The main objective of this work is to assess the level of readiness of BlueCRAB for modeling fluoride-cooled high-temperature pebble-bed reactors. This is achieved via the following tasks:

- Developing numerical models in BlueCRAB that include the majority of the physics relevant to this technology, ensuring an adequate level of fidelity for modeling reactor safety performance during accident scenarios.
- Performing comparisons between the thermal fluid porous media models in Pronghorn and SAM, with a 2-D geometry for steady state and the protected loss-of-forced-circulation transient scenario.
- Performing comparisons between coupled Griffin reactor physics and thermal fluid porous media models in Pronghorn and SAM, with a 2-D geometry for steady state, the control rod withdrawal, and the unprotected loss-of-forced-circulation transient scenario.
- Performing comparisons between single-solve and domain-overlapping multi-scale thermal fluid coupling approaches for coupling the SAM 2-D porous media core model and SAM 1-D loop model for steady state ass well as a protected loss-of-forced-circulation transient.
- Performing comparisons between the Griffin spatial dynamics and SAM-PKE for the unprotected loss-of-forced circulation transient with the SAM 2-D core and the SAM system model.
- Performing sensitivity analysis with the SAM core fluids solver coupled to the SAM-PKE and the SAM loop model for the unprotected loss-of-forced-circulation transient.
- Testing the 3-D capabilities of the thermal fluid porous media models in Pronghorn.
- Testing the 3-D capabilities for a coupled model with Griffin and Pronghorn.
- Performing comparisons between 3-D, 2-D, and 0-D/PKE models for two control rod withdrawal scenarios (one delayed and one prompt supercritical reactivity insertion).

Section 1.1 introduces the PB-FHR characteristics and the technical specifications for the reference plant model. Section 1.2 describes the accident scenarios that were analyzed.

1.1. System Description

The Pebble Bed Fluoride-Cooled High-Temperature Reactor (PB-FHR) design was based on published (open domain) material from the gFHR benchmark [1] developed by Kairos Power, along with some information from the non-proprietary documentation of the Hermes demonstration reactor [2]. Therefore, the PB-FHR specifications do not contain any specific design information from any Kairos design, and thus do not entirely provide a full characterization of any proprietary Kairos Power design. The schematic representation of the PB-FHR is presented in Figure 1, including the pebble-bed core, reflector, core barrel, salt downcomer, and reactor vessel. The main characteristics of the core design are included in Table 1. The thermal power of this PB-FHR model is 320 MW. The inlet and outlet temperatures are assumed to be 550°C and 650°C, respectively, with a corresponding flow rate of 1324.6 kg/s. This design relies on a multipass strategy in which the pebbles are discharged from the top of the active core and then reintroduced uniformly at the bottom of the core. The pebbles are buoyant and float toward the top of the core. They undergo an average of eight passes before being discharged. The recirculation, evaluation, and disposal tasks are performed by the Pebble Handling and Storage System (PHSS). During the evaluation task, the PHSS determines whether the pebble has achieved the desired design burnup limit, at which point it is either discharged or recirculated back to the bottom of the core. Note that the average residence time in the original journal article [1] was approximated at 490–550 Effective Full Power Days (EFPD).

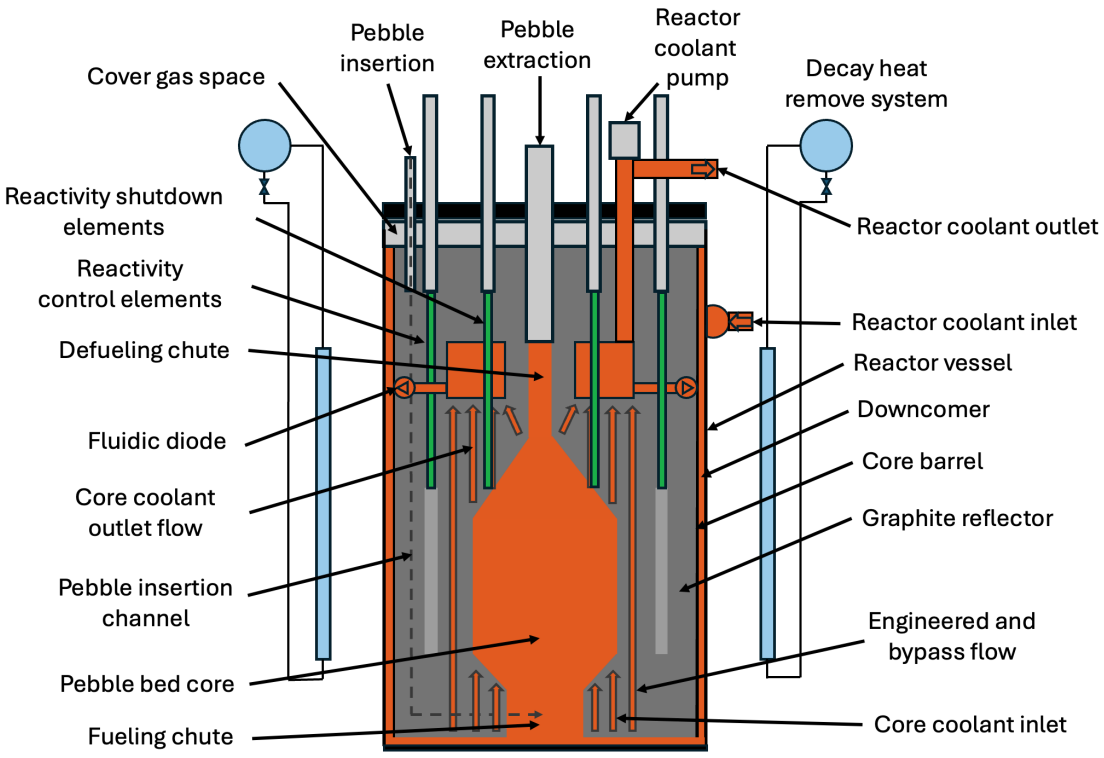

Figure 1. Schematic of the reference PB-FHR design, reproduced from [3].

This benchmark uses a single pebble design or type. The pebble specifications are shown in Table 2. The pebble includes a spherical lower density center graphite core, which makes the pebble buoyant, followed by a spherical shell that contains the TRISO particles and then an outer spherical graphite shell.

The TRISO design specifications, which are included in Table 3, are based on the oxycarbide fuel testing from the Advanced Gas Reactor Program (AGR) AGR-2 irradiation campaign [4], with the carbon content set to the upper limit of the AGR testing envelope.

Table 1. PB-FHR reactor specifications.

Parameter	Value
Core power [MWth]	320
Core inlet temperature [K]	823.15
Core outlet pressure [Pa]	1e5
Mass flow rate [kg/s]	1324.6
Pebble bed radius [m]	1.2
Cylindrical pebble bed height [m]	3.1
Pebble bed height with cones [m]	5.1
Number of pebbles (fully packed)	256,209
Pebble types	One pebble type (3.4g IHM)
Pebble packing fraction (average)	0.6
Average number of passes	8
Average pebble residence time [days]	522
Reflector outer radius [m]	1.8
Barrel outer radius [m]	1.82
Downcomer outer radius [m]	1.87
Vessel outer radius [m]	1.91

Table 2. Pebble specifications [1].

Parameter	Value
Pebble core radius [cm]	1.380
Fuel layer radius [cm]	1.8
Shell layer radius [cm]	2.0
Number of particles per pebble	11,660
Pebble core graphite density [kg/m^3]	1,410
Fuel layer matrix density [kg/m^3]	1,740
Shell layer graphite density [kg/m^3]	1,740

The reactor core is geometrically represented in Figure 2, with the pebble-bed zones (chutes, cones, and cylindrical core) shown as being fully packed with pebbles. The figure also depicts the position of the control rod channels and the downcomer. The various core structures and components are described in Figure 2. The pebbles and FLiBe coolant flow in the positive axial direction (z-axis). The pebbles enter the core through the fueling chute (1), flow to the lower cone (3) and then through the cylindrical core region (4 and 5), enter the upper cone (6), and finally exit via the defueling chute (7). Region 5 is the high-porosity region that physically occurs between the pebble bed and the wall. The fluid enters the core via the cold leg and moves through the downcomer (15), is mixed at the bottom plenum (refer to Figure 1), flows through the inlet annulus (2) and the fueling chute (1), and then continues on to the lower cone (3), although some flow is redirected into the control rod channels (10 and 11). It heads through the cylindrical core region (4 and 5), enters the upper cone (6), and finally exits via the outlet annulus (8) into the hotwell (17), and some flow is diverted into the defueling chute (7). In some publicly available information [5], there is a flow connection (16) between the defueling chute (7) and the hotwell (17), but the details on this are not yet known.

Table 3. TRISO specifications [1].

Parameter	Value
Fuel kernel radius [cm]	0.0212
Buffer outer radius [cm]	0.03125
IPyC outer radius [cm]	0.03525
SiC outer radius [cm]	0.03875
OPyC outer radius [cm]	0.04275
Fuel type	$UC_{0.5}O_{1.5}$
Fuel enrichment	19.55%
Fuel kernel density [kg/m^3]	10,500.0
Buffer graphite density [kg/m^3]	1,050.0
IPyC, OPyC graphite density [kg/m^3]	1,900.0
SiC density [kg/m^3]	3,180.0
Matrix graphite density [kg/m^3]	1,740.0

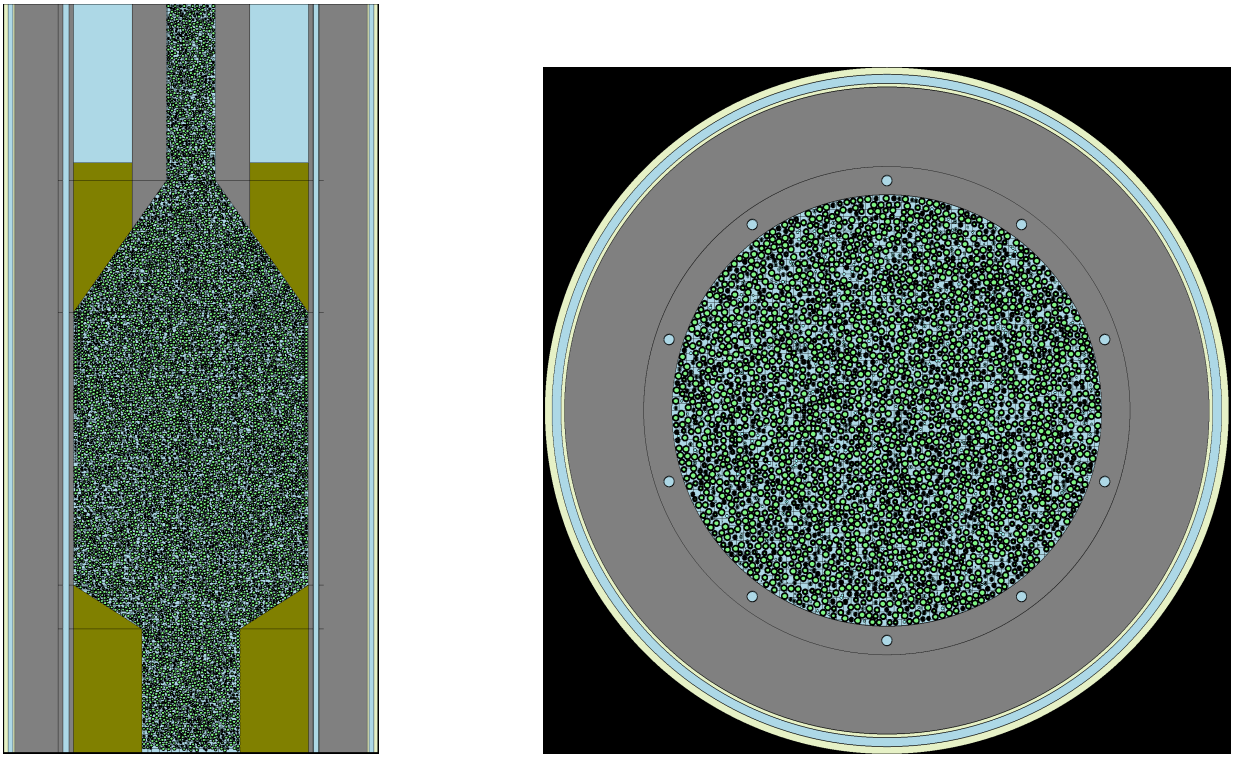

Figure 2. Geometric representation of the PB-FHR core. Pebble positions were obtained from a Project Chrono discrete element code [6] simulation and the figures from the Serpent Monte Carlo code [7].

The primary loop for the reference PB-FHR is shown in Figure 4. The cold salt flows downward into the downcomer and, after being collected in the inlet plenum at the bottom of the reactor core, is forced upward through a packed pebble-bed reactor core. At the top of the core, most of the hot salt flows directly through the outlet annulus region and into the outlet plenum, where it is collected and pumped into the hot leg of the primary loop. A small portion of the hot salt from the core outlet flows into the defueling chute to provide cooling to fuel pebbles slowly traveling upward. After leaving the defueling chute, the hot salt merges into the

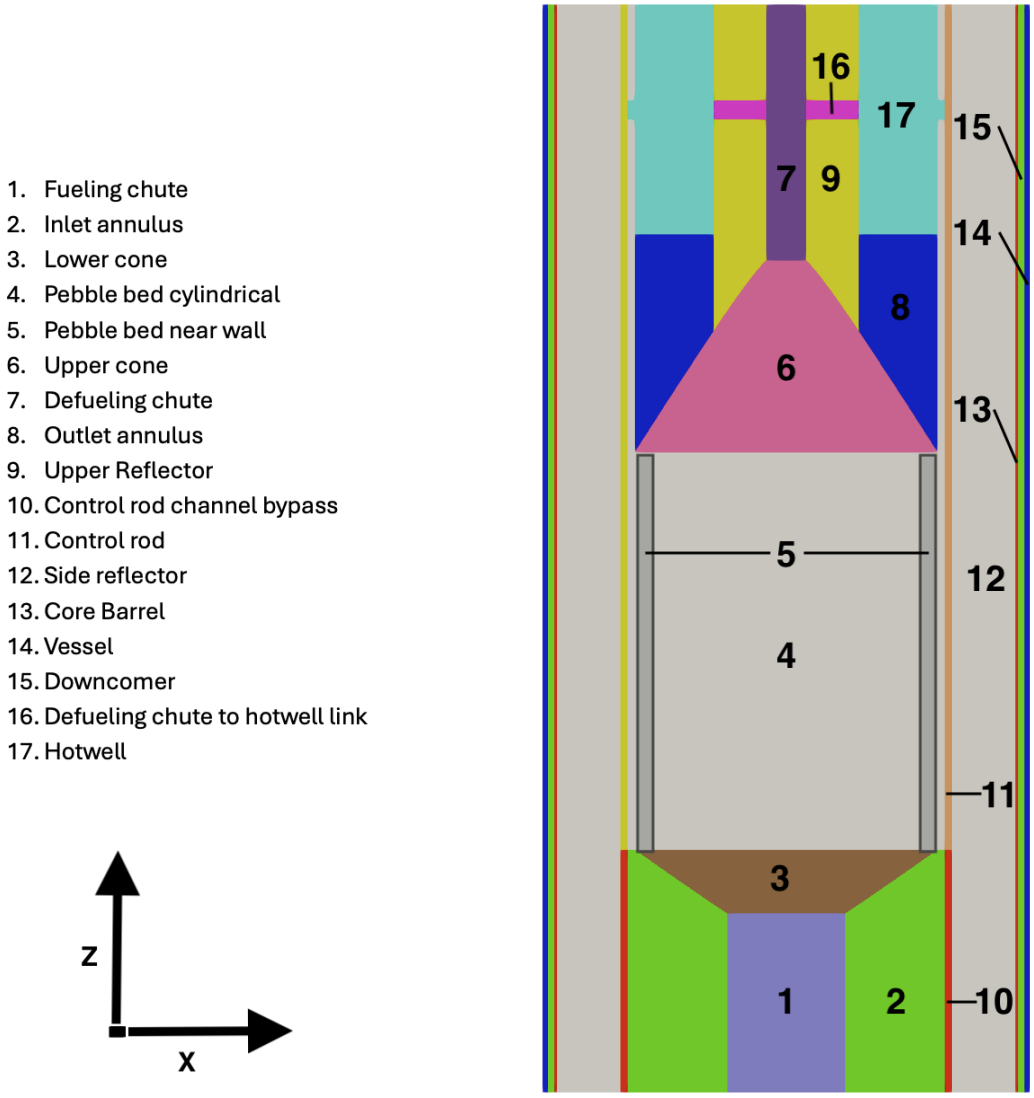

Figure 3. Geometric regions for the PB-FHR model.

outlet plenum. It then exits the outlet plenum and enters the primary coolant pump. After exiting the pump, it passes through a heat exchanger, where heat is transferred to the secondary-side salt. The cooled salt then passes through a network of piping until it reaches the reactor vessel and is distributed within the downcomer. A fluidic diode, which is a device used in Kairos Power's FHR design so as to allow single-direction flow, connects the outlet plenum and downcomer in the PB-FHR loop. During normal operating conditions when the primary pump is running, the fluidic diode minimizes the amount of bypass flow from the downcomer to the outlet plenum. When the primary pump is not operating, the fluidic diode allows for the flow of coolant from the outlet plenum to the downcomer, meaning that a flow path for natural circulation between the hot core region and cold downcomer region could be established.

In the secondary loop, secondary-side salt flows through the intermediate heat exchanger, where it absorbs heat from the primary loop salt. The heated secondary-side salt then enters the secondary heat exchanger. After being cooled in the secondary heat exchanger, it is circulated by the secondary pump back to the intermediate heat exchanger. In addition to the primary and secondary loops, a simplified Reactor Cavity Cooling System (RCCS) loop design is shown in Figure 5. This RCCS loop design is not based on any

prototype design. Through radiative heat transfer, heat is removed from the outer surface of the reactor vessel wall to the RCCS cooling panels. The water in the RCCS loop transfers the heat from the vessel wall to the air dump heat exchanger, which is connected to an outlet stack in order to increase the natural circulation driving head. With the RCCS system and the fluidic diode, passive heat removal from the primary system is achieved when the primary pump is not operating. This RCCS is designed to remove the system's long-term decay heat. During normal operation conditions, the RCCS will remove approximately 0.3% of reactor power.

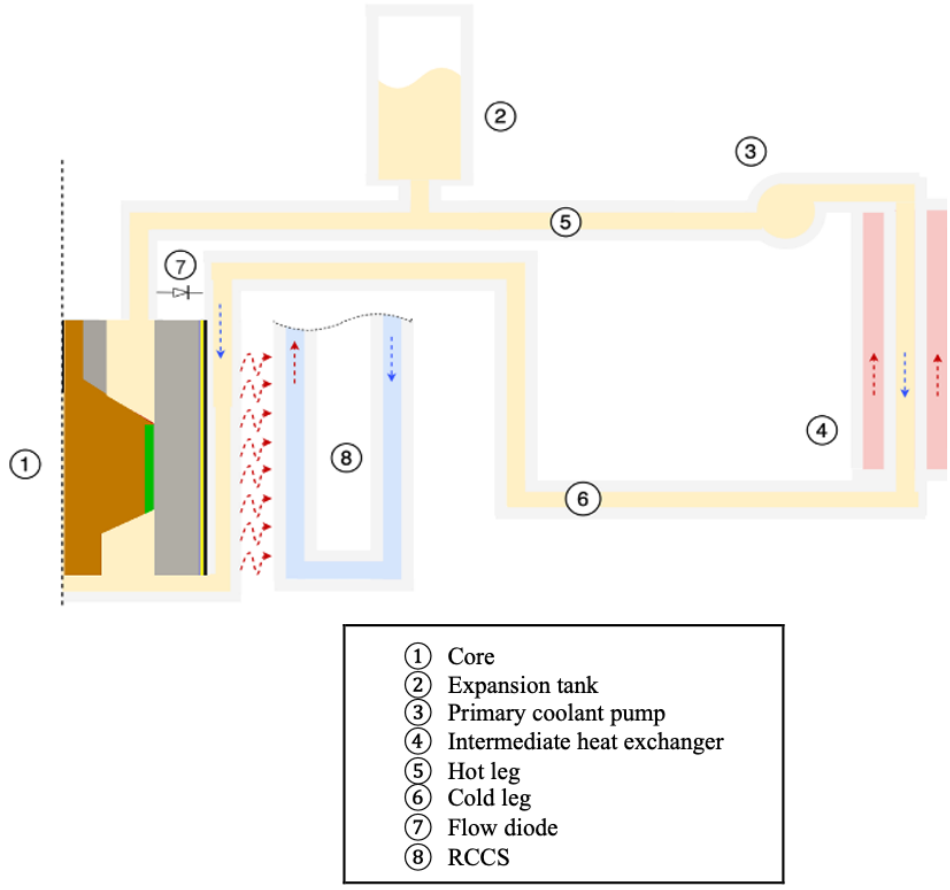

Figure 4. Graphical representation of the reference PB-FHR.

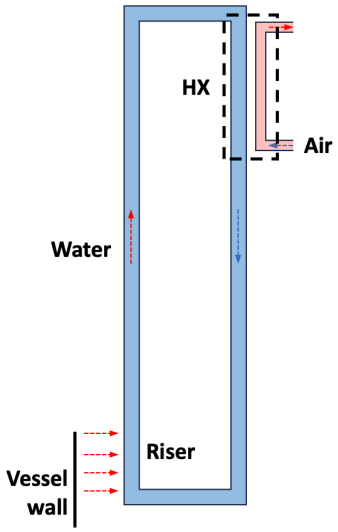

Figure 5. Graphical representation of the RCCS.

1.2. Scenario Selection And Description

1.2.1. Loss-of-Forced-Circulation Scenario

The standard assumption for this scenario involves the concurrent failure of the primary and secondary pumps, resulting in the Loss of Forced Circulation (LOFC) [8]. The change in the mass flow rate is detected by the Reactor Protection System (RPS), at which point the RPS initiates the insertion of all control and shutdown elements, thus fulfilling the reactivity control function. In addition, the reactor decay heat removal system is operational and limits the reactor temperature, thus fulfilling the heat removal function.

The safe core state is established when the following two criteria are met:

1. The core is maintained in a subcritical state and long-term reactivity control is assured.
2. The decay heat is being successfully removed and long-term cooling is assured. The figure-of-merit temperatures are steadily decreasing, and the FLiBe temperature remains above the FLiBe freezing temperature throughout the mission time of the decay heat removal system.

For the LOFC category, there are two bounding events for evaluating long-term passive cooling performance: (1) the overheating and (2) the downcomer freezing consequences. The following key figures of merit are typically evaluated:

- Peak TRISO temperature, in relation to the diffusion of radionuclides and to limit incremental TRISO layer failures
- Peak vessel and core barrel temperatures, in relation to long-term cooling
- Peak temperature of structural graphite, in relation to tritium release
- Peak temperature of pebble carbon matrix, in relation to tritium release
- Minimum reactor vessel inner-surface temperature to prevent partial freezing within the downcomer (long-term overcooling scenario).

For the present work, two modalities of the LOFC were studied that depend on the actions from the RPS. The first scenario assumes that the reactivity control function is met by the RPS. This is the controlled LOFC, the event sequence for which is shown in Table 4. In practice, it takes a finite amount of time for the RPS to detect the change in mass flow rate and to initiate insertion of all control and shutdown elements to shut down the reactor. However, due to lack of detailed information, the present work assumes immediate shutdown at the onset of the transient (i.e., at 0 seconds). The second scenario assumes that the reactivity control function is not met by the RPS. This is the uncontrolled LOFC, the event sequence for which is shown in Table 5. The evolution of the pump head fraction during the LOFC scenario is illustrated in Figure 6. It is assumed that pump head decreases following an exponential coast-down curve with a halving time of 4.5 s. Complete loss of pump head is reached at 76.5 s.

Table 4. Protected LOFC event.

Time [s]	Event
$-\infty$ – 0.0	No change in system parameters; steady state conditions are well established.
0.0	Instantaneous insertion of all control and shutdown elements.
0.0 – 76.5	Reduction of the primary and secondary pump head fraction from 1.0 to 0.0, using an exponential curve with a halving time of 4.5 seconds, as shown in Figure 6.
76.5 – 1E8	No change to system parameters.

Table 5. Unprotected LOFC event.

Time [s]	Event
$-\infty$ – 0.0	No change in system parameters; steady state conditions are well established.
0.0 – 76.5	Reduction of the primary and secondary pump head fraction from 1.0 to 0.0, using an exponential curve with a halving time of 4.5 seconds, as shown in Figure 6.
76.5 – 1E8	No change to system parameters.

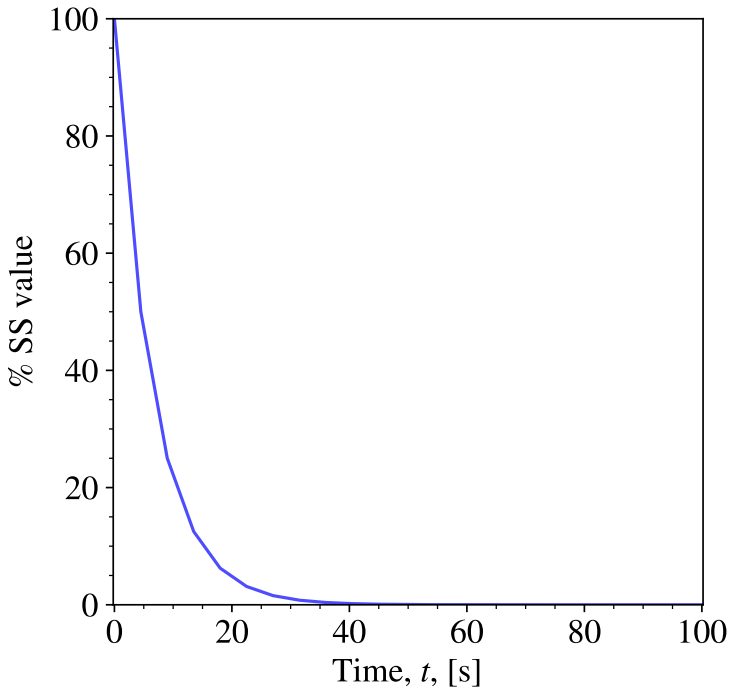

Figure 6. Pump head fraction during LOFC scenarios.

1.2.2. Control Rod Withdrawal Scenarios

The standard assumption for the control rod withdrawal scenario in pebble-bed reactors is either a control system error or operator error that causes continuous withdrawal of the highest-worth control element at the maximum reactivity control and shutdown system (RCSS) drive speed. In this scenario, credit is allowed for the RPS, which upon detection of the changes in the power level initiates insertion of all control and shutdown elements, thus fulfilling the reactivity control function [8]. This is typically combined with a transient analysis that includes the decay heat removal system, which limits the reactor temperature and fulfills the heat removal function.

The following key figures of merit are typically evaluated:

- Peak TRISO temperature, in relation to the diffusion of radionuclides and TRISO layer failures
- Peak vessel and core barrel temperatures, in relation to long-term cooling
- Peak temperature of structural graphite, in relation to tritium release
- Peak temperature of pebble carbon matrix, in relation to tritium release.

In this work, we depart from this standard scenario, since the primary purpose is to test physics included in the 3-D and 2-D numerical models. First, we simulate two fictional control rod withdrawal events: a fast delayed-supercritical and a slow prompt-supercritical event. The two transients involve the inadvertent movement of one and two control rods, respectively. The sequences of events are shown in Tables 6 and 7. In addition, we do not take credit for the reactor protection system actuation. Instead, the control rods are reinserted to their initial positions. These events test the physics for fast and slow reactivity insertions and the feedback physics.

Table 6. Delayed-supercritical control rod withdrawal event.

Time [s]	Event
0.0 – 10.0	No change in system parameters, and the system is running for 10.0 s to confirm that steady-state conditions are well established, with all rods banked at 2.21 m.
10.0 – 10.85	Withdraw control rod 5 (CR5) from position 2.21 m to position 6.5 m in 0.85 s.
10.85 – 22.0	The control rod stays at position 6.5 m.
22.0 – 24.0	The control rod is reinserted to its initial position in 2 s.
24.0 – 300.0	No change to the system's main parameters; the simulation is performed for up to 300 s.

Table 7. Prompt-supercritical control rod withdrawal event.

Time [s]	Event
0.0 – 10.0	No change in system parameters, and the system is running for 10.0 s to confirm that steady-state conditions are well established, with all rods banked at 2.21 m.
10.0 – 30.0	Withdraw control rods 5-6 from position 2.21 m to position 6.5 m in 20 s.
30.0 – 40.0	The control rods remain at position 6.5 m.
40.0 – 44.0	The control rods are reinserted to their initial positions in 4 s.
44.0 – 300.0	No change to the system's main parameters; the simulation was performed for up to 300 s.

2. METHODOLOGY

Multiphysics coupled simulations for the PB-FHR were performed using the Comprehensive Reactor Analysis Bundle (CRAB or alternatively BlueCRAB), which is the code suite proposed for non-light-water reactor (non-LWR) system safety analyses. BlueCRAB includes the Griffin [9] code for reactor physics, the Pronghorn [10] code for core thermal fluids, the BISON [11] code for solid conduction and fuel performance, and the SAM [12] code for system analysis. For this work, Griffin, Pronghorn, and SAM were utilized in the simulations. Griffin is a time-dependent, finite-element-based reactor physics code with weak-form formulations for diffusion, spherical harmonics (PN), and first-order discrete ordinates (SN) transport and a variety of equivalence techniques. Pronghorn is a multidimensional thermal-hydraulics code for advanced nuclear reactors, and is capable of intermediate-fidelity Computational Fluid Dynamics (CFD) for advanced nuclear reactors. SAM is a system analysis tool for advanced non-LWR safety analysis, and is capable of system-level modeling with built-in components, as well as higher-fidelity flow modeling with its multi-D flow models.

In this work, neutronics calculations were performed with Griffin, while thermal-hydraulics calculations of the core were performed using porous media models developed separately with Pronghorn and SAM. Outside of the core, the primary, secondary, and RCCS loops were modeled using SAM's component system, or instead just given boundary conditions for the porous media model of the core. As a result, two sets of coupled models were developed: the SAM/Griffin/SAM model and the Pronghorn/Griffin/BC model. Hereafter in this report, the coupled models are labeled per the following convention: the first name is the code for modeling the porous media core, the second name is the code for modeling the neutronics, and the third name is the code for modeling the loops. In the SAM/Griffin/SAM model, SAM's porous media model was used for thermal-hydraulics calculations in the core, Griffin for the neutronics calculation, and SAM for thermal-hydraulics calculations in the loops. In the Pronghorn/Griffin/BC model, Pronghorn's porous media model was used for thermal-hydraulics calculations in the core, Griffin was used for the neutronics calculation, and boundary conditions were provided for the 2-D porous media model instead of coupling to SAM loop models.

The porous media approach was employed to model the reactor core. Two 2-D R-Z axisymmetric models of the core were developed using Pronghorn and SAM. The primary difference between the two models is that SAM is a finite-element-based code whereas Pronghorn is a finite-volume-based code. The 2-D models were necessary to capture the relatively complex fluid flow and heat transfer phenomena in the core, especially during certain transient scenarios. The remainder of this section provides details on the models, including the meshing, coupling, assumptions, and simplifications employed. We also developed a 3-D flow model in Pronghorn to examine more complex flow characteristics and couple it to 3-D Griffin.

The applicability of the point reactor approximation is always an important question in reactor physics, due to the underlying assumption of separability of the neutron population density from the flux shape. Some scenarios that involve large changes to the flux distribution (i.e., control rod movement) can invalidate this assumption, and it is common practice to apply penalties to the PKE parameters (reactivity, mean generation time, or delayed neutron fraction) to overcome this limitation. Another approach is to rely on a spatial dynamics solution to better understand the accuracy of the PKE solution under specific scenarios. Ideally, one would rely on a high-fidelity coupled transport calculation that can serve as a reference solution to provide confidence in the results. For the present work, we deployed Griffin's multigroup diffusion solver in 3-D to provide such a reference solution. We also developed a 2-D model-equivalent of this reference 3-D model. In the future, the Griffin's SN transport is recommended as a reference solution due to recent improvements in this technology [13]. A brief introduction to the PKE theory and a description of the Griffin PKE model are included in Section 2.2.5.

2.1. Reactor Core Mesh Generation

The finite-element mesh used in the 2-D and 3-D models was developed with CUBIT [14] via the Python Application Programming Interface (API). The geometric specifications used in the meshing scripts are provided in Table 8 for the radial dimensions, Table 9 for axial, and Table 10 for the cone dimensions.

Table 8. PB-FHR mesh radial dimensions.

Region, radius [m]	Value
Defueling chute	0.25
Fueling chute	0.5
Cylindrical pebble bed	1.2
Reflector zone before control rod	1.25 *
Control rod zone	1.308 *
Reflector outer	1.8
Barrel outer	1.82
Downcomer outer	1.87
Vessel outer	1.91

* In the baseline model, there is no explicit reflector zone before the control rod and the radial position of the control rod, which extends to radial position 1.358 m.

Table 9. PB-FHR mesh axial dimensions.

Location, elevation [m]	Value
Top of fueling chute	1.4
Top of lower cone	1.9
Top of cylindrical pebble bed	5
Top of upper cone	6.5
Top of defueling chute	8.5

Table 10. PB-FHR mesh cone dimensions.

Parameter, dimension [m]	Value
Lower cone large radius	1.2
Lower cone small radius	0.5
Lower cone height	0.5
Upper cone large radius	1.2
Upper cone small radius	0.25
Upper cone height	1.5

To minimize the number of elements and thus the computational cost, the mesh was generated with quadrilateral elements that can be easily extruded in 3-D. For the 3-D cylindrical geometry, there is always a compromise on how to mesh the center of the geometry, and we chose to keep quadrilateral elements for the pebble-bed region in a single block, since using triangular prism elements would require a separate block, per the Exodus [15] format. In the latest modification to the Python scripts, we added the capability to assign pebble streamline zones and streamline discretization layers to variables in the mesh file. This allowed us to generate consistent models for the 2-D and 3-D simulations. There are several variants of these mesh files, as testing of the codes required the inclusion or exclusion of certain zones (i.e., hotwell, the link between the defueling chute and hotwell, the downcomer, and the fluidic diode). The following sections explain these variants.

2.2. Core Neutronics Modeling Approach And Assumptions

Griffin [9], a foundational capability in BlueCRAB, is the universal tool deployed in this work. Griffin is a reactor physics application built on the MOOSE framework. It provides neutron transport, depletion, core performance, decay heat, and cross-section calculation capabilities for non-light-water advanced reactor technologies. In this report, we refer to reactor kinetics as the time-dependent behavior (short-time scale) of the neutron population in a nuclear reactor with delayed neutrons in the absence of feedback, and to reactor dynamics as the general time-dependent behavior of the neutron population in a nuclear reactor with delayed neutrons and with feedback. This section describes the neutron cross-section and core neutronics models developed in this work.

For this work, we deployed Griffin's diffusion approximation to solve the linearized Boltzmann transport equation with the multigroup approximation in the energy domain. Multigroup cross sections must be provided as a function of reactor state parameters such as temperature and burnup in order to perform neutronics and depletion calculations with Griffin. Section 2.2.1 provides an overview of the development of neutron cross sections. Section 2.2.2 describes the baseline model developed for comparison of the coupled Pronghorn/Griffin and SAM/Griffin models. Section 2.2.3 then presents the model developed to simulate the reactivity insertion accident, using Griffin in 3-D, 2-D, or 0-D (PKE). In Section 2.2.4, we discuss modifications made to the mesh so as to enable the coupling to Pronghorn for the LOFC scenario. In Section 2.2.5, we cover the development of the 0-D/PKE Griffin model. Finally, the main neutronic modeling assumptions and approximations are listed in Section 2.2.6.

2.2.1. Neutron Cross Sections

The cross-section preparation methodology relied on the DRAGON5 [16] code, since the cross-section capability for Griffin was just merged in fiscal year (FY) 2025 [17]. A detailed description of the DRAGON cross-section preparation is detailed in the gFHR report [18]. The main departure from that original work is the replacement of various macroscopic cross sections with microscopic cross sections in the reflectors, control rods, and coolant regions in order to allow more flexibility in the porosity assignment and to include local changes to the coolant density in regions outside the pebble bed. The broad-group energy structure used in this work is shown in Table 11. This group structure will be optimized in future work during deployment of the native Griffin cross-section methodologies [17].

The main contributors to the reactor feedback mechanism in the PB-FHR are attributed to changes in:

- Fuel temperature — the fuel kernel temperature
- Moderator temperature — the temperature of all of the materials in the pebble, with the exception of the fuel kernel
- Coolant density — FLiBe density
- Reflector temperature — graphite reflector temperature.

Table 11. Neutron energy group boundaries for the four-group structure.

Neutron energy [eV]
1.96403000E+07
1.95007703E+05
1.75647602E+01
2.33006096E+00
1.10002700E-04

The tabulated values for the active core-region cross sections are shown in Table 12, and for mixed graphite-FLiBe the control rod and downcomer regions are shown in Table 13. Note that the control rod material does not yet support coolant density changes. The core barrel and vessel are the only macroscopic regions found in the model in Table 14. Table 15 contains the core regions along with their respective porosity values used in the various Griffin models.

Table 12. PB-FHR model microscopic cross-section tabulation parameters for the active core region.

Parameter	Value
Number of isotopes	297
Burnup tabulation [J/cm^3]	0.00, 8.526E+08, 1.759E+9
Fuel temperature tabulation [K]	600.0, 859.0, 959.0, 1059.0, 1200.0, 1600.0
Moderator temperature tabulation [K]	600.0, 800.0, 900.0, 1000.0, 1200.0
Coolant density tabulation [kg/m^3]	1925.0, 1973.8, 2022.6, 2120.2

Table 13. PB-FHR model microscopic cross-section tabulation parameters for various regions.

Parameter (Mixed Graphite-FLiBe Regions)	Value
Graphite Temperature [K]	600.0, 900.0, 1200.0
Coolant Density [kg/m^3]	1925.0, 1973.8, 2022.6, 2120.2
Parameter (Mixed Graphite-FLiBe-B_4C Regions)	Value
Graphite / B_4C Temperature [K]	600.0, 900.0, 1200.0
Parameter (FLiBe Regions)	Value
Coolant Density [kg/m^3]	1925.0, 1973.8, 2022.6, 2120.2

Table 14. PB-FHR model macroscopic cross-section tabulation parameters for steel regions.

Parameter	Value
SS 316H temperature tabulation [K]	600.0, 900.0, 1200.0

Table 15. Porosity and materials for the Griffin core models.

Region No.	Region name	Material	Porosity
1	Fueling chute	Pebbles/FLiBe	0.388 [1]
2	Inlet annulus	Graphite/FLiBe	0.388
3	Lower cone	Pebbles/FLiBe	0.388 [1]
4 & 5	Pebble bed	Pebbles/FLiBe	$0.388 \cdot fp(r)$ [1,2]
6	Upper cone	Pebbles/FLiBe	0.388 [1]
7	Defueling chute	Pebbles/FLiBe	0.388 [1]
8	Outlet annulus	Graphite/FLiBe	0.388
9	Upper reflector	Graphite	0.000
10	Control rod channel	Graphite/B_4C/FLiBe	0.045/0.0151 [3]
11	Control rod channel bypass	Graphite/FLiBe	0.182/0.061 [4]
12	Side reflector	Graphite	0.000
13	Core barrel	Stainless steel 316H	0.000
14	Vessel	Stainless steel 316H	0.000
15	Downcomer	FLiBe	1.000
16	Defueling chute to hotwell link	Graphite/FLiBe	0.388
17	Hotwell	FLiBe	1.000

[1] The value 0.388 was used in the baseline model for making comparisons between Pronghorn/Griffin and SAM/Griffin. The value 0.378 was used in the rest of the Griffin models to be consistent with Kairos Power publications [1].

[2] A radial porosity function [2] $fp(r) = 1 + 1 \cdot e^{\frac{r - r_{core}}{r_{pebble}}}$.

[3] The control rod channel with a control rod inserted has a porosity of 0.045 in the 3-D model and 0.0151 in the 2-D model.

[4] The control rod channel when no control rod is inserted has a porosity of 0.182 in the 3-D model and 0.061 in the 2-D model.

Table 16. PB-FHR model streamline depletion specifications.

Parameter	Value
Number of streamlines	5 (equally spaced)
Number of pebble types	1
Number of burnup groups	8 (from 0 to 155)
Discharge burnup (MWd/kgU, J/cm^3)	155, 1.36×10^9
Base discretization $\Delta\tau_b$ (J/cm^3)	1.87×10^8
Pebble speed (cm/day)	4.74
Pebble unloading rate (pebbles/day)	3,983

2.2.2. Baseline Model for Spatial Dynamics

The purpose of the baseline model is to provide a means for comparing the results from the Pronghorn/Griffin and SAM/Griffin coupled models with simplified geometry. The Griffin computational mesh with five discrete 1-D streamlines is shown in Figure 7. The control rod is homogenized over a larger reflector region, and the neutronics model does not include the inlet plenum, explicit diode, or the link between the refueling chute and hotwell.

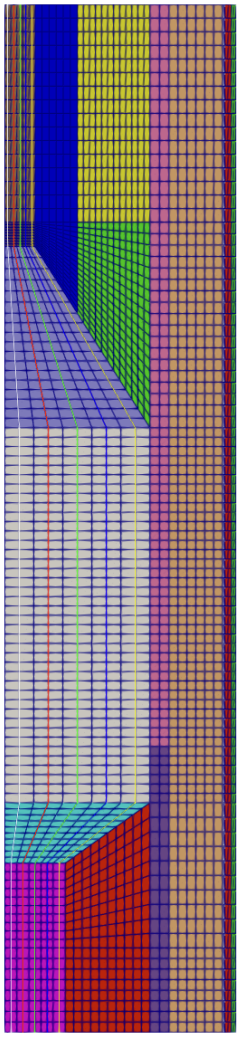

Figure 7. Baseline 2-D Griffin mesh with streamlines.

2.2.3. Control Rod Withdrawal Model

The purpose of the control rod withdrawal model is to provide a means for comparing the results from the Pronghorn/Griffin coupled model in the 3-D, 2-D, and 0-D domains. The computational mesh for the 3-D and 2-D models is shown in Figure 8. In this model, we removed the downcomer, vessel, and SAM loop model to simplify the complexity for this transient. We included the link between the defueling chute and the hotwell so as to investigate potential problems in modeling the flow in those regions. There is also a graphite region between the core periphery and the homogenized control rod region. Additional mesh details for the

3-D model are provided in Figure 9, which shows the 10 homogenized control rod regions and the radial and azimuthal discretizations. The pebble streamline assignment and discretization layers for the 2-D and 3-D models are illustrated in Figure 10 and use 5 and 41 streamlines, respectively, and 15 axial layers in both modls to define the trajectory of the pebbles in the pebble bed.

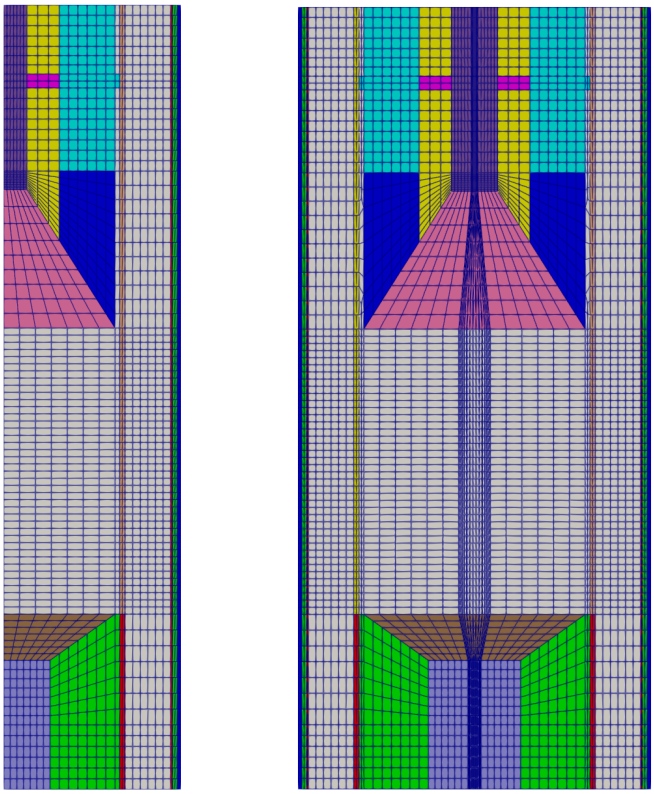

Figure 8. Computational mesh for 2-D and 3-D simulations.

We developed a methodology to generate a 2-D model that is nearly equivalent to the 3-D model. One significant difference between the 2-D and 3-D general modeling approaches for PBRs lies in the control rod regions. Our 3-D model includes explicit, albeit homogenized, rod regions, whereas the 2-D model relies on a gray curtain approach (i.e., azimuthally constant). This can lead to overestimation of the absorption of neutrons as they enter the reflector zone in the 2-D model. A simple solution is to dilute the control rod material definition in the 2-D model until the eigenvalues from the 2-D and 3-D models are equal. This will not necessarily preserve the neutron currents returning to the pebble bed in the 2-D model, but allows us to approximate the solution from the 3-D simulation. Use of a gray curtain in the 2-D model changes the worth of the control rods and the subsequent insertion of reactivity. We can use dilution by taking advantage of the control rod material definition in Griffin, enabling the user to define a minimum of three control rod segments: lower follower, poison region, and upper follower. The lower and upper followers extend to $-\infty$ and $+\infty$, respectively (refer to Figure 11). The control rod channel extends the full axial domain with the two regions 10 and 11. Region 10 uses a material definition that includes a homogenized mixture of graphite and FLiBe, whereas in Region 11 we use the control rod material to define the three segments for different homogenized mixtures of graphite, ^{10}B, and FLiBe. For these 2-D Control Rod (CR) models, we can extend Region 10 to the starting position of the banked rods before the transient (2.21 m) and "hide" the lower follower. We can then move the gray curtain to the fully withdrawn position (6.5 m) and adjust the ^{10}B content in the lower follower to match exactly the eigenvalue of the 3-D reference model. This allows a similar reactivity insertion between the two models.

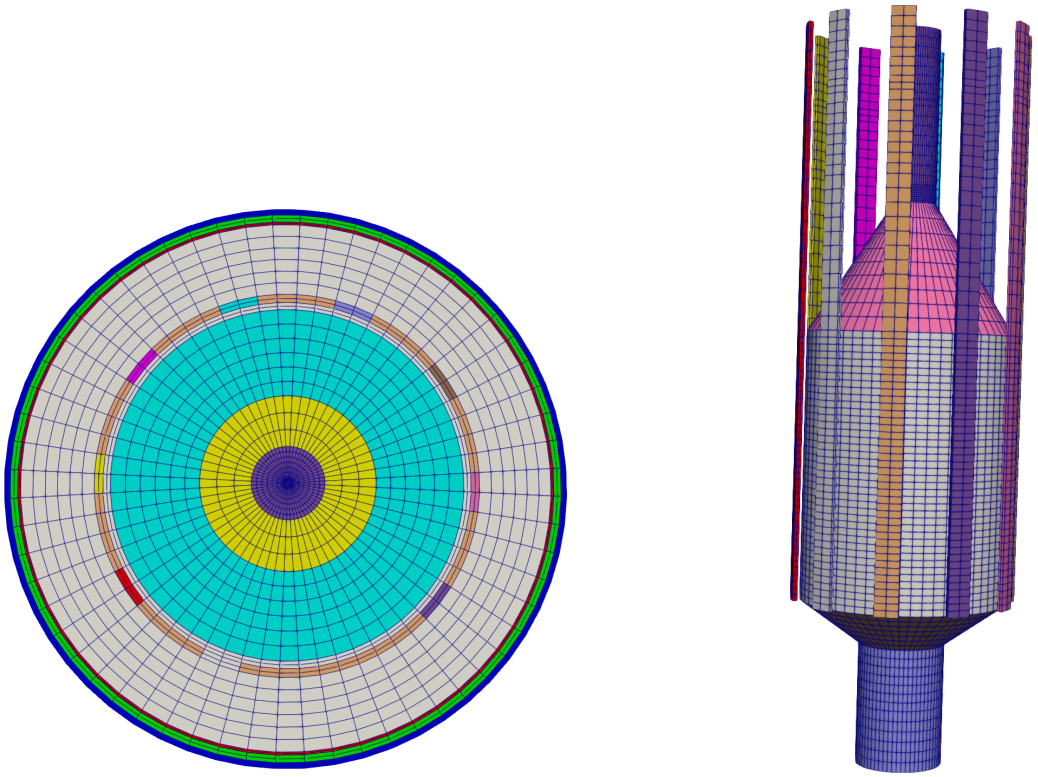

Figure 9. Computational mesh for 3-D simulations with homogenized control rod regions, showing radial and azimuthal discretization.

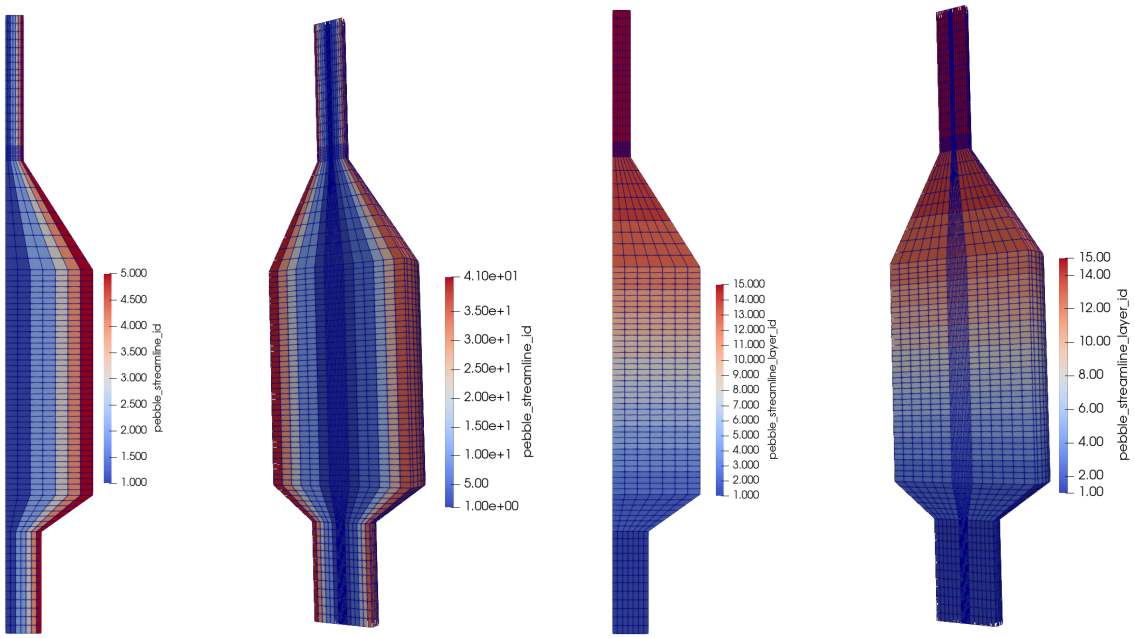

Figure 10. Visualization of the 5 pebble streamlines and 15 pebble streamline layers for the 2-D and 3-D models.

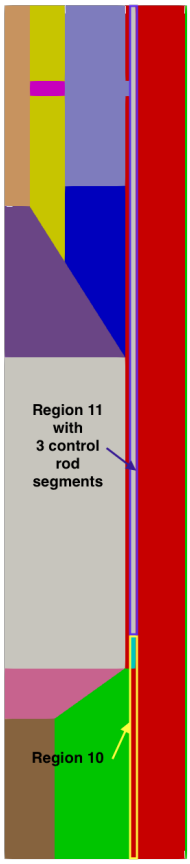

Figure 11. Equivalent 2-D model methodology.

2.2.4. Loss-of-Forced-Circulation Transient Model

This model was specifically developed to couple to Pronghorn for the LOFC scenario. The computational mesh, represented in Figure 12, and is similar to that described in the previous section with the addition of inlet plenum, explicit fluidic diode, downcomer, and vessel regions. The primary purpose of this model is to enable recirculation of fluid within the 2-D domain directly in Pronghorn, since the changes in the fluid density directly impact the core neutronics. The porosity in the fluidic diode region is consistent with the flow area in the SAM model.

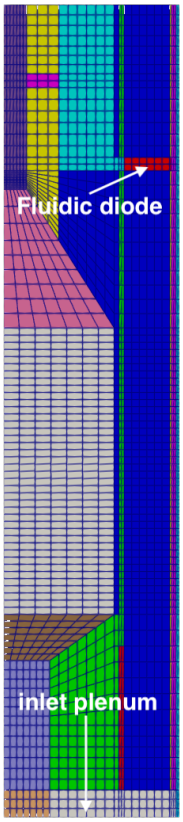

Figure 12. 2-D Griffin mesh used in the LOFC analysis.

2.2.5. Griffin Point Kinetics

The Point Kinetics Equations (PKE) can be derived from the multigroup transport equation and the delayed neutron precursor balance equation. The first assumption is to make the point reactor approximation, via separation of variables (flux factorization). In essence, we assume that only the neutron density is time-dependent and that the neutron angular flux distribution (fundamental mode eigenfunction) is time-independent:

$$\Psi_g(\vec{x}, \vec{\Omega}, t) = n(t)\Psi_{g,0}(\vec{x}, \vec{\Omega}) \tag{1}$$

After introducing the point reactor approximation, we integrate over angle, space, sum over the energy groups, and introduce a weighting function—typically the neutron importance or adjoint flux distribution—in order to arrive at:

$$\frac{dn(t)}{dt} = \frac{\rho(t) - \beta_{eff}}{\Lambda} n(t) + \sum_{i=1}^{I} \lambda_i C_i(t) \tag{2}$$

$$\frac{dC_i(t)}{dt} = \frac{\beta_{eff,i}}{\Lambda} n(t) + \lambda_i C_i(t), i = 1..I \tag{3}$$

where
n is the neutron population
t is time
ρ is the reactivity
β_{eff} is the effective delayed neutron fraction
Λ is the neutron mean generation time
C_i the concentration of the ith neutron precursor group
λ_i is the decay constant of the ith neutron precursor group.

The Griffin PKE solver can be deployed in a 0-D context to provide an approximation to the neutron transport equation. The PKE parameters Λ, β_{eff}, and λ_i can be calculated with Monte Carlo, or from deterministic methods such as Griffin. In this work, these parameters were calculated with the 3-D steady-state Griffin forward and adjoint flux solutions. Inherently, the PKE model assumes that the neutron flux shapes (forward and adjoint) do not change with time—which can be a significant approximation in some cases (e.g., control rod movement scenarios). One of the most challenging constituents of the PKE model is the reactivity model, which contains the dominant feedback physics of the reactor. Reactor designs that exhibit strong local feedback effects (strong thermalization) can be problematic, as opposed to reactors that exhibit global feedback effects (fast reactors). Traditionally, we couple a PKE model to a thermal fluids model in which we assume that the power distribution in the core does not change significantly during transient, and relies on global parameters for feedback.

Reactivity models can vary significantly in terms of complexity and the amount of effort required by the analyst. Griffin supports several reactivity modeling capabilities:

- **Separable (linear combination) model** - relies on linear interpolation methods in MOOSE, with a parametrization of independent variables that leads to an incomplete physics model since it removes correlated physics that are potentially assumed to be weakly dependent. The linear combination model does not imply that the various feedback mechanisms are treated as linear functions, since we can always use higher-order interpolation methods.
- **Partially correlated models** - use multivariate interpolation methods in MOOSE (e.g., n-linear, n-cubic, splines). Leads to an improved physics model since it includes some correlated physics, off-diagonal dependencies in a dependency matrix (state point matrix); for example, moderator temperature effects on fuel temperature feedback due to spectrum hardening.
- **Fully correlated models** - use the Stochastic MOOSE Module (STM) and the PyTorch MOOSE interface to generate a surrogate model directly usable in Griffin.

In this work, we used a linear combination model for reactivity, as shown in Equation 4, which leverages the Griffin PKE action system to add the various components of the feedback:

$$\rho(t) = \rho_{cr}(cr_{pos}(t)) + \rho_{fuel}(T_{fuel}(t)) + \rho_{mod}(T_{mod}(t)) + \rho_{ref}(T_{ref}(t)) + \rho_{cool}(D_{cool}(t)) \tag{4}$$

where

ρ_{cr} is the reactivity inserted by the control rod as a function of position cr_{pos}

ρ_{fuel} is the reactivity inserted due to the change in fuel temperature T_{fuel}

ρ_{mod} is the reactivity inserted due to the change in moderator temperature T_{mod}

ρ_{ref} is the reactivity inserted due to the change in reflector temperature T_{ref}

ρ_{cool} is the reactivity inserted due to the change in coolant density D_{cool}.

2.2.6. Reactor Physics Assumptions and Limitations

The following assumptions are made:

1. The multigroup neutron diffusion equation provides an accurate flux solution in the core and reflector regions for equilibrium core and time-dependent calculations, and a 3-D model of the core with the diffusion solver is sufficient to provide a reference calculation for the purpose of these comparisons. Reference solutions based on 3-D discrete ordinates (SN) are recommended for future work.

2. The control rod regions are homogenized with some reflector graphite for the diffusion solver and do not currently use an equivalence method in the 3-D model. In addition, the gray curtain in the 2-D model is not corrected using equivalence methods. This is left for future work.

3. No streaming correction is applied to the pebble region. Although, we could apply a Lieberoth-type [19] streaming correction, the theory was derived for cavities with non-interacting media; therefore, it might overestimate the streaming in the PB-FHR core. The Griffin online cross-sections method includes an accurate streaming correction based on the Benoist method [20], and will be deployed in future work.

4. A 2-D R-Z representation of the reactor core is used in some analyses, and constitutes an adequate representation of the reactor geometry

5. The multigroup cross sections are prepared using an infinite reflected domain in the lattice physics calculation. The intra-core neutron leakage significantly affects the local spectrum and will have an impact on the cross-section condensation and homogenization [21]. Nevertheless, cross sections serve as an initial set for performing preliminary calculations until we deploy the more sophisticated methods now available in Griffin [17].

6. A flux-limited approximation [22] of the isotope transport cross sections is sufficient to build acceptable diffusion coefficients for this reactor.

7. A 1-D streamline depletion is sufficient to capture the pebble flow, since experiments show that the flow is axially dominated [23].

8. The equilibrium salt isotopic composition is approximated and not directly calculated in Griffin.

9. The control rod and control rod channel cross sections do not include the density dependence for the FLiBe coolant. This effect is assumed to be small.

10. In the PKE model, we assume that the neutron flux shape (forward and adjoint) do not change with time.

2.3. Core Thermal Fluids Modeling Approach And Assumptions

No detailed information on the thermal fluids design for the PB-FHR can be found beyond what is provided in [1, 2, 24, 25]. Additional approximations necessary to develop a model for steady-state and transient analyses are described in the following sections. The SAM numerical and analysis methodology is described in Section 2.3.1, and the Pronghorn numerical and analysis methodology is detailed in Section 2.3.2.

2.3.1. SAM 2-D Core Model

To improve the overall fidelity of the PB-FHR transient modeling, an effort was made to couple SAM with the Griffin code so as to capture the spatial dynamics effects in this work. The SAM model in the coupled simulation includes a 2-D R-Z symmetric core region and core-external components in 0-D/1-D. The reactor core is modeled as a 2-D R-Z axisymmetric porous media flow by using heat conduction models in SAM, which includes the pebble-bed core, graphite reflector, core barrel, and vessel, as shown in Figure 13. The corresponding mesh used for the SAM 2-D core model is also shown in Figure 13. The material properties and porosity values applied in each region are listed in Table 17. Blocks 1–8 were modeled using the porous media flow model, which contains mixtures of coolants and solids. This allows the fuel pebbles or porous graphite to be modeled alongside the primary salt. Blocks 1 and 7 correspond to the fueling and defueling chutes, respectively. The pebble movement due to fueling and defueling is not modeled, such that the pebble bed is treated as static. Blocks 2 and 8 represent inlet and outlet annulus regions, through which the fluoride salt enters and exits the core via channels in the graphite blocks. Due to limited design details on these regions, they were assumed to have the same porosity as the core. Blocks 9 through 14 were treated as solid regions and only the heat conduction model was applied in these blocks. Blocks 10 and 11 are the control rod channel, which is modeled with heat conduction in the SAM 2-D core model. The fluid flow in the control rod channel and engineered bypass channel is not explicitly modeled in the 2-D domain; instead, it is represented by a 1-D fluid component in the SAM primary loop model. Heat transfer between this 1-D fluid component and the side reflector are handled using SAM's capability for modeling multi-scale heat transfer between fluid and structures. Likewise, the downcomer is not modeled in the SAM 2-D domain, but is modeled with the 1-D fluid component in the SAM loop model.

Table 17. Porosity and material in the SAM 2-D core model.

Region No.	Region name	Material	Porosity
1	Fueling chute	Pebbles	0.388
2	Inlet annulus	Graphite	0.388
3	Lower cone	Pebbles	0.388
4	Pebble-bed cylindrical core	Pebbles	0.388
5	pebble-bed cylindrical core near wall	Pebbles	0.407
6	Upper cone	Pebbles	0.388
7	Defueling chute	Pebbles	0.388
8	Outlet annulus	Graphite	0.388
9	Upper reflector	Graphite	0.000
10	Control rod channel	Graphite	0.000
11	Control rod channel	Graphite	0.000
12	Side reflector	Graphite	0.000
13	Core barrel	Stainless steel	0.000
14	Vessel	Stainless steel	0.000

In the pebble-bed region, along with the porous media flow model, the SAM multiscale pebble model was applied. The original porous media model solid-phase energy equations were extended to include the modeling of pebble temperature in 1-D spherical coordinates. In this model, all the pebbles in a representative elementary volume are represented by a "representative pebble." The pebble surface energy balance equation and an additional 1-D pebble heat conduction equation are solved. Further details on the equations are given in [26]. For this work, the pebble was divided into three layers: an unfueled pebble core, an annular fuel layer, and an outer shell layer. The 1-D mesh utilized in the 1-D pebble heat conduction calculations is presented in

1. Fueling chute
2. Inlet annulus
3. Lower cone
4. Pebble bed cylindrical
5. Pebble bed near wall
6. Upper cone
7. Defueling chute
8. Outlet annulus
9. Upper reflector
10. Control rod channel
11. Control rod channel
12. Side reflector
13. Core barrel
14. Vessel

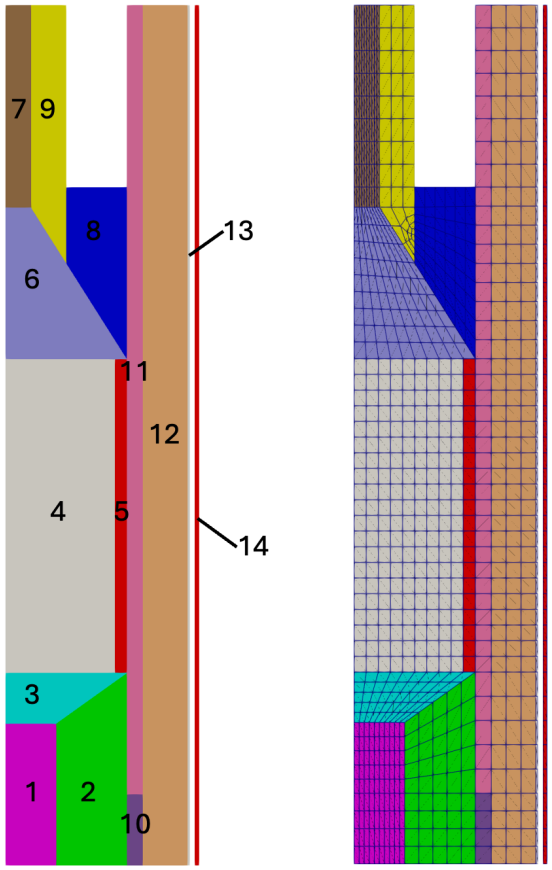

Figure 13. SAM 2-D core geometry with block labeled (left) and mesh (right).

Figure 15. Different material properties were applied in different layers, and power was only applied in the fuel layer. With the calculated pebble temperature, the TRISO fuel kernel temperature was calculated with the simplified lumped mass heat transfer model in SAM, which is based on the lumped model for coated particles in the TINTE code [27].

For the thermophysical properties of the fluoride salt FLiBe, the SAM model utilizes built-in temperature-dependent correlations from UC Berkeley [28]. Constant properties are applied for the solid materials, as listed in Table 18.

Table 18. Solid thermophysical properties in the SAM 2-D core model.

Material	Density [kg/m^3]	Thermal Conductivity [W/(m·K)]	Heat Capacity [J/(kg·K)]
Stainless Steel	8000	21.5	500
Pebbles	1631	15	1697
Graphite	1740	26	1697

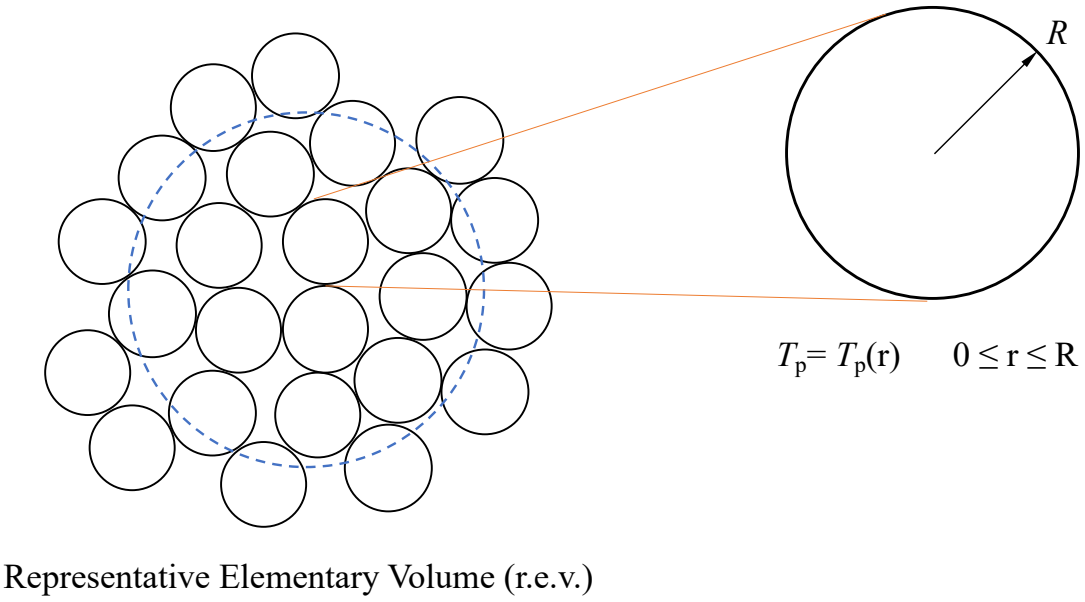

Figure 14. The concept of a representative elementary volume (r.e.v.), illustrated in the pebble-bed condition: the r.e.v. is represented by a dashed circle at the left, and an enlarged representative pebble in the r.e.v. is shown at the right [29].

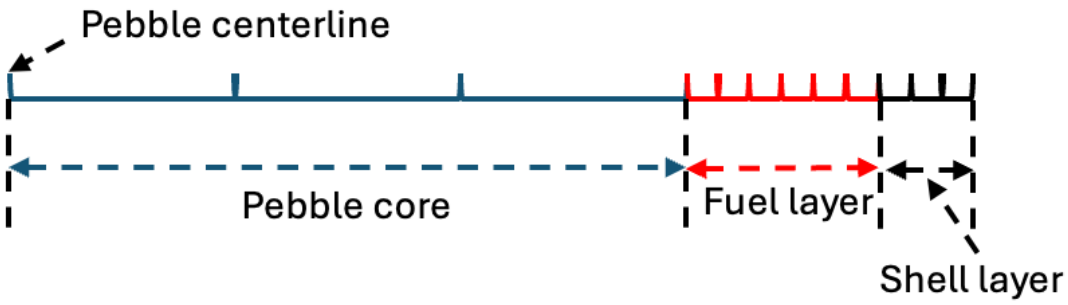

Figure 15. 1-D mesh utilized in the SAM multiscale pebble model.

2.3.2. Pronghorn 2-D Core Model

The 2-D Pronghorn core thermal fluids mesh used in the control rod withdrawal scenarios and in the Loss of Forced Circulation (LOFC) scenarios are shown in Figure 16. Note there are some differences between the two geometric models. The control rod withdrawal model used in the 3-D and 2-D comparisons includes a core inlet flow boundary at the bottom of the geometry below the fueling chute and inlet annulus. Furthermore, the downcomer and vessel are omitted. The LOFC model includes a core inlet flow boundary at the top of the downcomer and explicitly adds the downcomer, inlet plenum, fluidic diode, and vessel. In this model, there is no bypass flow via the control rod, as it would interfere with the diode. The ability to model the control rod and diode explicitly will be added in the near future by the NEAMS program.

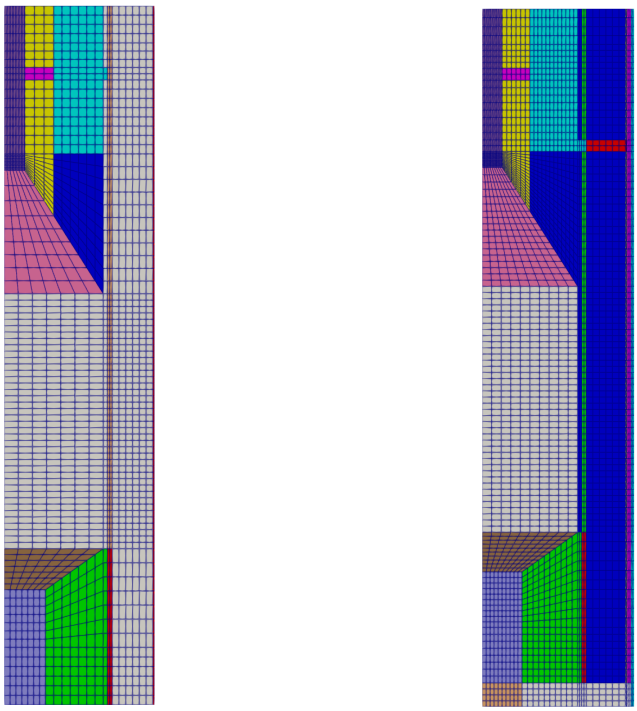

(a) Control rod withdrawal scenarios

(b) Loss of Forced Circulation (LOFC) scenarios

Figure 16. 2-D Pronghorn mesh.

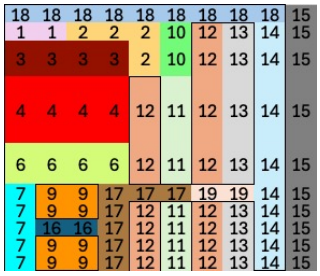

Figure 17. Region assignments for the Pronghorn PB-FHR model. Note that region 18 is at the bottom of the core.

The conceptual geometry of the PB-FHR model is shown in Figure 17. The region identification values shown in Figure 17 can be used as keys in Table 19,which summarizes the parameters and closure correlations used in each region.

Areal heat transfer coefficients h computed via the Dittus-Boelter correlation were converted to volumetric heat transfer coefficients α by:

$$\alpha = \frac{A_{HT}}{V} h, \tag{5}$$

where A_{HT} is the heat transfer area of the region and V is the volume of the region. For the downcomer, no solid is present; therefore, the heat transfer coefficient is instead used for interface conjugate heat transfer between the downcomer fluid and the surrounding structure.

ID	Name	Porosity	D_H	κ_s	κ_f	Drag	α
1	Fueling chute	0.39	0.04	PBR κ_s^a	Peclet dependentκ_f	KTA	Wakao
2	Inlet annulus	0.39	0.1	k_s^*	k_f	Churchill	0
3	Lower cone	0.75	0.04	PBR κ_s^a	Peclet dependentκ_f	KTA	Wakao
4	Cylindrical bed	0.401	0.04	PBR κ_s^a	Peclet dependentκ_f	KTA	Wakao
5	Cylindrical bed near wall	0.401	0.04	PBR κ_s^a	Peclet dependentκ_f	KTA	Wakao
6	Upper cone	0.75	0.04	PBR κ_s^a	Peclet dependentκ_f	KTA	Wakao
7	Defueling chute						
8	Outlet annulus	0.39	0.8	k_s^*	k_f	Open	0
9	Upper reflector	0	—	Eq. 6	—	—	—
10	Control rod bypass	0.3	0.058	Eq. 6	k_f	Churchill	D-B
11	Control rod bypass	0.3	0.058	Eq. 6	k_f	Churchill	D-B
12	Side reflector	0	—	Eq. 6	—	—	—
13	Barrel	0	—	21.5	—	—	—
14	Downcomer	0.3	0.1	k_s^*	k_f	Churchill	0
15	Vessel	0	—	21.5	—	—	—
16	Upperchute to hotwell link	0.39	0.8	k_s^*	k_f	Open	0
17	Hot well	0.39	0.8	k_s^*	k_f	Open	0
18	Inlet plenum	0.39	0.9	k_s^*	k_f	Open	0
19	Diode 1	0.03	0.14	k_s^*	k_f	see description in text	D-B

[a] Radiation: Breitbach-Barthels, Conduction: Chan-Tien, Fluid conduction: ZBS

Table 19. Modeling parameters and closure relations used in the Pronghorn PB-FHR model, where D_H is the characteristic length of each region, κ_s is the effective solid thermal conductivity, κ_f is the effective fluid thermal conductivity, and α is the volumetric heat transfer coefficient. Regions with a porosity equal to zero have no defined flow variable.

The pebble thermophysical properties in Pronghorn were approximated with temperature- and fluence-dependent models based on Equations 6 and 7 [21, 30]. The density of the graphite pebble was assumed to be 1631.59 $[kg/m^3]$, which was adjusted to account for differences in density between the core, matrix, and shell regions of the pebble. In the future, these values need to be integrated with the values computed in the BISON model.

$$k_{peb} = 127.68 * (\frac{-0.03906 * \frac{T_C}{1000} + 0.06829}{\Gamma + 0.1931 * \frac{T_C}{1000} + 0.105} + 0.1228 * (\frac{T_C}{1000} + 0.042)) \tag{6}$$

$$c_p = (0.645 + 3.14 * (\frac{T_C}{1000}) - 2.809 * (\frac{T_C}{1000})^2 + 0.959 * ((\frac{T_C}{1000})^3) * 1000.0 \tag{7}$$

where

Γ = fluence in $1 \times 10^{25} m^{-2}$ dido nickel equivalent (DNE) units

T_C = temperature in Celsius.

The reflector thermophysical properties in Pronghorn were approximated with temperature- and fluence-dependent models based on Equations 8 and 7 [21, 30]. The graphite density was 1740.0 $[kg/m^3]$.

$$k_{ref} = 115\Big((1.5648 - 0.3162 log_{10}(T + 100)\Big) \cdot \Big(\frac{(-0.0054705 + 0.00038214T' + 0.13487T'^2)}{(\frac{T}{10} - (-0.013951 + 0.12064T' - 0.32955T'^2))} - 0.07264 + 0.41459T' + 0.23149T'^2\Big) \tag{8}$$

where $T' = (T/1000)$, and T is in K.

The pebble and TRISO particles were modeled with 1-D steady-state solid conduction by using BISON and Pronghorn. The thermal conductivities for the various materials are shown in Table 20. Note that the effective thermophysical properties for the TRISO and fueled regions of the pebble use the composite material theory described in the Pronghorn manual [10]. In the simplified model used to compare the Pronghorn results to SAM, we only applied a temperature dependence on the fuel kernel. The conductivities in each layer are provided in Table 20. Temperature, burnup, and fluence dependence were used in the other calculations, and the conductivities in each layer are provided in Table 21. Griffin does not currently include the unit of Fissions per Initial Heavy Metal Atom (FIMA) or a neutron fluence value in the pebble-bed reactor action system that is used to set up the pebble depletion problem. The NEAMS program plans to have this technology in Griffin next year. Nevertheless, we can use the DRAGON calculations to approximate the value of FIMA via Equation 9, and the fast fluence (>0.8 MeV) with Equation 10.

$$\%FIMA = \frac{Bu \cdot 24 \cdot 3600 \cdot 1000 \cdot 100}{Bu_{conv} \cdot JMeV \cdot e_{fiss} \cdot atg} \tag{9}$$

$$\Gamma = 3.928\,39 \times 10^{-31} Bu^2 + 1.510\,22 \times 10^{-15} Bu \tag{10}$$

where

Bu = burnup in $\frac{J}{m^3}$

Γ = fluence in $1 \times 10^{25} m^{-2}$ DNE units

$e_{fiss} = 194.0 \frac{MeV}{fission}$

$JMeV = 1.602\,176\,634 \times 10^{-13} \frac{J}{MeV}$

atg = atoms per gram uranium = $2.5357 \times 10^{21}\ \frac{atU}{gU}$

Bu_{conv} = burnup conversion = $8.782\,569\,077 \times 10^{12} \frac{J \cdot kg}{m^3 \cdot MWd}$.

We imposed a Dirichlet boundary condition on both the pebble and TRISO models and enforced the average homogeneous surface temperature from the porous medium solution on the pebble surface, and the pebble fuel region average temperature on the TRISO surface. In addition, we used a quasi-static assumption that, though it does not account for the thermal inertia of the pebble and the TRISO, allows for simpler coupling and introduces negligible error. More complex coupling approaches are left for future work. Typical solutions for the pebble and TRISO temperature fields are shown in Figure 18.

Table 20. Thermal conductivity of the various pebble and TRISO materials for the simplified model against which to compare SAM.

Material	Value [W/m/K]
Kernel	$\frac{1.0}{(0.035+2.25e-4*t)} + 8.30e-11*t^3$
Buffer	0.7
PyC	4.0
SiC	16.0
Matrix and shell	32.4
Core	30.0
TRISO effective	Composite solid properties series mixing
Pebble fuel region effective	Composite solid properties Chiew mixing

Table 21. Thermal conductivity of the various pebble and TRISO materials with temperature- and irradiation-dependent models.

Material	Value [W/m/K]	References
Kernel	$(0.0132e^{0.00188T_C} + \frac{4040}{464+T_C}) f_d f_p f_{por} f_r$	[31–34][1]
Buffer	$244.3 T_K^{-0.574} f_{por} f_r$	[35–39][2]
PyC	$244.3 T_K^{-0.574} f_{por} f_r$	[35–39][2]
SiC	$(\frac{17885}{T} + 2.) * exp(-0.1277\Gamma)$	[40]
Matrix and shell	$32.4 * (1 - 9.7556 \times 10^{-4} * (T_C - 100) * e^{-6.036 \times 10^{-4} T_C}) f_{por} f_r$	[41][2]
Core	$30.0 * (1 - 9.7556 \times 10^{-4} (T_C - 100) e^{-6.036 \times 10^{-4} T_C}) f_{por} f_r$	[41][2]
TRISO effective	Composite solid properties series mixing	[10]
Pebble fuel region effective	Composite solid properties Chiew mixing	[10]

[1] In the BISON UCO model, the functional relationships are assumed to be the same as for UO_2 (Miller and Nabielek [31, 32]). For the correction factors, we used the Fink-Lucuta [33, 34], model dissolved fission product (f_d), precipitated fission product (f_p), porosity (f_{por}), and radiation damage (f_r) correction factors.

[2] The porosity correction factor $f_{por} = \frac{\rho}{\alpha(\rho_{TD} - \rho) + \rho}$ with $\alpha = 2.2$, where ρ_{TD} is the theoretical material density. The irradiation correction factor is of the form $f_r = (1. - 0.336 * (1. - e^{-1.005\Gamma}) - 0.035\Gamma)$ (similar to models developed in the German program by Nabielek), where the neutron fluence is in $1 \times 10^{25} m^{-2}$ DNE units.

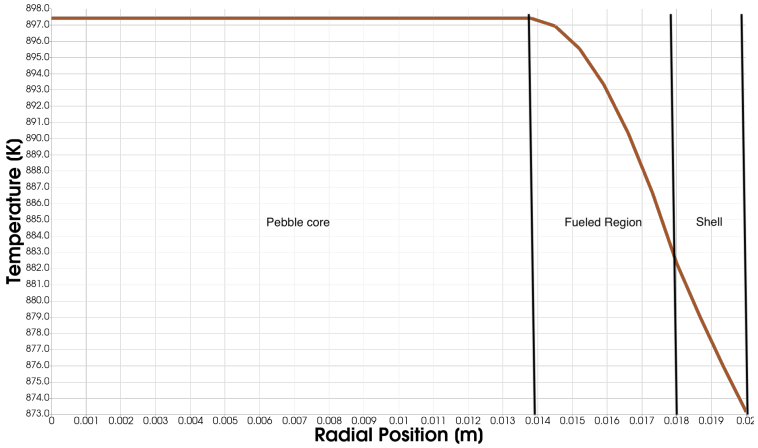

(a) Pebble temperature

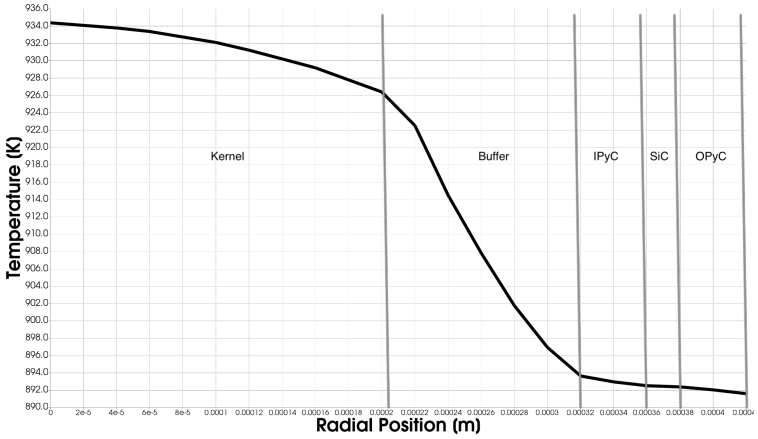

(b) TRISO temperature

Figure 18. Temperature profiles for the PB-FHR pebble and TRISO designs with an assumed power density of 5.0×10^7 W/m^3.

The assumptions and limitations applicable to the Pronghorn **thermal fluids model** are as follows:

1. Porous medium equations capture most of the important effects in the core.
2. The flow in the plena is approximated due to a lack of detailed information about the geometry and will require either empirical or CFD-computed closure models to be further improved, but is not expected to significantly change the core temperature results. Drag and heat transfer correlations for these regions are only estimations for the purposes of this work.
3. Wall effects for convection, radiation, and conduction heat transfer are approximated, not explicitly treated.
4. Convective heat transfer between the core fluid and the reflector wall is not explicitly treated. Instead, it is modeled in the effective solid conductivity closure.
5. Slip-wall and symmetry boundary conditions are used for the fluid mass, momentum, and energy equations.
6. All walls have zero-flux boundary conditions for the fluid temperature, and the conjugate heat transfer is treated as a porous-media volumetric phenomenon. The one exception to this is with the downcomer, as there is no solid in the downcomer of the PB-FHR. Conjugate heat transfer is considered between the downcomer fluid and the barrel/vessel walls in the downcomer.
7. The solid energy equation boundaries are all adiabatic except for the outside of the vessel.
8. The volumetric friction diode requires a significant friction correction. Transition to a wall flow diode will remove this requirement in the future.
9. Radiative and conduction boundary conditions were applied between the vessel and RCCS.
10. The RCCS temperature is constant and set to 20^oC.
11. In regions containing very little solid material, the solid thermal conductivity is set to $k_s^* = 10^{-4}$.
12. We use the molecular thermal conductivity of the fluid (k_f) instead of the effective fluid conductivity, except for cases when we have a good model for the effective thermal conductivity (i.e., in the bed).
13. Heat transfer between the downcomer salt and the solid structure is handled as interface conjugate heat transfer.
14. Dittus-Boelter (DB) is used for modeling heat transfer between solid and fluid regions.
15. In large open flow regions, we use a constant Forchheimer coefficient of 1.25. This corresponds to about 1 kPa of pressure drop per meter under forced flow conditions.

The following assumptions are applicable to the BISON **pebble and TRISO thermal model**:

1. A thermal equilibrium approximation was considered in pebble simulations during transient calculations, so using the quasi-static approximation in the pebble and TRISO thermal conduction problem is acceptable for slow transients, as the two will be in thermal equilibrium. In fast reactivity insertion transients, which are not typically considered for pebble-bed reactors, the Pronghorn solid conduction solution includes the time-dependent term so as to compute the surface temperature, thus providing a degree of correction on the time delay for steady state.

2. Several sources of heat transfer heterogeneity around the pebble were ignored: the coolant flow orientation, pebble-to-pebble contact, pebble-to-reflector contact, and radiation.

3. A Dirichlet boundary condition is set at the pebble surface to obtain the moderator temperature, and is assumed to provide reasonable solutions, though it will not strictly conserve energy.

4. A Dirichlet boundary condition is set at the TRISO surface to obtain the fuel temperature, and is assumed to provide reasonable solutions, though it will not strictly conserve energy.

5. The thermophysical properties for the fuel kernel are based on UO_2 data, so ideally we would need to use uranium oxycarbide data.

2.4. Loops And Secondary-Side Modeling Approach And Assumptions

In the primary loop modeling, the external flow circuit was modeled with 0-D and 1-D SAM fluid components. The primary pump was modeled with SAM 0-D *PBPump* components. For steady-state simulation under normal operating conditions, the pump head was adjusted to 0.15 MPa to achieve the designed core flow rate of 1324.6 kg/s. Downstream of the pump was the intermediate heat exchanger, modeled using the *PBHeatExchanger* component so as to represent a countercurrent design heat exchanger. In this model, the downcomer was modeled with the 1-D fluid component in SAM. The heat transfer between the downcomer and the core barrel, and the downcomer and the reactor vessel, were modeled using SAM's multi-scale capability for heat transfer between fluid and structures. The fluidic diode was modeled with the *CheckValve* component in SAM. One pipe connects the outlet plenum to the fluidic diode, and another connects the fluidic diode to the downcomer. During normal operating conditions, the *CheckValve* is closed because of the pressure difference, so no flow is passed through the fluidic diode. After the primary pump stops operating, the *CheckValve* opens due to loss of pressure difference, such that a flow path through the fluidic diode can be established for natural circulation between the hot core and cold downcomer regions. In the secondary loop, a *PBPump* component was used to model the secondary pump, and the secondary heat exchanger was simplified to be modeled with the 1-D fluid component *PBOneDFluidComponent*.

A water-cooled RCCS loop was modeled outside the reactor vessel. Heat was removed from the core through radiative heat transfer between the RCCS cooling panels and the outer surface of the reactor vessel wall. The radiative heat transfer between the RCCS and the outer surface of the reactor vessel wall was modeled with the *NearestNodeRadHeatTransferConstraint* in SAM. A *PBCoupledHeatStructure* was placed between the riser of the RCCS loop and the reactor vessel wall. One surface of this heat structure was coupled to the riser of the RCCS loop through convection heat transfer, and the other surface was coupled to the reactor vessel wall through the *NearestNodeRadHeatTransferConstraint* for radiative heat transfer. Due to the passive nature of the RCCS, there was no pump in the RCCS loop. The water from the riser came to the RCCS heat exchanger, through which water transferred the heat to the air in the secondary side. A *PBHeatExchanger* component was used to simulate the RCCS heat exchanger, and the secondary side of the RCCS heat exchanger was given pressure and temperature boundary conditions at both the inlet and outlet.

2.5. Coupling Approach And Assumptions

2.5.1. Thermal Fluids Coupling

For practical nuclear engineering applications, multi-scale thermal fluid analysis achieved by adopting the combined uses of different-scale computational tools (e.g., System Thermal-Hydraulics (STH) and CFD codes) is vital when 3-D effects play an important role in the evolution of a given transient or accident scenario. Most commonly, multi-scale coupling of STH and CFD is performed by partitioning the simulation domain

into two separate domains: one handled by STH and the other by CFD. This is often referred to as the domain decomposition approach. Coupling of this approach is realized via data exchange at the boundaries/interfaces of the two separate domains. This type of coupling scheme is often simple to implement, but care must be taken to ensure numerical stability and accuracy. Because of the strong pressure-velocity coupling, iterations (e.g., fixed-point Picard iterations with relaxations) between two different codes are required to achieve the desired convergence in both codes and to ensure stability of the coupled system. The potentially large number of iterations due to the low convergence rate of the fixed-point iteration method at each time step is a limiting factor in practical simulations.

In this work, to overcome the limitations of the traditional domain decomposition approach for the multi-scale thermal fluid coupling, we adopted two approaches, the single-solve approach and the domain-overlapping approach, both of which will now be discussed in detail.

2.5.1.1 SAM Single-Solve Approach

A novel single-solve [42] approach was implemented in SAM to couple the SAM multi-D and 1-D/0-D domains. In the SAM single-solve approach, instead of solving the multi-D flow equations and 1-D flow equations separately (and then coupling both modules through explicit boundary information exchange), the SAM multi-D/1-D integrated coupling model was solved in a fully coupled, fully implicit manner. A single combined computational domain (i.e., computational mesh) was used to represent the whole system, with part of the computational domain being modeled in multi-D (e.g., the reactor core), and other parts in 1-D (e.g., the primary and secondary flow loops). Different governing equations (e.g., multi-D Navier-Stokes/porous-media-flow equations and 1-D flow equations) were solved in different domains. After discretization of the whole computational domain, the discretized governing equations were condensed into a combined nonlinear residual vector for solving unknown variables. Constraint equations were added to connect the multi-D and 1-D boundaries and enforce the mass, momentum, and energy balance across these boundaries/interfaces. All these coupling operations were achieved at the nonlinear residual level, without the need for explicit boundary information exchange. Numerical stability and convergence are guaranteed by appropriate implementation of Jacobian entry-related degrees of freedom that lie in the coupling boundaries. The integrated model can be solved in a fully coupled manner using Newton's method, such that iterations between the multi-D flow module and 1-D flow module can be avoided so as to reduce the total computational cost.

Coupling between the multi-D fluid domain and the 1-D fluid domain at the coupling boundaries was achieved through special 0-D coupled volumes that take inflow/outflow from either multi-D flow boundaries or 1-D fluid channel ends. Figure 19 shows schematically the design of a coupled volume branch in the integrated coupling model, with multiple connections. The integrated primary loop model with single-solve approach in SAM for PB-FHR is illustrated in Figure 20. To couple the multi-D region and 1-D fluid domain with the single-solve approach in SAM, two *CoupledVolumeBranch* components, representing the inlet plenum and hotwell, were placed at the downcomer outlet and the core outlet, through which the two domains are connected at the boundaries. Furthermore, the conjugate heat transfer between the 1-D downcomer and multi-D core barrel, 1-D downcomer and multi-D reactor vessel, and 1-D control rod channel and multi-D reflector were modeled by adding three SAM *ConvectiveHeatTransfer* components between the multi-D solid and 1-D fluid domains.

2.5.1.2 SAM Domain-Overlapping Approach

To address the numerical stability and accuracy issue, another type of STH/CFD coupling scheme, referred to as the domain overlapping approach, was proposed. In this approach, the entire domain is simulated in the system analysis code, and part of the domain is also simulated with the CFD code. Coupling between STH and CFD is still realized by data exchange between the two codes. Compared with the domain decomposition approach, there is a significant difference in what kinds of data are being exchanged. In the domain-overlapping approach, when CFD data are transferred to STH,

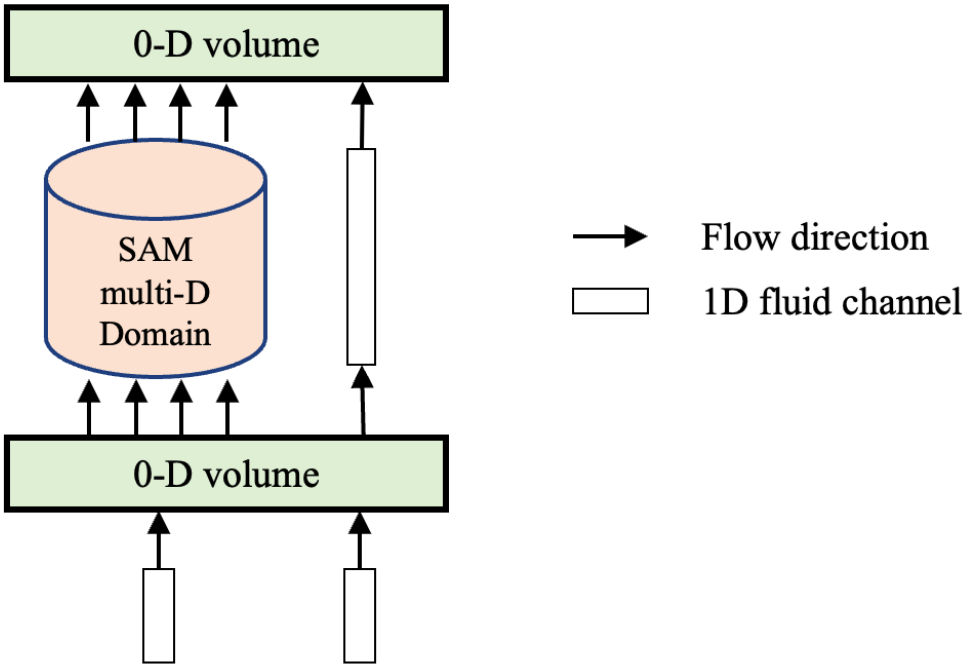

Figure 19. Schematic diagram of the single-solve coupling approach between the multi-D and 1-D domains in SAM.

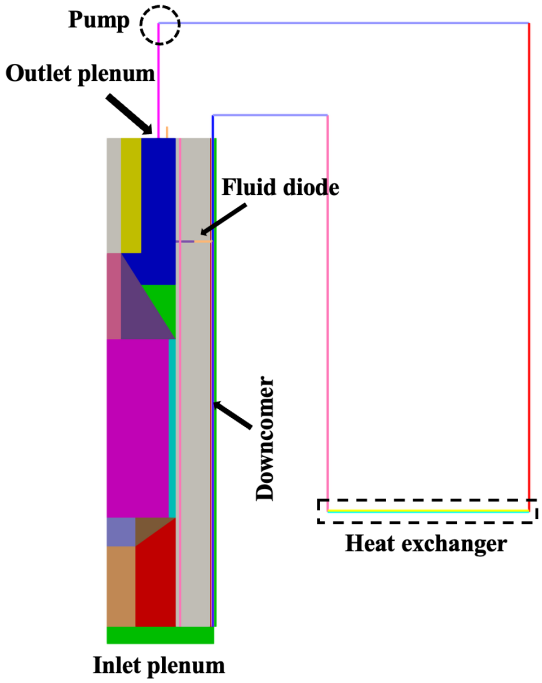

Figure 20. Primary loop model of SAM with single-solve approach.

they often appear as volumetric source/sink terms (e.g., the friction factor in the momentum equation and the volumetric heat source term in the energy equation). The difference between the domain decomposition and domain-overlapping approaches is illustrated in Figure 21.

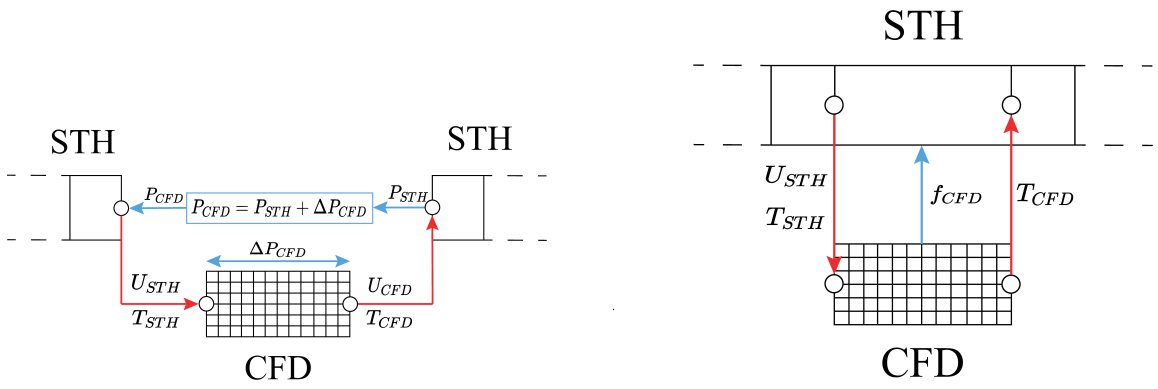

Figure 21. Coupling schematics for the domain decomposition (left) and domain-overlapping (right) methods [43].

The domain-overlapping approach has been demonstrated to be numerically more stable and robust, but often requires modifications to the source code. For the SAM code, the original effort of implementing the domain-overlapping coupling was supported by an NEUP project [44]. Using the domain overlapping approach, many successful applications have been demonstrated with SAM as the system analysis code, coupled to CFD tools such as Nek5000/NekRS [43] and STAR-CCM+ [45].

In this work, the PB-FHR is a much more complex system than what is illustrated in Figure 21. The multi-scale couplings occur in a few places, including the coupling between the 1-D primary loop and the multidimensional core model, the conjugate heat transfer between the 1-D downcomer and the multidimensional core model, and the thermal radiation between the multidimensional core vessel outer surface and the 1-D RCCS model. To successfully model PB-FHR in a multi-scale simulation, care must be taken to ensure that all the couplings are appropriately handled. In the SAM/SAM domain-overlapping setup illustrated in Figure 22, the MainApp includes the multidimensional core part, the RCCS, and the thermal radiation heat transfer between the reactor vessel outer wall and the RCCS panel. The SubApp includes the entire primary heat transport system, which includes a 1-D surrogate core model, a key component for realizing the domain-overlapping scheme. The conjugate heat transfer between the 1-D downcomer, modeled in the SubApp, and the multidimensional core barrel and reactor vessel, modeled in the MainApp, as illustrated in Figure 23 (left), is realized by a more standard MultiApp approach. In such an approach, as illustrated in Figure 23 (right), surface temperatures from multidimensional solid structures are transferred to the 1-D flow channel as wall temperatures. The fluid domain heat transfer is then modeled using SAM's *HeatTransferWithExternalHeatStructure* component, which takes the wall temperature transferred from the multidimensional MainApp. Meanwhile, fluid temperatures and heat transfer coefficients are transferred back to the multidimensional domain to set up a Neumann-type heat transfer boundary condition. The multidimensional wall surface heat transfer is then modeled using the *CoupledConvectiveHeatFluxBC* object, which takes the fluid temperatures and heat transfer coefficients transferred from the 1-D SubApp. More detailed discussions on the MultiApp conjugate heat transfer can be referred to in previous publications [46, 47].

The complexity of the PB-FHR domain-overlapping model necessitates a more detailed description of the MultiApp setup pertaining to the domain-overlapping scheme. Figure 24 illustrates the major components and data transferring between the MainApp and SubApp of the domain-overlapping setup.

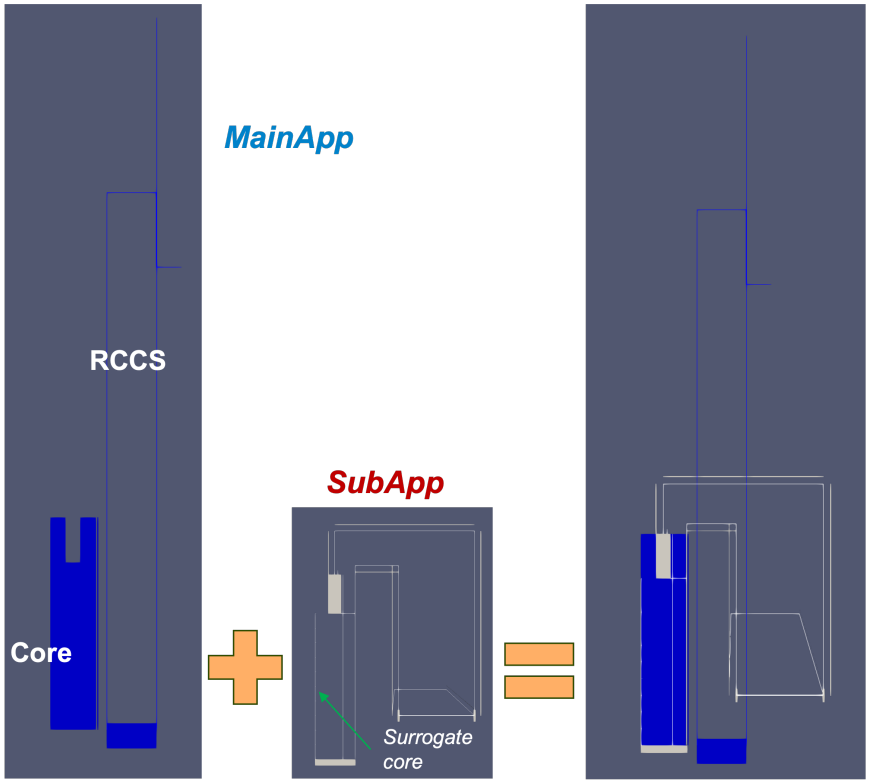

Figure 22. SAM/SAM domain-overlapping scheme for the PB-FHR simulation.

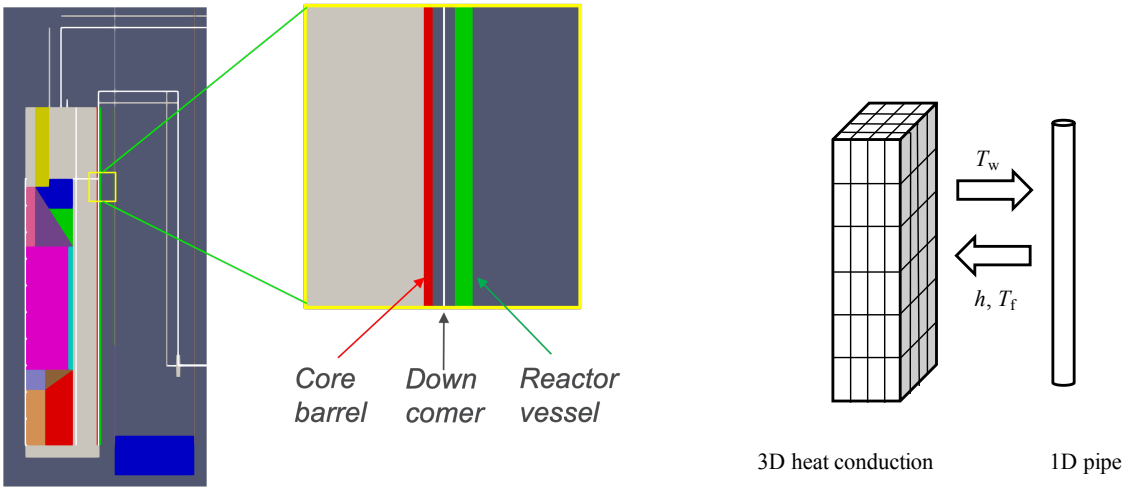

Figure 23. Conjugate heat transfer MultiApp setup: (left) conjugate heat transfer between the 1-D downcomer and the multidimensional core barrel and reactor vessel; (right) scheme for MultiApp conjugate heat transfer [46, 47].

For the multidimensional core CFD part, on boundary (1) it requires inlet boundary conditions, including temperature T_{in} and velocity v_{in}, both of which are transferred from the SubApp extracted from the inlet of the surrogate core component. It is noted that the inlet velocity boundary conditions represent a necessary setup; however, they cause some slight differences when compared with the single-solve approach, which effectively uses a pressure boundary condition on the same boundary. On boundaries (2) - de-fueling chute outlet and

(3) - annulus core outlet, pressure values are required. Note that boundaries (2) and (3) are both connected to the same outlet plenum, such that their pressures are related. In this setup, a reference pressure p_{ref} is provided to boundary (3). To compensate for the hydrostatic pressure change in the outlet plenum, a pressure value of $p_{ref} - \rho_{outlet\,plenum} g \Delta h$ is provided to boundary (2), in which $\rho_{outlet\,plenum}$ is the coolant density in the 0-D outlet plenum transferred from the SubApp, and Δh is the vertical distance between boundaries (2) and (3). It is noted that, since an incompressible flow model is used, the reference pressure p_{ref} can be an arbitrary value. For the 1-D SubApp part, the core between the inlet and outlet plena is broken into two parts: the surrogate core and a very short pipe connected to the outlet plenum. The same reference pressure is set to both the outlet of the surrogate core component and the inlet of the very short pipe. The pressure drop through the surrogate core, including the total effect of both the gravity effect and frictional effect, is informed by the MainApp. In this case, the total pressure change between boundaries (1) and (3), as well as the vertical distance between the two, are used to compute an effective pressure gradient and, eventually, an effective frictional factor for the surrogate core component. Note that the pressures at boundaries (2) and (3) are already related, as discussed above, and therefore in the surrogate model, a pressure at boundary (2) is not needed. The temperature to the very short pipe, $\bar{T}$, represents the mass flow rate averaged outlet temperature from the core entering the outlet plenum. This temperature comes from the MainApp, through MultiApp data transfer, and the outlet temperature of the surrogate core is discarded. For FLiBe, the mass flow rate averaged core outlet temperature is evaluated as:

$$\bar{T} = T(\bar{h}) = \frac{\bar{h}}{c_{p,const}} \tag{11}$$

and

$$\bar{h} = \frac{(mh)_{(2)} + (mh)_{(3)}}{m_{(2)} + m_{(3)}}, \tag{12}$$

where

$$m_{(i)} = \int \rho \mathbf{u} \cdot \mathbf{dA}, \tag{13}$$

and

$$(mh)_{(i)} = \int \rho h \mathbf{u} \cdot \mathbf{dA}, \tag{14}$$

are the surface integral over boundary (2) or (3), with (i) being (2) or (3).

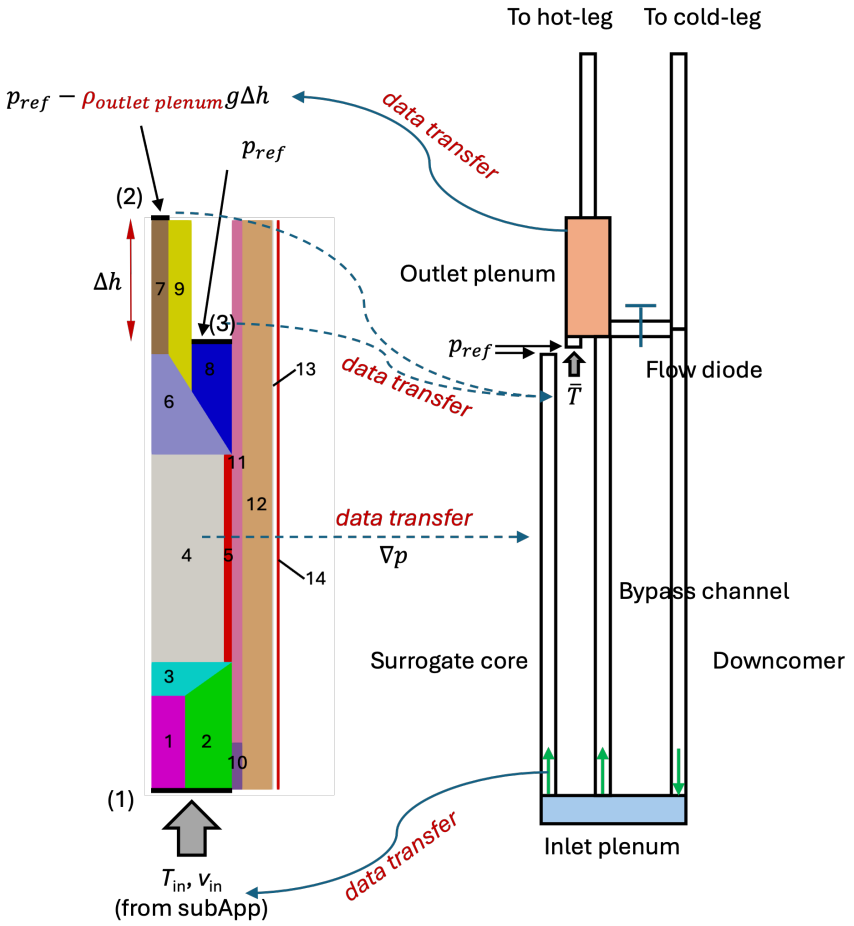

Figure 24. Detailed descriptions of the SAM/SAM domain-overlapping scheme for the PB-FHR simulation.

2.5.1.3 Pronghorn Domain-Overlapping Approach The current NEAMS effort for developing an overlapping domain coupling method is a continuation of the NEUP work used in SAM that was introduced in the previous section. The NEAMS approach utilizes Pronghorn and SAM, coupled through BlueCRAB, to perform the overlapping domain coupling, but in this case the coupling enforces mass, momentum, and energy conservation. Pronghorn performs the multidimensional simulation, and SAM performs the system-level simulation, with the exchange of information being facilitated by BlueCRAB.

The overlapping domain method, developed by the NEAMS program, to couple Pronghorn and SAM was tested in this work. In this method, an overlapped surrogate channel is placed in the SAM model to represent the overlapped multidimensional Pronghorn domain. The mass flow rate and temperature at the inlet of the surrogate component are passed to Pronghorn as inlet boundary conditions, and the surrogate outlet pressure is passed to Pronghorn as an outlet boundary condition. Pronghorn then provides the ΔP and Δh between the inlet and outlet to the coupling framework. Finally, the coupling framework determines a friction factor and heat source to produce the same ΔP and Δh in the SAM surrogate components. This is the key difference between SAM's NEUP overlapping domain approach and the current NEAMS approach. The NEUP-developed method passes the temperature at the surrogate outlet to SAM and applies it as a boundary condition. This makes the method overlapped for momentum, but essentially segregated for energy. On the other hand, the NEAMS approach is fully overlapped for both momentum and energy, as no boundaries exist in the SAM model for either momentum or energy. Rather than passing the boundary temperatures, a heat

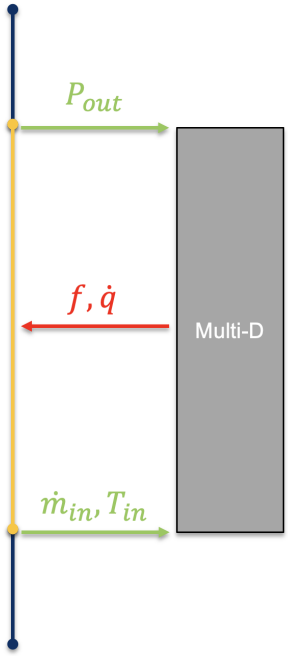

Figure 25. Exchange of information for the Pronghorn/SAM overlapping domain coupling framework. The yellow segment represents the overlapped 1-D surrogate component.

source is determined in SAM to satisfy a Δh that is consistent with Pronghorn. Fixed-point iterations are used to ensure that the two codes are consistent with each other during a given time step. An overview of these data transfers is shown in Figure 25.

This novel approach for coupling a system code to the higher dimension CFD model produced excellent solutions for the steady-state cases. Difficulties, however, were encountered during the LOFC transient, due to differences in the axial temperature profiles between the multi-D and surrogate system models. In natural circulation, there is a balance between buoyancy forces and frictional losses. If multidimensional effects cause the axial temperature profile in Pronghorn to be nonlinear, there will be a nonlinear density profile, and thus the buoyancy forces will significantly differ from what can be captured in a 1-D code. These differences in buoyancy forces between the two codes manifests as coupling instability. This issue is currently being addressed by the NEAMS program, and a solution should be available soon to better couple Pronghorn and SAM. For this reason, the domain-overlapping method is only used for coupling Pronghorn and SAM in the 2-D equilibrium core calculation that serves as the initial condition for the simple control rod withdrawal scenario. For the LOFC, boundary conditions are instead applied to approximate the effects of the loop components. Future work may apply the NEAMS overlapping domain approach to couple Pronghorn and SAM for loss-of-cooling transients.

2.5.2. Core Neutronics and Thermal Fluids Coupling

2.5.2.1 Multiphysics Coupling with SAM The Griffin neutronics model and SAM thermal-hydraulics model were coupled with the BlueCRAB and MOOSE MultiApps system [48]. The coupling scheme and data transfer between different apps are shown in Figure 27. In this coupled simulation, Griffin serves as the main application (MainApp) that solves the neutron spatial flux and streamline pebble depletion. Under the main Griffin app, the SAM MultiApp solves the thermal-hydraulics problem, including the multi-scale pebble model that solves the pebble and TRISO fuel kernel temperatures. In the Griffin model, there are nine burnup groups of pebbles, whereas in the SAM calculation only one average pebble is modeled,

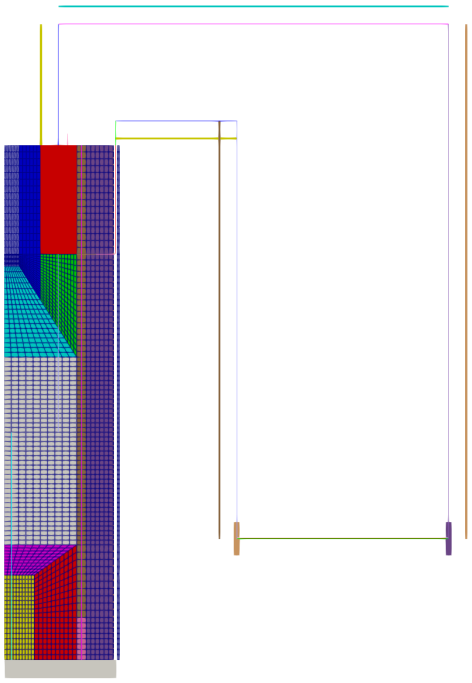

Figure 26. Overlapping domain coupling between Pronghorn and SAM.

and all nine burnup groups of pebbles are assumed to have the same temperature. In the coupled steady-state calculation, the first Griffin calculation will be initialized by the streamline depletion solver. The isotopic number density from the depletion solver is transferred back to the Griffin diffusion solver. The neutron flux and k-eigenvalue are calculated by Griffin by using the 2-D R-Z diffusion solver. The power density computed by the Griffin model is transferred to the SAM model for thermal-hydraulics calculations. The fuel and moderator temperatures of the pebble-bed, along with the reflector temperature calculated by SAM, are transferred back to the Griffin MainApp. Picard iteration is performed in the coupled steady-state calculation until convergence is achieved.

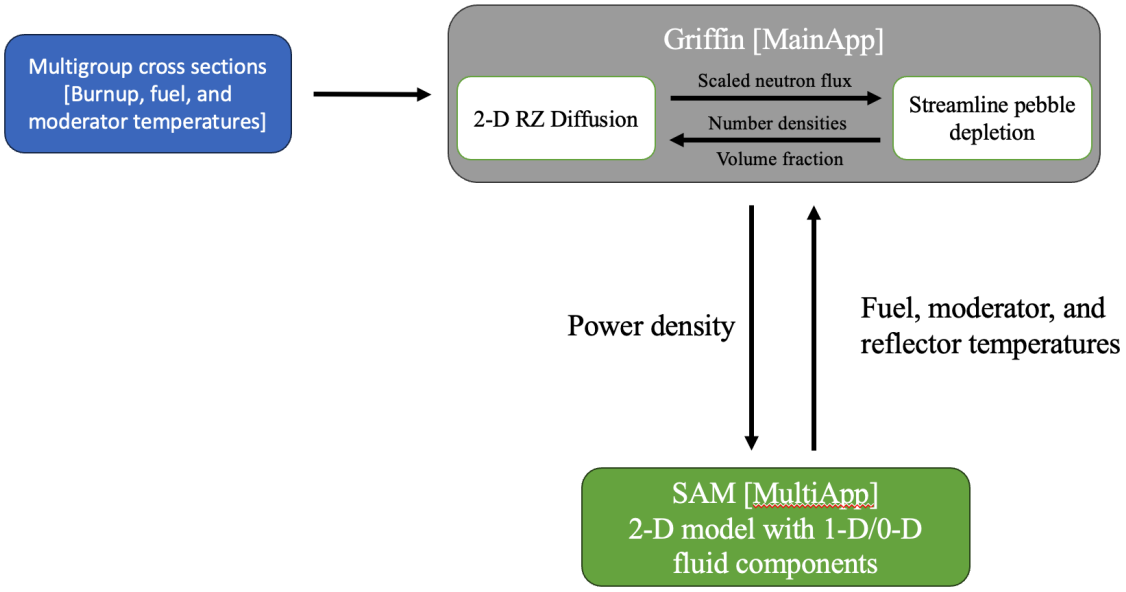

Figure 27. MultiApps coupling scheme of the SAM/Griffin multiphysics model for the PB-FHR.

2.5.2.2 Multiphysics Coupling with Pronghorn The general structure and variable transfers for the BlueCRAB model with Griffin spatial dynamics coupled to Pronghorn core fluids and SAM RCCS and SAM system loops are shown in Figure 28. In this work, Pronghorn was coupled to SAM on a case-by-case basis. Sometimes, Pronghorn was not coupled to SAM at all, sometimes to the SAM RCCS model only, and other times it included the RCCS, the rest of the salt primary loops, and secondary side via the overlapping domain coupling discussed in Section 2.5.1.3. In this BlueCRAB setup, Griffin is always the main application (MainApp) and solves the neutron diffusion equation in either the 3-D X-Y-Z or 2-D R-Z domains and the Bateman equation for each 1-D streamline defined. The Pronghorn MultiApp solves the porous medium equations for either the 3-D X-Y-Z or 2-D R-Z domain. The pebble/TRISO MultiApp model uses BISON and Pronghorn capabilities to solve for the fuel and graphite moderator temperature, as described in Section 2.3.2. The calculation flow is very similar to that discussed in Section 2.5.2.1. One distinction from the SAM approach to the fuel and moderator temperature calculation is the transfer of the partial power density and the burnup from Griffin, which generates a temperature solution for the pebble and TRISO in each of the pebble types and burnup groups. This is an important capability during the running-in phase of pebble-bed reactors, as well as for transient analysis. All MultiApps are coupled with a Picard iteration until convergence is achieved. Another difference is that the SAM RCCS is coupled to the Pronghorn application via boundary conditions in both the Pronghorn and SAM models, whereas the SAM single-solve approach internally couples the RCCS and core.

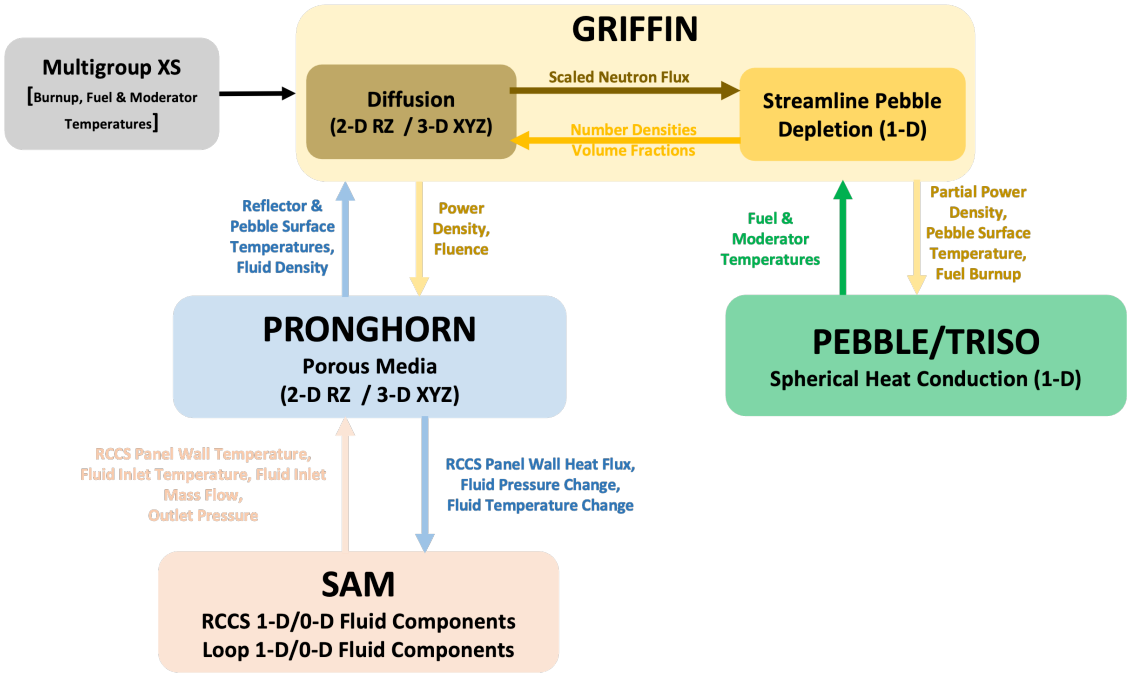

Figure 28. PB-FHR MultiApp coupling scheme for the Pronghorn/Griffin/SAM multiphysics model.

2.5.3. Griffin PKE and Thermal Fluids Coupling

Figure 29 shows the general structure and variable transfers for the BlueCRAB model with Griffin 0-D/PKE coupled to Pronghorn core fluids. It is noteworthy that the 0-D/PKE Griffin model and the Pronghorn model use a significant amount of information from the Griffin spatial dynamics steady-state calculations, including the PKE parameters as well as the spatial distributions for the power, volume fraction, and burnup of each pebble burnup group. The Griffin PKE model solves for the amplitude of the power based on global core values of the average fuel, moderator, and reflector temperatures, as well as coolant density. Griffin then transfers the power amplitude to the Pronghorn application. Subsequently, Pronghorn rescales the steady state partial power density distributions, determines the heat generation rate in the core, and solves the porous medium equations. Pronghorn transfers, for each pebble type and burnup group, the partial power density, pebble surface temperature and fuel burnup in each active core element to the BISON model which solves for the fuel and moderator temperatures. These values are transferred back to Pronghorn and constitute the various fields that are used in the averaging of core global fuel and moderator temperature feedback parameters.

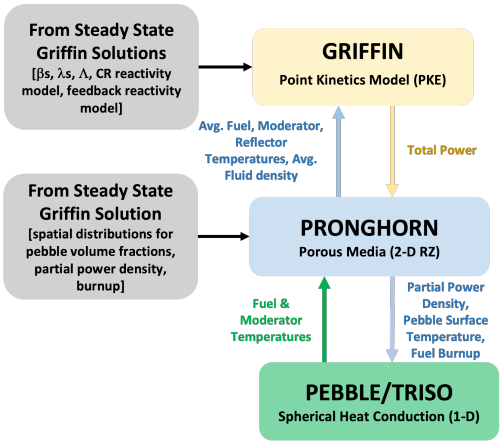

Figure 29. PB-FHR MultiApps coupling scheme for the Pronghorn/Griffin-PKE multiphysics model.

2.5.4. SAM PKE and Thermal Fluids Coupling

This section describes the modeling approach for SAM internal point kinetics coupled with SAM thermal fluids calculations. The point kinetics parameters applied in this SAM 0-D/PKE calculation were derived from 3-D Griffin simulations and are summarized in Tables 22, 23, and 24. The mean generation time, Λ, is 3.1773×10^{-4} seconds.

Several simplifications were adopted in the SAM 0-D/PKE model. First, this model only considers the total feedback coefficients for the fuel, moderator, reflector, and coolant, with the distributions of these coefficients being ignored. As a result, the volume-averaged fuel, moderator, reflector temperatures, and coolant density are used to calculate the reactivity feedback. Additionally, the local fuel and moderator temperatures are calculated based solely on the total local power density, with no distinctions being made between burnup groups. The 0-D/PKE model also assumes a constant power density distribution for steady-state and transient scenarios. For consistency, the solution from the SAM/Griffin/SAM coupled model is used to set the power density distribution for the SAM 0-D/PKE model. Furthermore, the same decay heat curve is applied in the SAM 0-D/PKE model as in the coupled SAM/Griffin/SAM calculation.

Table 22. Delayed neutron fractions and delayed neutron precursor decay constants.

Groups	β	λ[1/s]
1	0.000179	0.013336
2	0.001011	0.032739
3	0.000909	0.12078
4	0.002007	0.30278
5	0.000872	0.84949
6	0.000347	2.853

Table 23. Temperature reactivity feedback coefficients.

T [K]	Fuel [pcm/K]	Moderator [pcm/K]	Reflector [pcm/K]
650	-5.505	-0.495	0.308
750	-5.543	-0.507	0.311
850	-5.272	-0.747	0.315
950	-4.729	-0.969	0.207
1050	-4.429	-1.359	0.209
1150	-4.254	-1.396	0.210
1250	-3.694		
1350	-3.712		
1450	-3.730		
1550	-3.748		

Table 24. Coolant density reactivity feedback coefficients.

Coolant density [kg/m^3]	Reactivity feedback coefficient [pcm/(kg/m^3)]
1937.5	3.637
1975	3.524
2025	3.346
2075	3.205
2110.1	3.133

3. ANALYSIS AND RESULTS

Section 3.1 covers the results and analysis for the steady-state cases, including equilibrium core results, comparisons of various thermal fluid solvers and couplings, and solutions from the coupled Pronghorn/Griffin and SAM/Griffin models. Section 3.2 presents the results from the protected LOFC scenario, while Section 3.3 addresses the unprotected LOFC scenario. Section 3.4 introduces the results for the baseline 2-D control rod movement accident scenario. Lastly, Section 3.5 analyzes and compares the 3-D, 2-D, and 0-D/PKE results.

3.1. Steady State

The various models developed in this work produced similar solutions for the equilibrium core, with differences arising from the discretization used and the core regions included in the analysis. Therefore, not all models will be analyzed in depth. Instead, the equilibrium core results from the 2-D and 3-D control rod withdrawal models are discussed in detail in 3.1.1. In these models, it was necessary to drive all the rods deeper into the core to achieve the target reactivity range when one or two rods were removed. Initially, we performed the coupled equilibrium core calculation, followed by a subsequent coupled k-eigenvalue calculation with all rods banked at 2.21 m. The basic isotopic concentrations are essentially the same, with differences observed in the fission product poison concentrations. The initial conditions for the various transient scenarios are discussed in 3.1.5, 3.1.6, and 3.1.7.

Sections 3.1.2 and 3.1.3 compare the 2-D porous media models of Pronghorn and SAM. These sections present standalone thermal fluids simulation results for the core, as well as results for the coupled Pronghorn/Griffin and SAM/Griffin core models. In both sections, the same closure correlations and boundary conditions are applied to the SAM and Pronghorn models. Additionally, Section 3.1.4 compares the steady-state results between two multiscale thermal fluid coupling schemes used to couple the SAM 2-D porous media core and 1-D system models.

3.1.1. Equilibrium Core

The fundamental mode eigenvalue (k_{eff}) and discharge burnup from Griffin for the 2-D and 3-D equilibrium core calculations are reported in Table 25. The average and maximum power densities from the two models, as well as the local power peaking values, align closely with each other. The maximum power is determined for each pebble burnup group, with the first burnup group primarily driving this value, due to it having the highest concentration of ^{235}U. The core pebble power peak is computed from the pebble maximum and the core-averaged pebble power density. There is a 5 degree difference between the pebble surface average temperatures predicted by the 2-D and 3-D models. This discrepancy originates from the fluid solution and affects the temperatures of the pebble surface, fuel, moderator, and reflector. The coolant densities, along with the various fission product concentrations, are consistent in both models. Thermal fluid data comparisons are presented in Table 26. The calculated flow distribution between the inlet annulus, fueling chute, and control rod channel is 76.4%, 14.5%, and 9.1%, respectively. Additionally, a 5 K difference in core-averaged fluid temperature is observed.

The flux distributions are illustrated in Figure 30. The flux shape is bottom-peaked because the pebbles at the bottom have a lower burnup, and the FLiBe density is at its highest in the pebble-bed region. The flux shapes in the first three groups are similar. Neutron moderation peaks are noticeable near the graphite reflectors in the fourth flux group. The flux solutions from the 3-D and 2-D models are consistent.

The spatial distributions of the ^{235}U, ^{238}U, and ^{239}Pu isotopes are shown in Figure 31. The ^{235}U distribution has the highest concentration at the bottom of the core, where fresh pebbles are fed into the fueling chute, and gradually decreases in concentration as it approaches the defueling chute. The higher porosity near the wall is also evident. A similar behavior is observed for ^{238}U as it depletes and produces

Table 25. Comparison of 2-D and 3-D equilibrium core neutronics.

Parameter	3-D	2-D	% or pcm
k_{eff}	1.00888	1.00889	1.00
Discharge burnup [EFPD]	471.32	471.32	0.00
Total core power [MWth]	320.0	320.0	0.00
Pebble power density avg [W/cm^3]	26.61	26.61	0.00
Pebble power density max [W/cm^3]	69.75	69.32	-0.61
Local pebble power peak	1.289	1.286	-0.16
Core pebble power peak	2.62	2.60	-0.76
CR position [m]	4.225	4.225	0.00
Pebble surface avg. temp. [K]	923.55	928.18	0.50
Fuel avg. temp. [K]	969.98	974.74	0.49
Fuel max. temp. [K]	1066.6	1071.1	0.42
Mod avg. temp. [K]	941.18	945.86	0.50
Mod max. temp. [K]	1011.5	1014.2	0.26
Reflector avg. temperature [K]	909.39	915.57	0.68
Coolant density avg. [kg/m^3]	1976.5	1974.6	-0.10
Coolant density max. [kg/m^3]	2010.9	2010.9	-0.00
^{135}Xe avg. conc. [at/b-cm]	3.0535e-10	3.0576e-10	0.13
^{135}Xe max. conc. [at/b-cm]	4.0099e-10	4.0225e-10	0.31
^{149}Sm avg. conc. [at/b-cm]	3.0723e-09	3.0832e-09	0.36
^{149}Sm max. conc. [at/b-cm]	4.1437e-09	4.1662e-09	0.54
^{135}I avg. conc. [at/b-cm]	1.0827e-09	1.0822e-09	-0.05
^{149}Pm avg. conc. [at/b-cm]	2.0630e-09	2.0616e-09	-0.07

Table 26. Comparison of 2-D and 3-D equilibrium core thermal fluids.

Parameter	3-D	2-D	%
Total mass flow [kg/s]	1318.69	1318.69	0.00
Inlet annulus mass flow [kg/s]	1011.64	1011.64	-0.00
Fueling chute mass flow [kg/s]	192.70	192.70	-0.00
Fueling chute fluid temp. [K]	833.66	833.74	0.01
Lower cone fluid temp. [K]	839.23	839.84	0.07
Core avg. fluid temp. [K]	893.84	897.72	0.43
Cyl. core avg. fluid temp. [K]	892.42	896.29	0.43
Upper cone fluid temp. [K]	939.36	945.52	0.66
Defueling chute fluid temp. [K]	952.00	960.25	0.87
Defueling chute pressure [Pa]	1.00E+05	1.00E+05	0.00
Defueling chute temp. [K]	952.25	960.49	0.86
Defueling chute velocity [m/s]	0.16	0.16	-1.29
Defueling chute mass flow [kg/s]	61.78	60.86	-1.50
Outlet annulus pressure [Pa]	1.00E+05	1.00E+05	0.00
Outlet annulus temp. [K]	922.24	921.86	-0.04
Outlet annulus velocity [m/s]	0.19	0.19	0.07
Outlet annulus mass flow [kg/s]	1256.91	1257.83	0.07
Outlet annulus velocity [m/s]	0.43	0.43	0.07
Reflector center top temp. [K]	952.12	959.94	0.82
Reflector side temp. [K]	907.39	913.50	0.67
Barrel temp. [K]	907.19	913.41	0.69

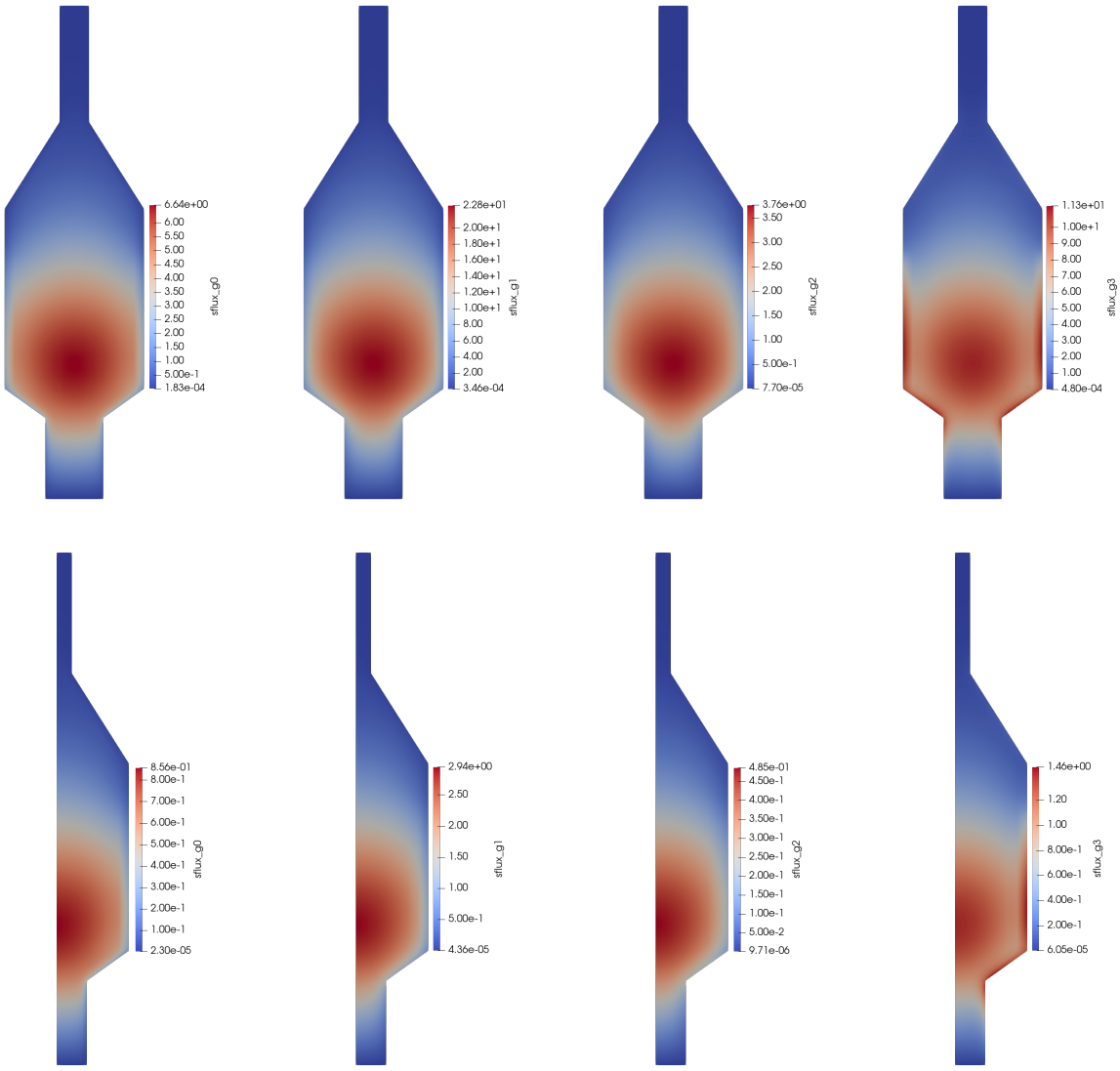

Figure 30. Equilibrium core normalized flux distributions for the 3-D and 2-D models.

^{239}Pu, but with smaller-magnitude changes. Conversely, the concentration of ^{239}Pu increases as the pebbles travel through the core, especially near the core center where the hardest spectrum is located. The model indicates that ^{239}Pu located near the reflector walls is more effectively burned as it travels through the core.

The spatial distributions of the ^{135}Xe, ^{90}Sr, and ^{137}Cs isotopes are illustrated in Figure 32. ^{135}Xe is significant for long transients such as the unprotected loss-of-flow condition (LOFC), where changes in ^{135}Xe concentration combined with core temperature variations create conditions for recriticality. ^{90}Sr and ^{137}Cs are fission products of particular interest in regard to dose calculations, and their distributions follow the burnup distribution of the core.The spatial distributions of the pebble-averaged power density, maximum power density, and local power peaking are depicted in Figure 33. The power distribution aligns with the thermal flux distribution in the pebble bed, with peak power occurring near the bottom center of the core. The highest local peaking value, for each pebble type and burnup group, is found near the reflector in the upper portion of the pebble bed. This is due to the higher burnup in this region and the larger discrepancy between the average and maximum power levels.

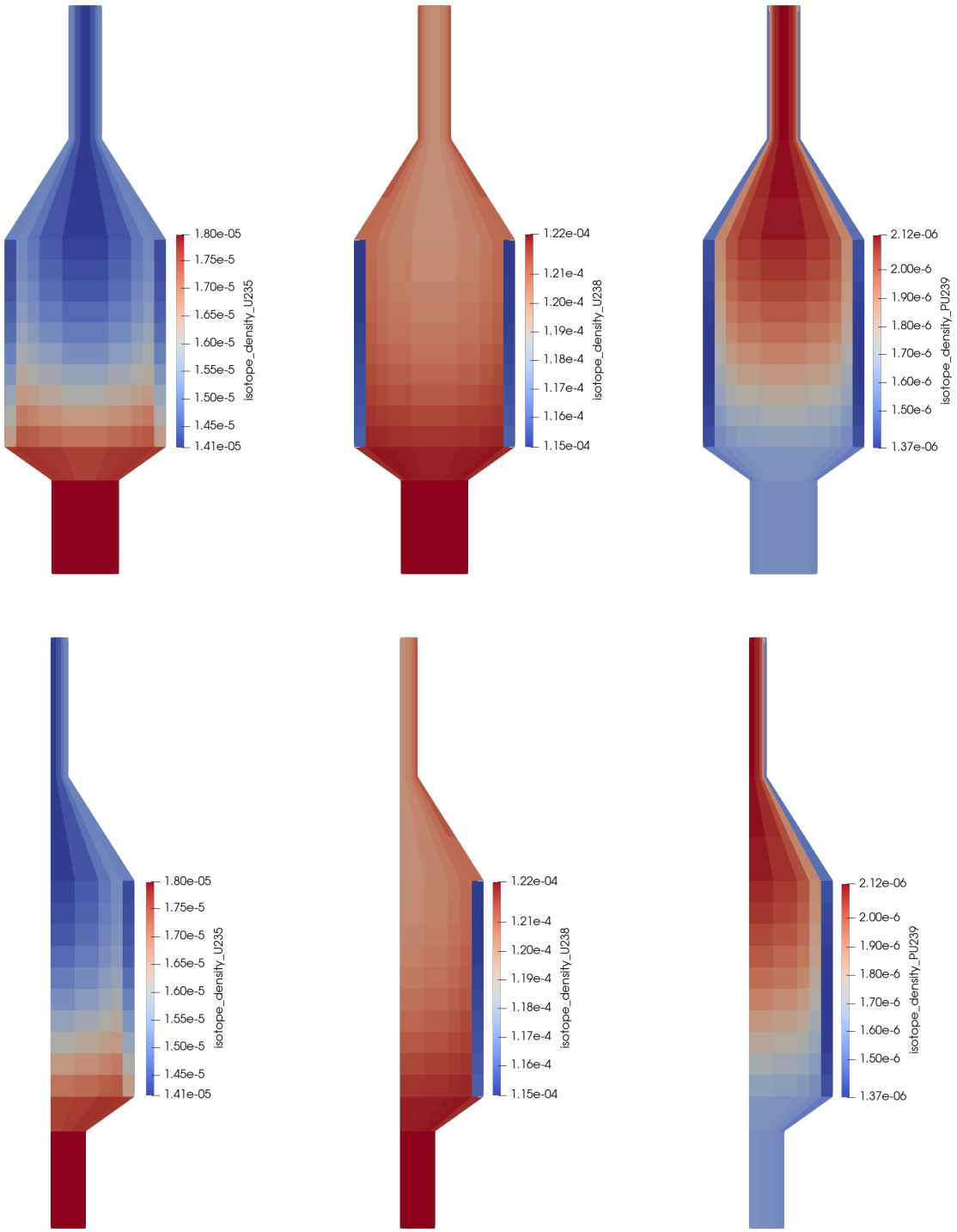

Figure 31. Equilibrium core pebble-averaged ^{235}U, ^{238}U, and ^{239}Pu distributions for the 3-D and 2-D models.

One notable feature of the Griffin code is its ability to deplete pebbles based on a burnup group structure. In the depletion calculation, Griffin computes the volume fraction in each burnup group for each spatial zone

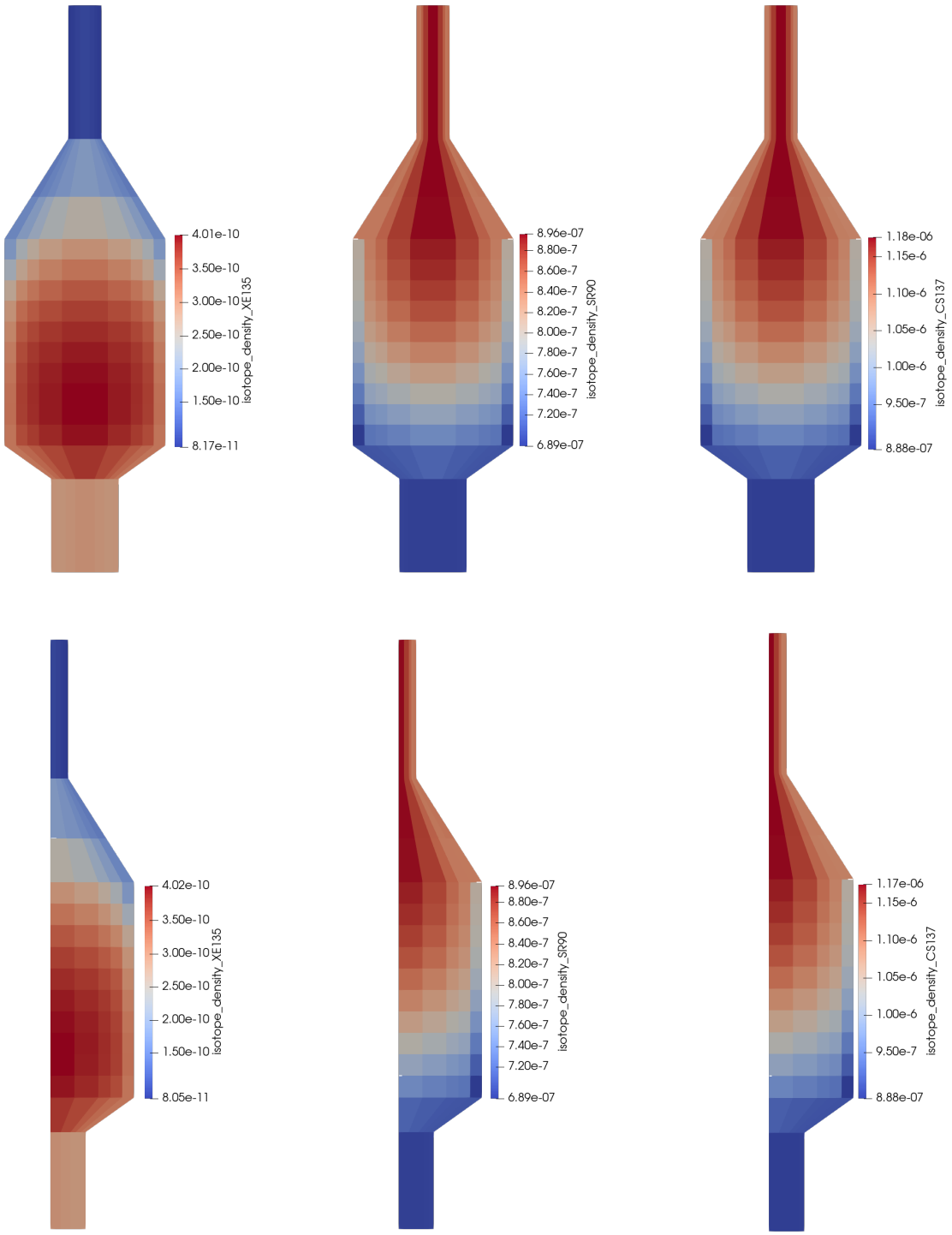

Figure 32. Equilibrium core pebble-averaged ^{135}Xe, ^{90}Sr, and ^{137}Cs distributions for the 3-D and 2-D models.

in the core, as shown in Figure 34. The lowest burnup group (0 in Griffin), which comprises the least burned pebbles, experiences a significant change in volume fraction as pebbles transition to other burnup groups

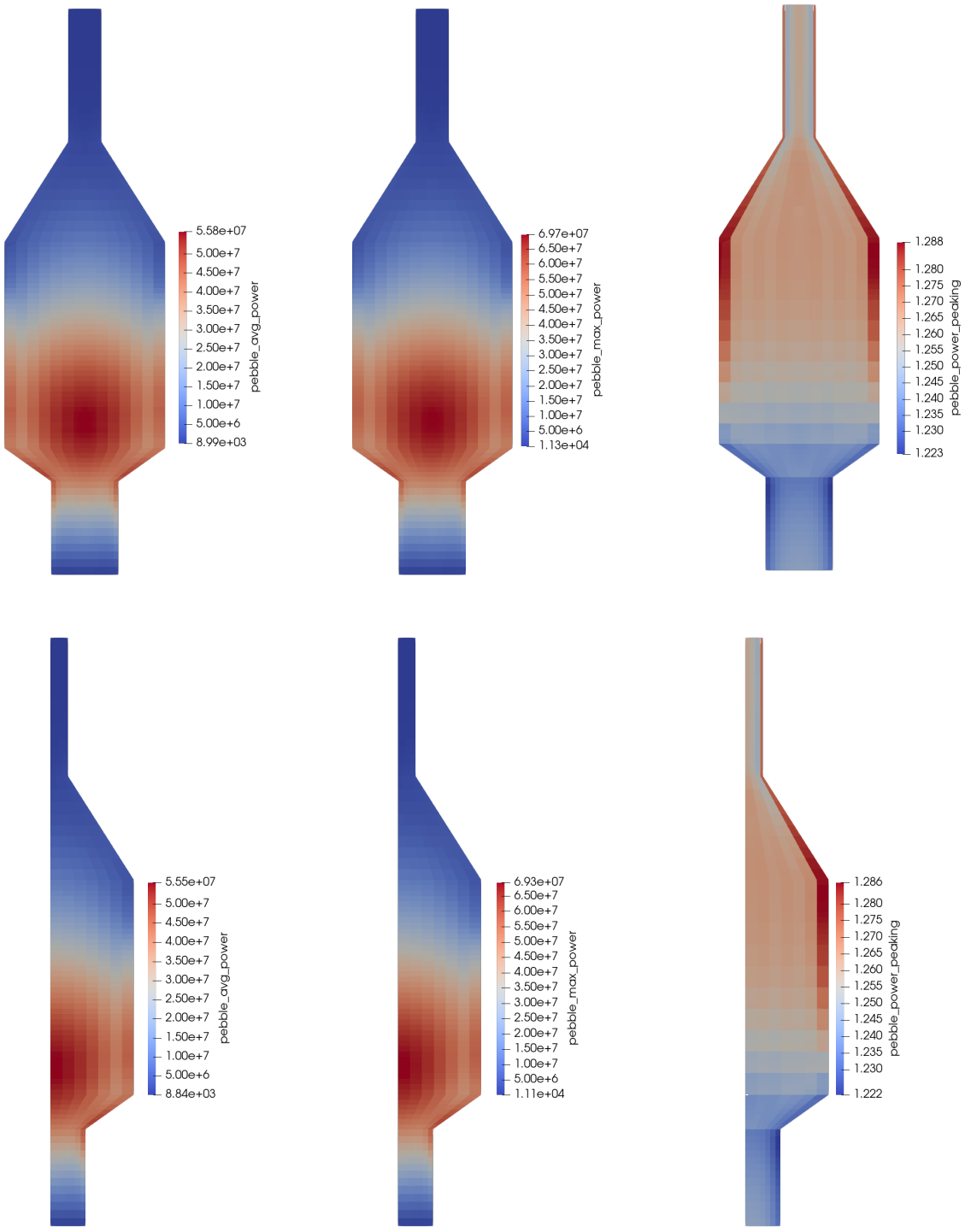

Figure 33. Equilibrium core pebble-averaged and maximum pebble power density distributions and local pebble power peaking for the 3-D and 2-D models.

while moving through the core. The volume fraction for this group changes from 0.026 to 0.116. The next group (1 in Griffin) experiences less of a gradient, as the rate of depletion decreases in each subsequent group.

For burnup group 2, the range is from 0.052 to 0.071. In burnup group 6 (5 in Griffin), the volume fraction remains nearly constant, representing an extreme case in which there is a balance between the inflow and outflow from this burnup group throughout the core. Finally, the last group (8 in Griffin) shows a significant change as pebbles are discarded upon reaching their burnup limit, starting with a low concentration of 0.003 at the bottom of the core and increasing to 0.107 at the top of the core.

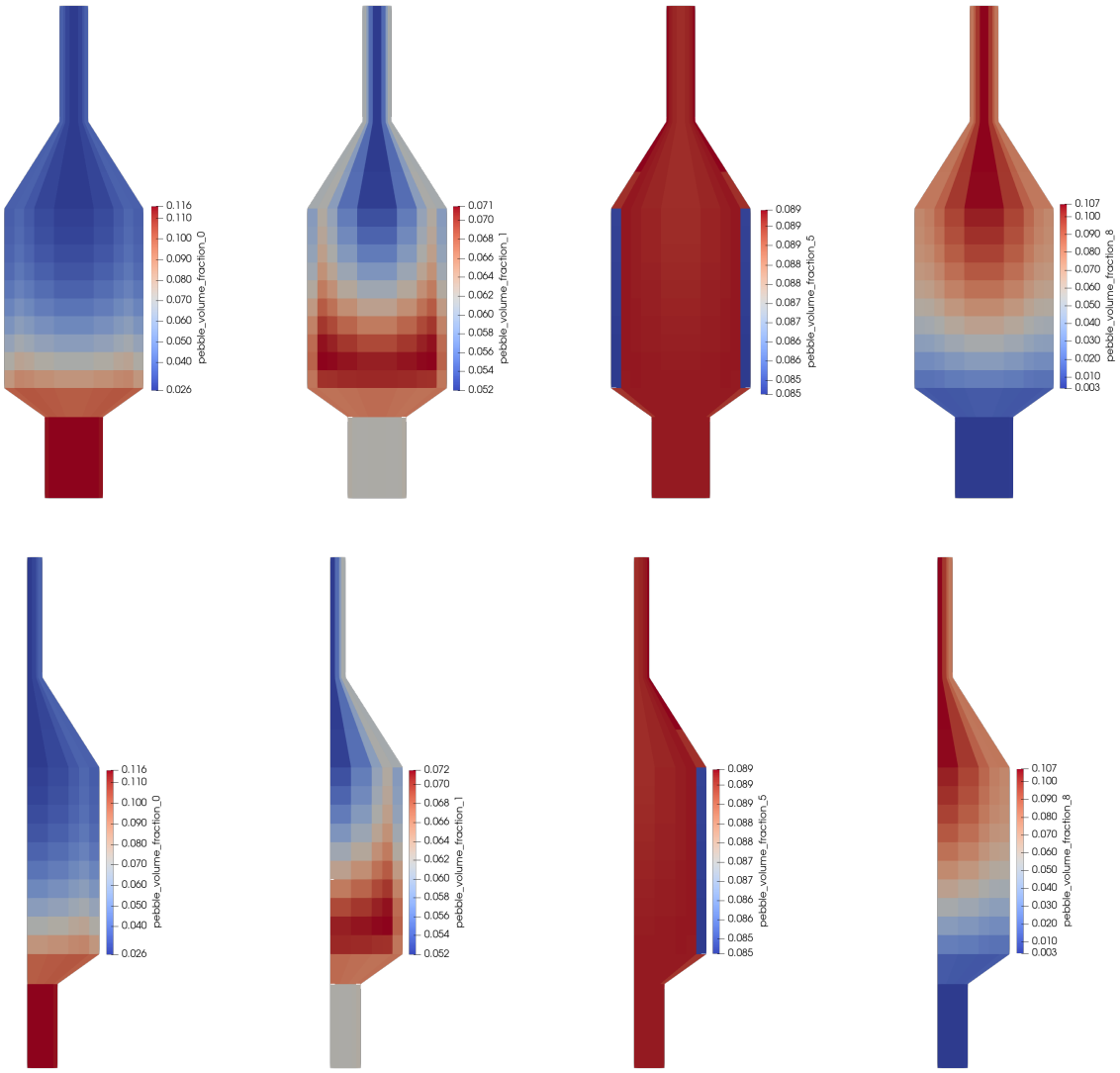

Figure 34. Equilibrium core pebble burnup group volume fractions for 3-D and 2-D models. % FIMA for Group 0 = 1.17, Group 1 = 3.50, Group 5 = 12.83, and Group 8 = 16.98.

The spatial distribution of the fuel and moderator temperatures is shown in Figure 35. These include the average and maximum pebble temperatures, which are the average values from each pebble burnup group in each finite element. The results indicate a high-temperature region at the bottom center of the core, where the power distribution is at its maximum, and a peak at the center top, where flow recirculation appears to lead to higher pebble surface temperatures. The flow recirculation area, influenced by the cone and the high flow resistance from the pebbles, can be observed in Figure 37. Near the top cone are regions of flow recirculation around the point where the flow splits between the annulus and defueling chute. This flow split

and subsequent flow area contraction might cause a local recirculation within the cone. This region is present in both the 2-D and 3-D models. This result requires further inquiry since it could be an artifact of the solver.

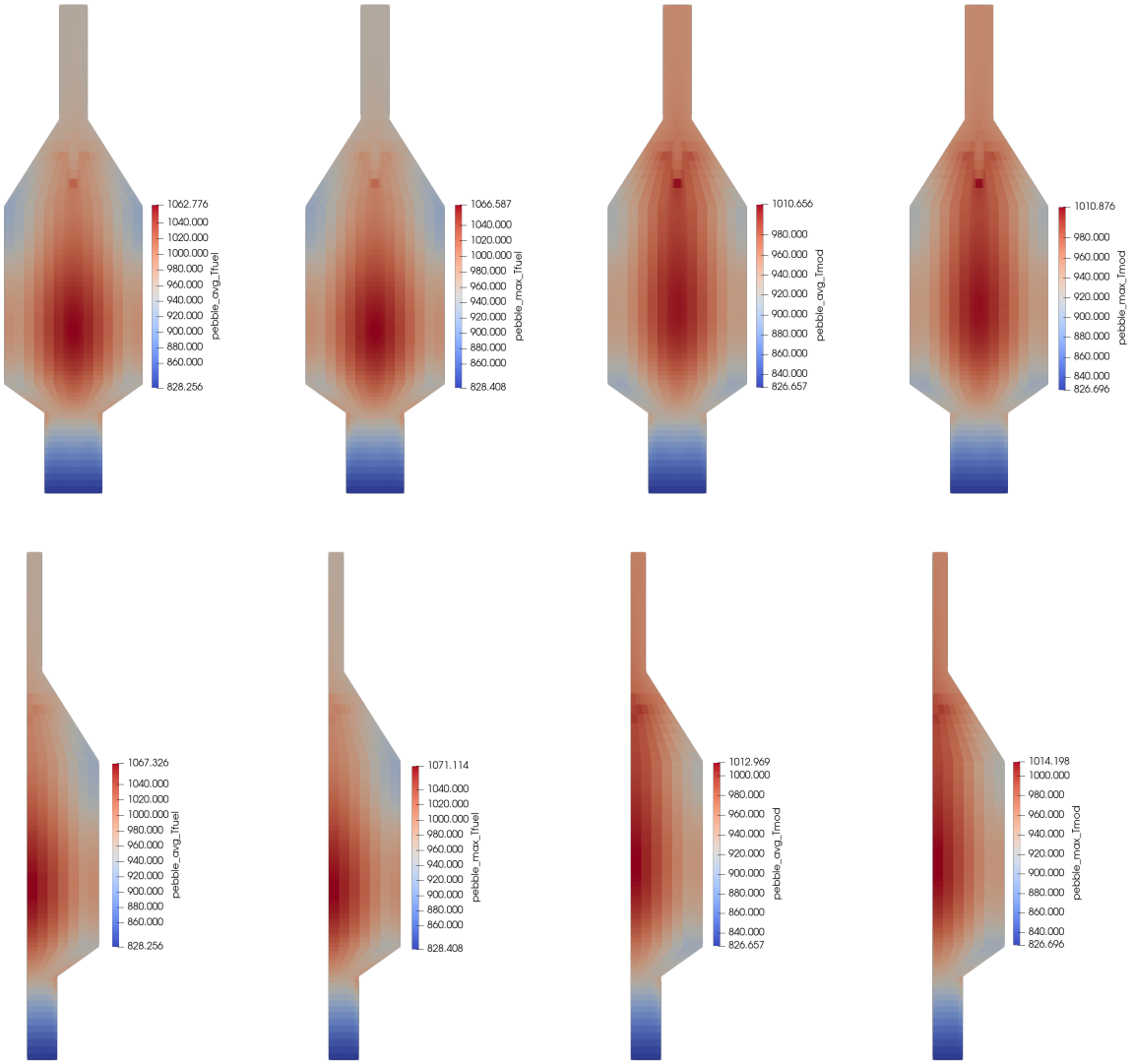

Figure 35. Equilibrium core pebble-averaged fuel and moderator temperature distributions [K] for the 3-D and 2-D models.

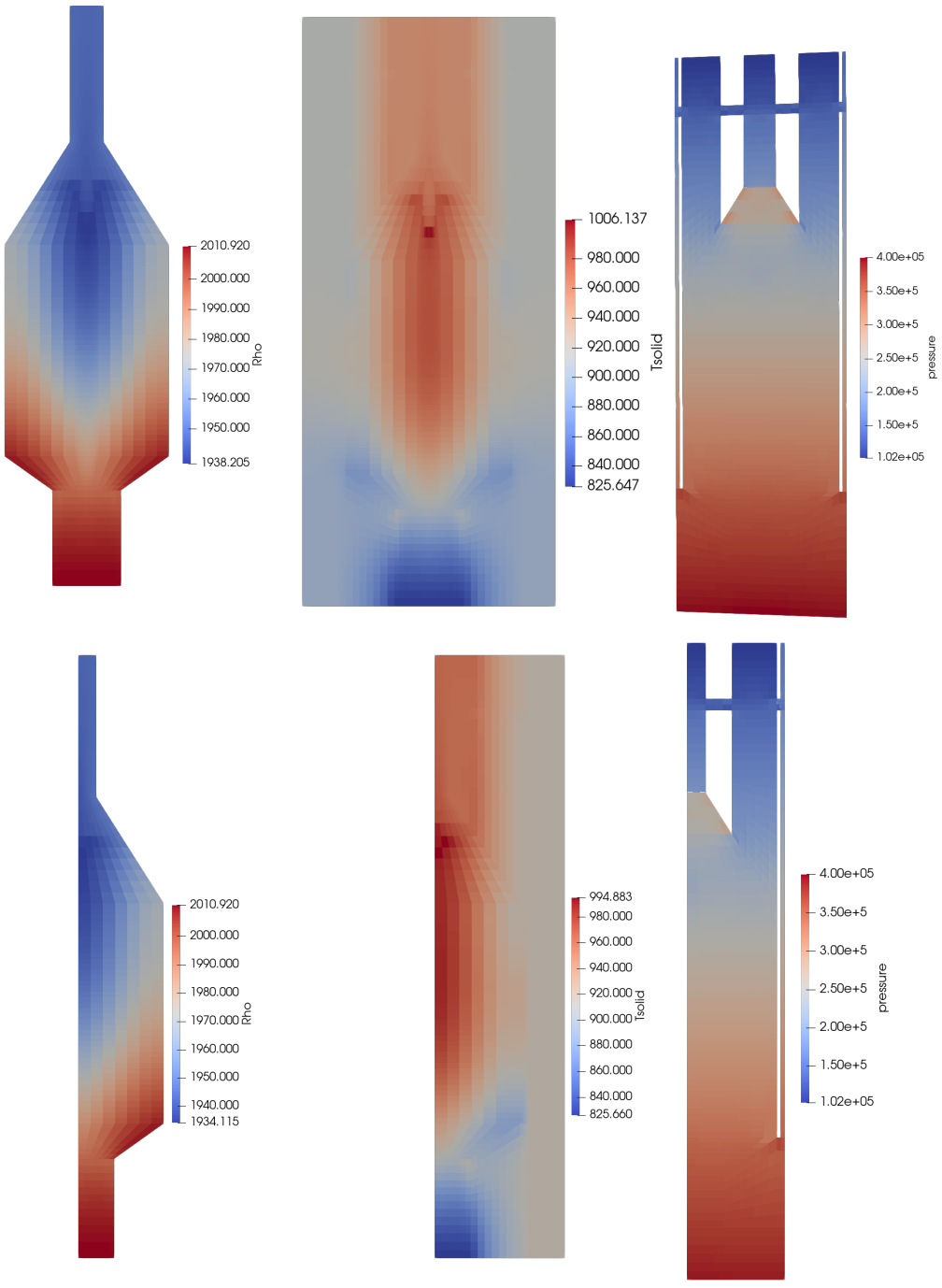

Figure 36. Equilibrium core coolant density [kg/m^3], solid temperature [K], and pressure [Pa] distributions.

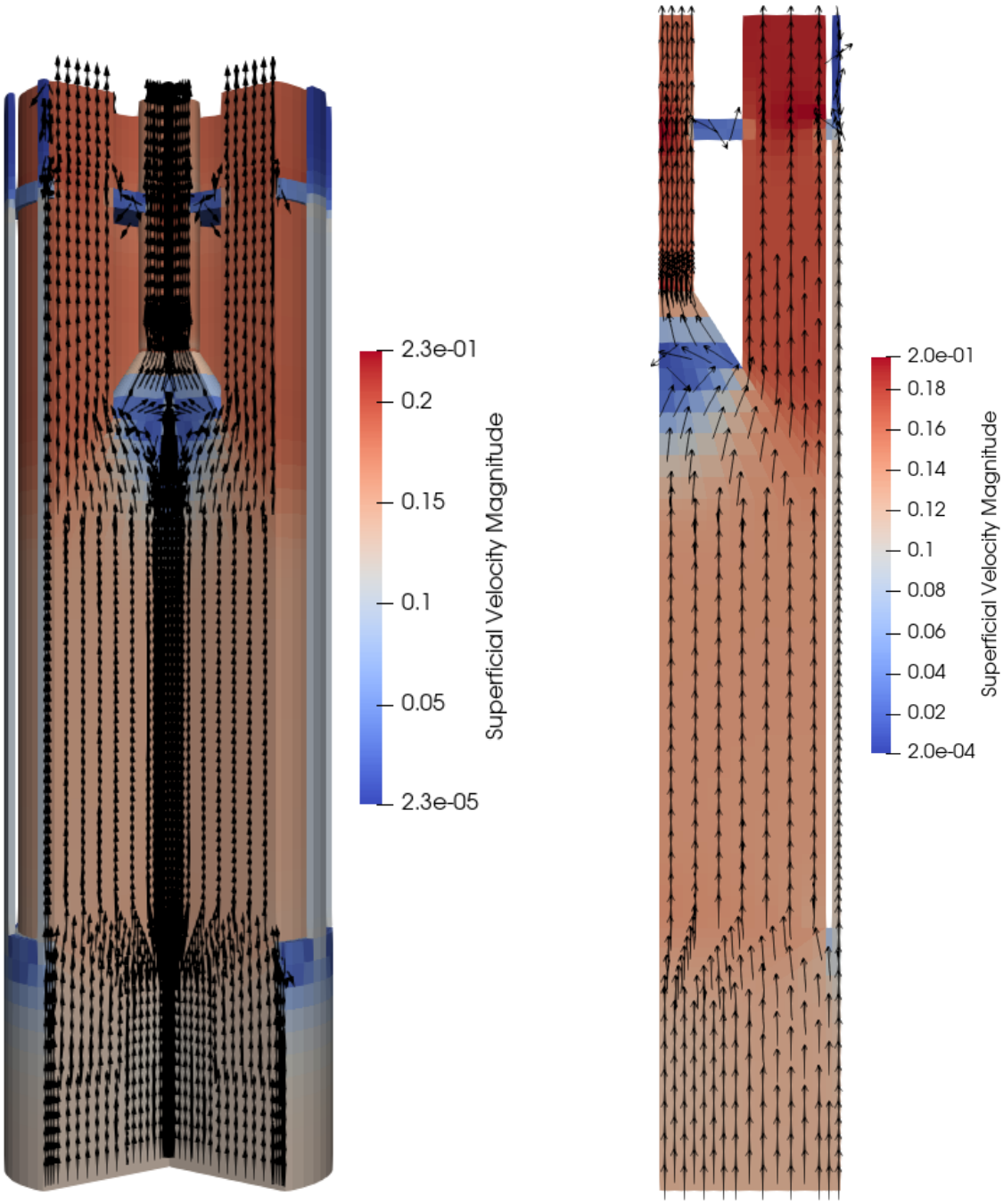

Figure 37. Equilibrium core flow path for the 2-D and 3-D Pronghorn/Griffin models.

The point kinetics model requires approximations for the PKE parameters. The values calculated from the Griffin 3-D model are presented in Table 27, with the control rods being positioned at the equilibrium core configuration (4.225 m) and deeply inserted (2.21 m). We chose the values at 2.21 m, since they are the starting point of the spatial transient solutions. There is little difference between the delayed neutron fractions. The main difference lies in the mean generation time, as the control rod position affects the fraction of neutrons returning to the core, thus giving more weight to neutrons within the core.

As discussed in Section 2.2.5, the Griffin 0-D/PKE reactivity model in this work is based on a linear combination of independent components. The control rod reactivity component is based on the 3-D integral worth when either one or two control rods are removed. The reactivity curves for single and double control rod movements in the 3-D and 2-D simulations are shown in Figure 38. These curves only include fuel and graphite moderator feedback and assume that the coolant feedback will be delayed. There are significant differences in the 2-D model differential worths that cannot be resolved without deploying equivalence theory. This task is left for future work, but it highlights one of the weaknesses of the 2-D Griffin model.

Table 27. Griffin 0-D/PKE parameters computed from 3-D calculations.

Delayed Group	β CR at 4.225 m	β CR at 2.21 m	λ [1/s]
1	1.7908×10^{-4}	1.7993×10^{-4}	1.3336×10^{-2}
2	1.0099×10^{-3}	1.0122×10^{-3}	3.2739×10^{-2}
3	9.0714×10^{-4}	9.1058×10^{-4}	1.2078×10^{-1}
4	2.0036×10^{-3}	2.0108×10^{-3}	3.0278×10^{-1}
5	8.7075×10^{-4}	8.7340×10^{-4}	8.4949×10^{-1}
6	3.4651×10^{-4}	3.4786×10^{-4}	2.8530
β_{eff} [pcm]	531.69	533.48	–
Λ [s]	3.1742×10^{-4}	2.7406×10^{-4}	

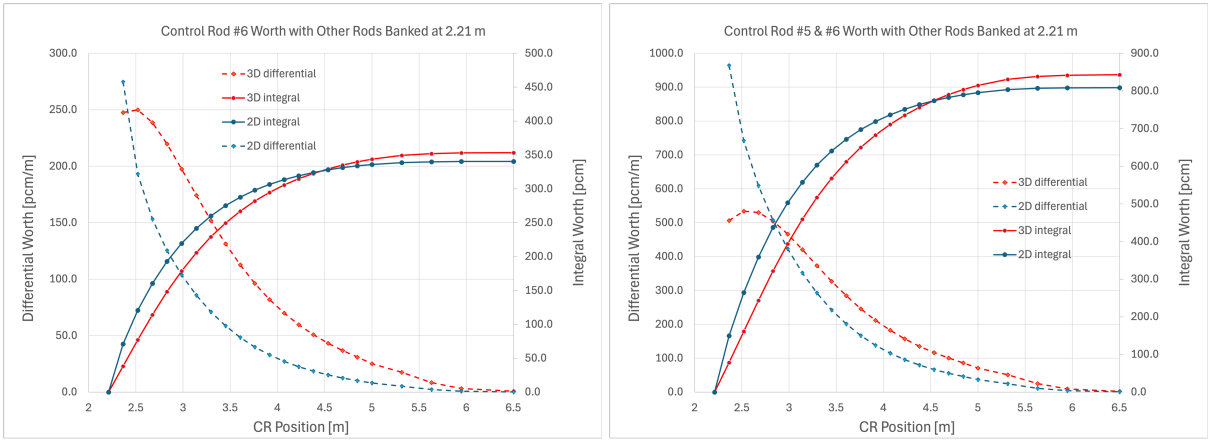

Figure 38. Control rod worth for 1 and 2 control rods in the 3-D and 2-D models. The remaining control rods are banked at 2.21 m.

One of the challenges encountered in this work is the calculation of the reactivity model for the 0-D/PKE simulations. This issue could stem from various factors, with the leading theory suggesting that the linear combination model is inadequate for this application. Consequently, we recommend transitioning to a fully correlated reactivity surrogate model in the future, for transient cases where PKE can be deployed.

Tables 28 and 29 present a series of static and dynamic reactivity calculations. The static calculations were performed with and without feedback, while the dynamic calculation used the Improved Quasi-Static (IQS) method in Griffin to predict the reactivity. The dynamic reactivity value was confirmed via an exponential fit to the reactor power curve after the rod was fully ejected, without feedback, thus producing a stable reactor period, which was then converted to a reactivity value by solving the Inhour equation (inverse kinetics). The predicted rod worth for both one and two rods increased with feedback to 0.71$ and 1.67$, respectively. The static and dynamic rod worth results without feedback are consistent at 0.64$ and 1.5$, respectively. The adjusted value reported was obtained through manual iteration to better match the spatial dynamics solutions. These results indicate inconsistencies in the reactivity model, necessitating adjustments to the PKE control rod reactivity to achieve similar results to those obtained with the spatial dynamics models. For the PKE control rod reactivity models, we used the shape from the 3-D integral worth curve and re-normalized it to the dynamic (without feedback) and adjusted values, which we later report in the two PKE solutions.

Table 28. Reactivity calculation for the single control rod withdrawal.

	$k_{eff,in}$	$k_{eff,out}$	reactivity	reactivity [$]
Static with feedback	0.97313	0.97681	0.00377	0.707
Static without feedback	0.97313	0.97648	0.00343	0.643
Dynamic without feedback	–	–	0.00341	0.638
Adjusted	–	–	0.00276	0.517

Table 29. Reactivity calculation for the double control rod withdrawal.

	$k_{eff,in}$	$k_{eff,out}$	Reactivity	Reactivity [$]
Static with feedback	0.97313	0.98185	0.00889	1.666
Static without feedback	0.97313	0.98124	0.00827	1.550
Dynamic without feedback	–	–	0.00809	1.517
Adjusted	–	–	0.00650	1.218

The temperature reactivity coefficients computed using the Griffin 3-D simulation are shown in Table 30, and the coolant density reactivity coefficients are presented in Table 31. These values differ slightly from the SAM model values, due to a late update to the 3-D model that slightly modified the results. These updated values are reported here for the sake of completeness. It is important to emphasize that these coefficients were computed using a constant distribution for the variable. In the future, we can assess the impact of using a steady-state distribution in these calculations.

The Griffin 0-D/PKE model relies on 2-D steady-state Griffin and Pronghorn initial conditions, from which we compute the independent scalar variables (T_{fuel}, T_{mod}, T_{ref}, D_{cool}) that represent the core average conditions. Any deviation from those initial values causes a change in the 0-D/PKE reactivity model. The values in Tables 30 and 31 were reformulated to ensure that the coupled model can hold a null transient. The reactivity parametrization of all reactivity components is shown in Table 32. Note that the values for the 0 reactivity point have many more digits than shown in the Table 32. Nevertheless, this illustrates how a simple PKE reactivity model can be input in Griffin.

Table 30. Temperature reactivity feedback coefficients.

T $[K]$	Fuel $[pcm/K]$	Moderator $[pcm/K]$	Reflector $[pcm/K]$
650	-5.510	-0.488	0.307
750	-5.548	-0.499	0.310
850	-5.278	-0.741	0.313
950	-4.735	-0.965	0.206
1050	-4.435	-1.359	0.208
1150	-4.260	-1.395	0.209
1250	-3.701		
1350	-3.719		
1450	-3.737		
1550	-3.755		

Table 31. Coolant density reactivity feedback coefficients.

Coolant density $[kg/m^3]$	Reactivity feedback coefficient $[pcm/(kg/m^3)]$
1937.5	3.639
1975	3.525
2025	3.344
2075	3.201
2110.1	3.128

Table 32. Griffin 0-D/PKE reactivity feedback model.

T_{fuel} $[K]$	ρ_{Fuel}	T_{mod} $[K]$	ρ_{mod}	T_{ref} $[K]$	ρ_{ref}	D_{cool} $[\frac{kg}{m^3}]$	ρ_{cool}
600	2.032E-02	600	2.246E-03	600	-9.23E-04	1925	-1.70E-03
700	1.476E-02	700	1.754E-03	700	-6.13E-04	1950	-7.77E-04
800	9.162E-03	800	1.249E-03	800	-3.00E-04	1971.80	0.00E+00
900	3.834E-03	900	5.006E-04	894.93	0.00E+00	2000	1.00E-03
980.28	0.000E+00	951.38	0.000E+00	900	1.60E-05	2050	2.69E-03
1000	-9.460E-04	1000	-4.742E-04	1000	2.24E-04	2100	4.31E-03
1100	-5.423E-03	1100	-1.847E-03	1100	4.34E-04	2120	4.95E-03
1200	-9.723E-03	1200	-3.256E-03	1200	6.45E-04		
1300	-1.346E-02						
1400	-1.721E-02						
1500	-2.099E-02						
1600	-2.478E-02						

3.1.2. Steady-State Comparison Between the SAM and Pronghorn 2-D Porous Media Models

This section compares the 2-D SAM and Pronghorn porous media standalone simulation results for the core. The primary, secondary, and RCCS loop models are excluded from both calculations in this comparison. Instead, core inlet velocity, inlet temperature, and outlet pressure are given as boundary conditions. An adiabatic boundary condition is applied to the outer surface of the vessel wall in both the SAM and Pronghorn models. To ensure a consistent basis for comparison, the same 2-D mesh is employed in both simulations, as shown in Figure 13. Identical power density distributions, as illustrated in Figure 39, are directly applied as an input to both the SAM and Pronghorn calculations. Table 33 summarizes the correlations in the SAM and Pronghorn 2-D core porous media calculations. Specifically, the Cheng model [49] was applied to estimate the core porosity distribution in the near wall region of the pebble-bed cylindrical core. The pebble-bed heat transfer coefficient and pebble-bed wall heat transfer coefficient are calculated using Wakao correlations [50, 51]. The ZBS [52] model and KTA model [53] were utilized for the pebble-bed effective thermal conductivity and pebble-bed friction model, respectively.

With these consistent modeling assumptions and boundary conditions, the results from SAM and Pronghorn show close agreement. Table 34 compares the core inlet and outlet results. The average core outlet temperatures differ by only 0.1 K: 922.7 K in SAM and 922.8 K in Pronghorn. The flow split at the core outlet between the defueling chute and outlet annulus is 3.6% and 96.4% in SAM, as compared to 3.8% and 96.2% in Pronghorn. The pressure drops across the core are 0.248 and 0.242 MPa in SAM and Pronghorn, respectively. Figures 40, 41, and 42 compare the solid temperature, fluid temperature, and axial velocity distributions. These spatial distribution results for SAM and Pronghorn are all in good agreement with each other.

Table 33. Summary of heat transfer coefficient and frictional pressure drop correlations in the standalone SAM and Pronghorn 2-D core porous media calculations.

Parameter	SAM/Pronghorn
Core porosity distribution	Cheng model
Pebble bed HTC	Wakao
Pebble bed Wall HTC	Wakao
Pebble bed effective thermal conductivity	ZBS
Pebble bed friction	KTA

Table 34. Comparison of the SAM and Pronghorn 2-D core porous media standalone simulations.

Parameter	SAM	Pronghorn
Mass flow rate [kg/s]	1324.7	1324.4
Coolant inlet temp. [K]	823.15	823.15
Coolant outlet temp. [K]	922.7	922.8
Flow split in defueling chute [%]	3.6	3.8
Flow split in outlet annulus [%]	96.4	96.2
Pressure drop from core inlet to hotwell inlet [MPa]	0.248	0.242

Figure 43 presents the axial fluid temperature profiles at two radial positions: r = 0.15 m and r = 0.92 m. The results from SAM and Pronghorn show good agreement with each other at both locations. At r = 0.15 m, the fluid temperature begins to rise from the core inlet. Upon entering the defueling chute, the temperature

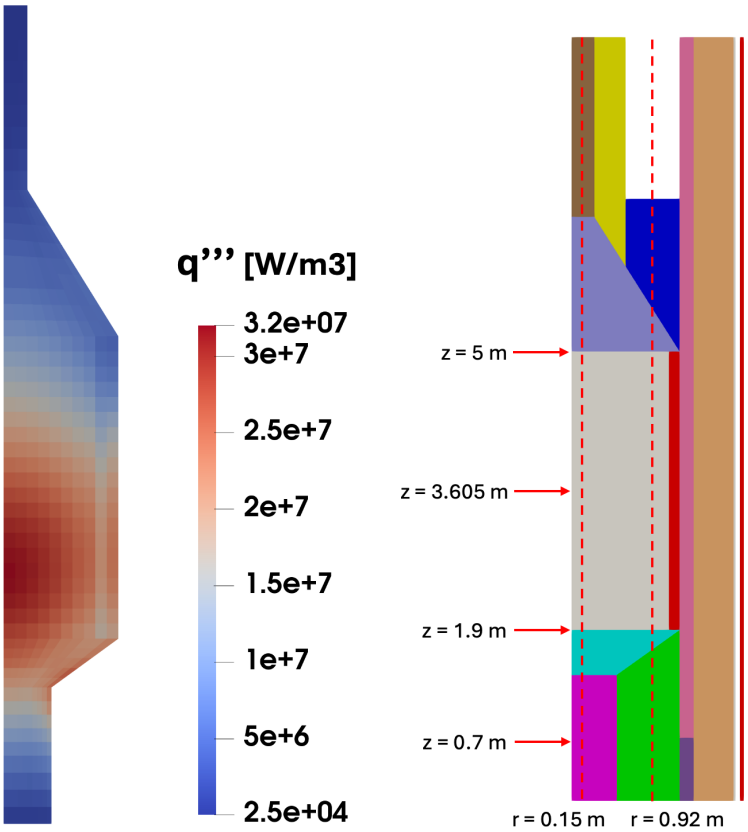

(a) Power density (b) Axial and radial locations

Figure 39. Power density distribution and locations of axial and radial profiles for comparing the Pronghorn and SAM 2-D core porous media.

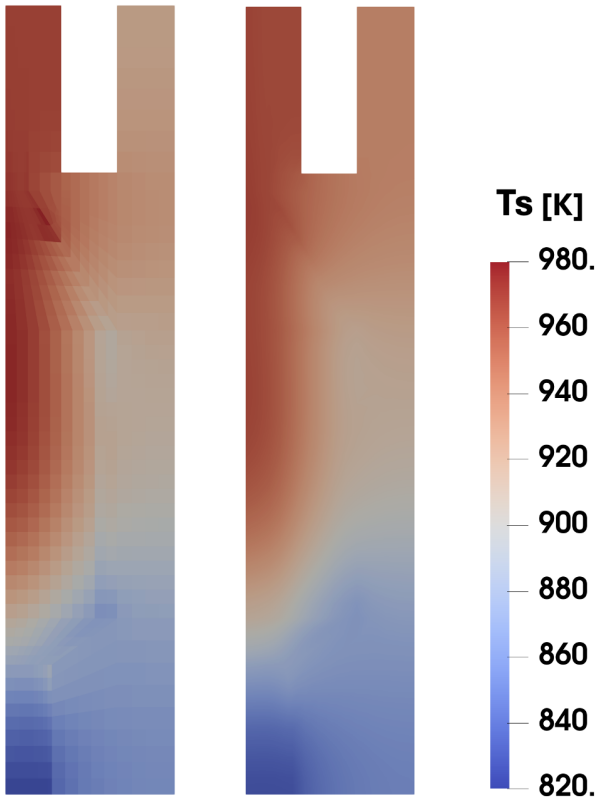

Figure 40. Solid temperature distributions from Pronghorn (left) and SAM (right).

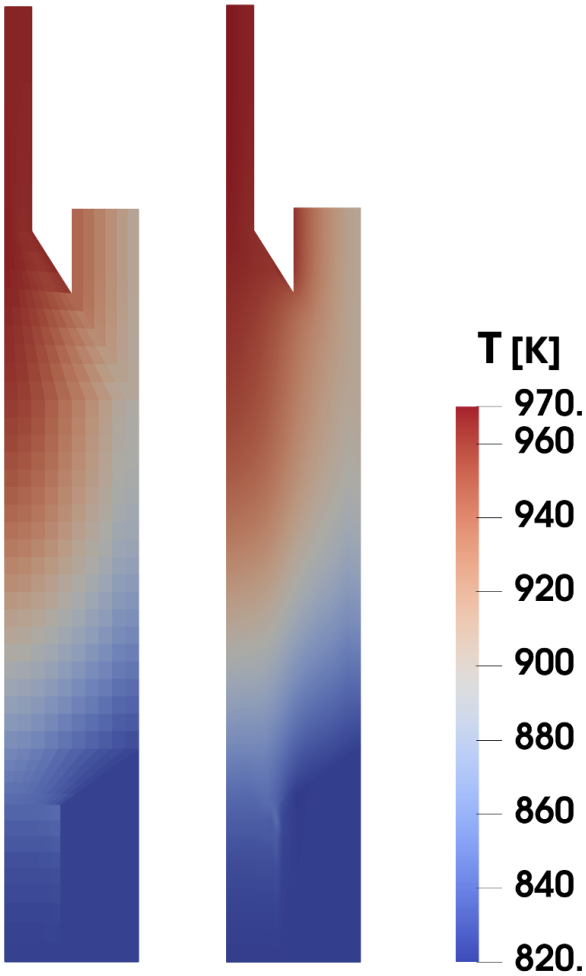

Figure 41. Fluid temperature distributions from Pronghorn (left) and SAM (right).

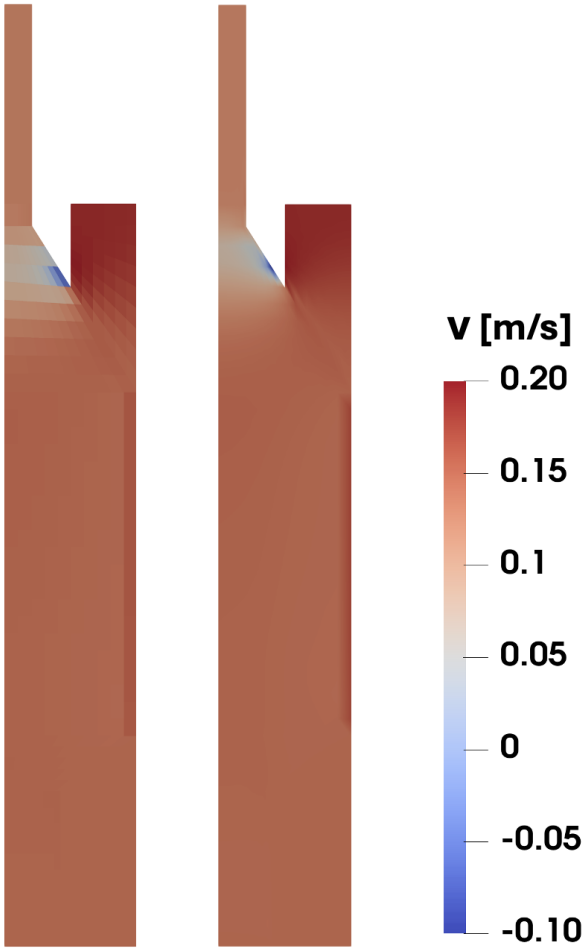

Figure 42. Axial velocity distributions from Pronghorn (left) and SAM (right).

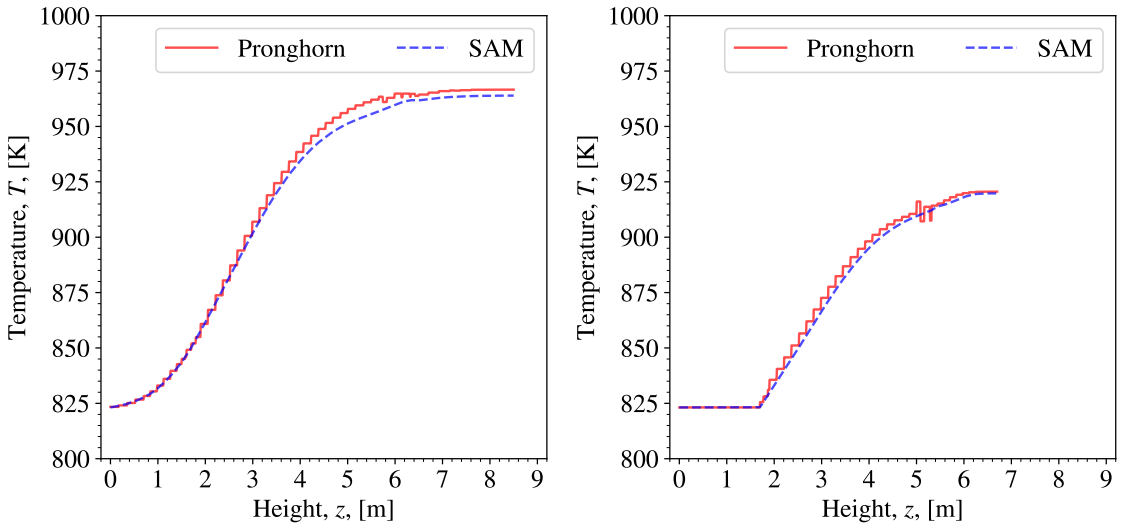

(a) r = 0.15 m (b) r = 0.92 m

Figure 43. Axial temperature distributions from Pronghorn and SAM at x = 0.15 m and x = 0.92 m.

remains nearly constant, as the power density in this region is significantly lower than in the pebble-bed cylindrical core region. In the upper region of the core, Pronghorn predicts a slightly higher fluid temperature than does SAM. At r = 0.92 m, the fluid temperature remains constant at the inlet annulus region, due to there being no power in this region. The temperature begins to increase as the fluid flows upward through the pebble-bed lower cone region. Figure 44 compares the radial fluid temperature distributions at four different elevations. The radial fluid temperature distributions from SAM and Pronghorn again show good agreement. As is consistent with the axial power profiles, Pronghorn predicts a slightly higher fluid temperature than does SAM at the top of core center region. Figure 45 compares the axial velocity at four different elevations. The radial velocity is several orders of magnitude less than the axial velocity during steady state, so it is considered negligible and thus not shown here. In the fueling chute, the axial velocity from Pronghorn is about 0.002 m/s higher than that of SAM, while in the top of core center region the axial velocity from Pronghorn is about 0.002 m/s less than that from SAM. Overall, the axial velocity profiles from Pronghorn and SAM are in close agreement across the core.

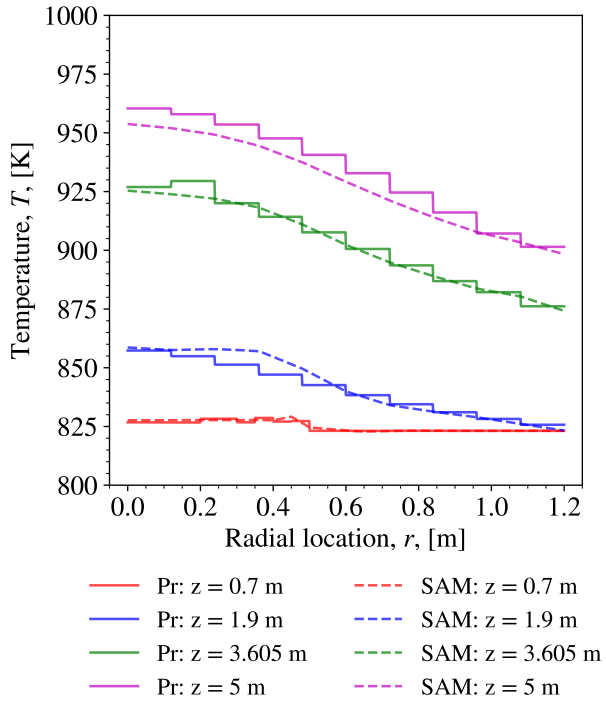

Figure 44. Radial fluid temperature distributions (at different elevations) from Pronghorn and SAM.

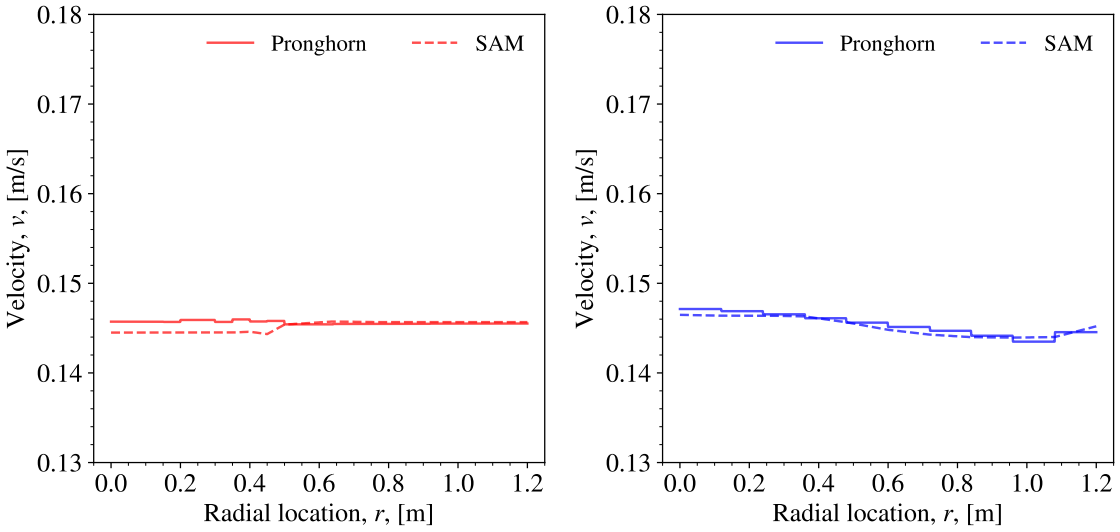

(a) z = 0.7 m

(b) z = 1.9 m

(c) z = 3.605 m

(d) z = 5 m

Figure 45. Radial velocity distributions from Pronghorn and SAM.

3.1.3. SAM/Griffin and Pronghorn/Griffin Core-Only Comparison

This section compares the coupled SAM/Griffin and Pronghorn/Griffin results. In both the SAM and Pronghorn models, only the 2-D porous media model for the core is included. For this comparison, the primary, secondary, and RCCS loop models are excluded in both calculations. The same mesh is applied in the SAM and Pronghorn simulations, as shown in Figure 13. The correlations in the SAM and Pronghorn 2-D core porous media calculation are listed in Table 33. Unlike the SAM and Pronghorn standalone simulation discussed in Section 3.1.2, the power density distributions in this section were obtained through coupling with Griffin. The same Griffin mesh and model were applied in two simulations. Specifically, the baseline Griffin mesh was employed, as shown in Figure 7.

With consistent modeling assumptions and boundary conditions, the SAM/Griffin and Pronghorn/Griffin simulation results showed close agreement. Table 35 compares the core inlet and outlet results. The theoretical value for the average core outlet temperature is 923.15 K. SAM predicted an average outlet temperature of 923.10 K, while Pronghorn yielded 923.14 K, indicating that both models preserve energy balance across the core. The predicted flow split at the core outlet between the defueling chute and outlet annulus was 3.6% and 96.4%, respectively, in the SAM simulation. In the Pronghorn simulation, the corresponding values were 3.7% and 96.3%. Figures 47, 48, and 49 compare the solid temperature, fluid temperature, and axial velocity distributions, respectively. These distributions for the SAM and Pronghorn results are all in good agreement with each other.

Figure 50 shows the axial fluid temperature profiles at two radial positions: r = 0.15 m and r = 0.92 m. As in the SAM and Pronghorn standalone results in Section 3.1.2, the coupled SAM/Griffin and Pronghorn/Griffin simulations show good agreement at both locations. At r = 0.15 m, Pronghorn predicts a slightly higher fluid temperature than SAM in the upper region of pebble bed cylindrical core. In the defueling chute region, the temperature profiles from both models align closely. Figure 51 compares the radial fluid temperature distributions at four different elevations from Pronghorn and SAM. Pronghorn/Griffin consistently predicts slightly higher fluid temperature than SAM/Griffin near the top of core center region. Figure 52 compares the axial velocity at four different elevations. These results are consistent with the trends observed in SAM and Pronghorn standalone simulations presented in Section 3.1.2. In the fueling chute, the axial velocity from Pronghorn is about 1.4% higher than SAM results, while in the top center region of the core, the axial velocity from Pronghorn is about 1.3% lower than the SAM results. Overall, the axial velocity profiles from Pronghorn/Griffin and SAM/Griffin are in good agreement across the core.

Table 35. Comparison of the coupled SAM/Griffin and Pronghorn/Griffin results.

Parameter	SAM/Griffin	Pronghorn/Griffin
Mass flow rate [kg/s]	1324.7	1324.4
Coolant inlet temp. [K]	823.15	823.15
Coolant outlet temp. [K]	923.10	923.14
Flow split in defueling chute [%]	3.6	3.7
Flow split in outlet annulus [%]	96.4	96.3
Pressure drop from core inlet to hotwell inlet [MPa]	0.248	0.241

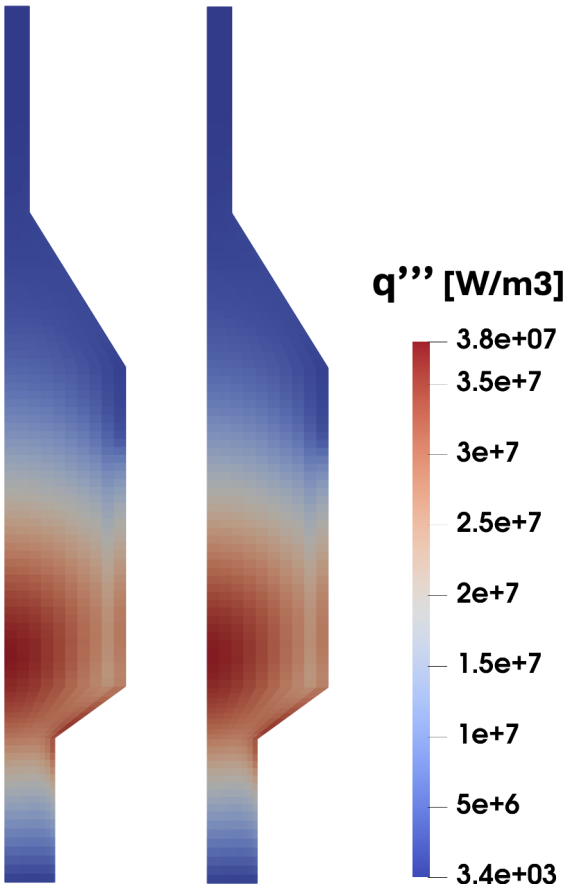

Figure 46. Power density distributions from coupled Pronghorn/Griffin (left) and SAM/Griffin (right).

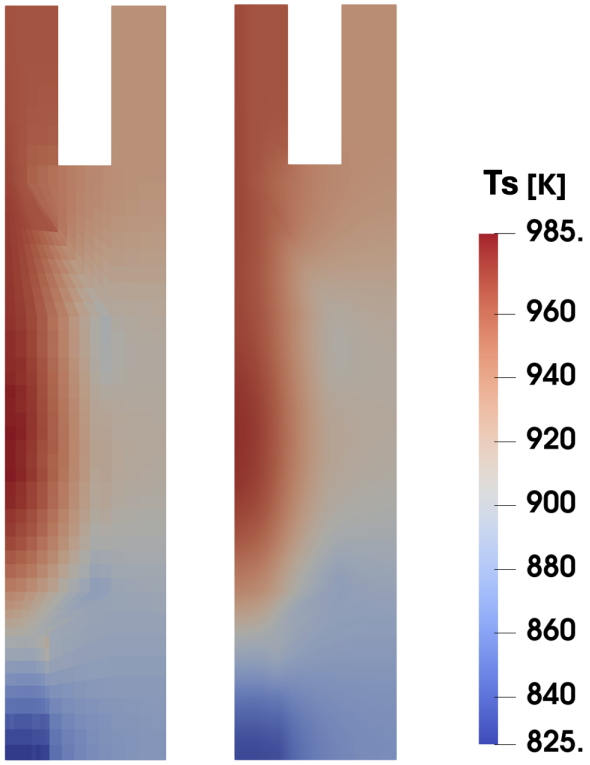

Figure 47. Solid temperature distributions from coupled Pronghorn/Griffin (left) and SAM/Griffin (right).

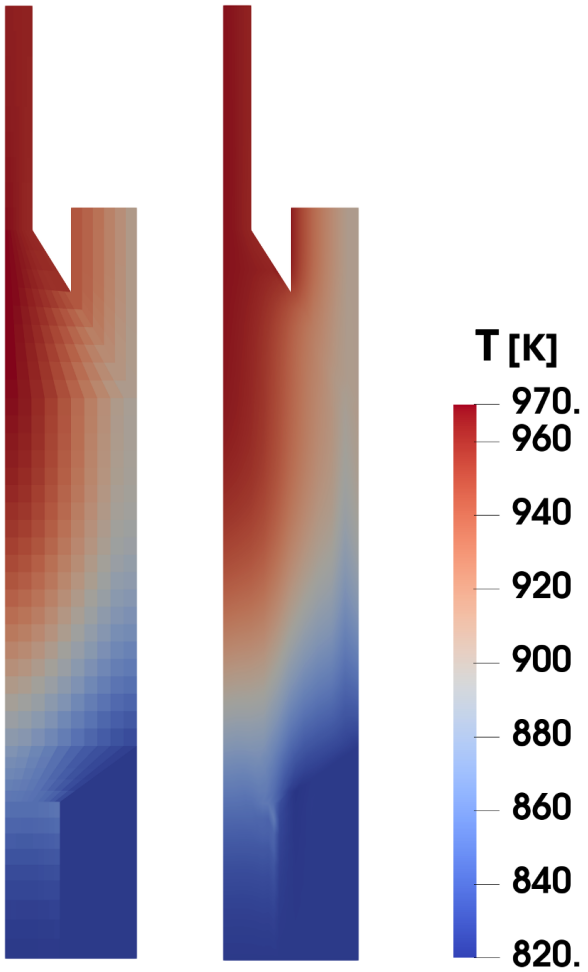

Figure 48. Fluid temperature distributions from coupled Pronghorn/Griffin (left) and SAM/Griffin (right).

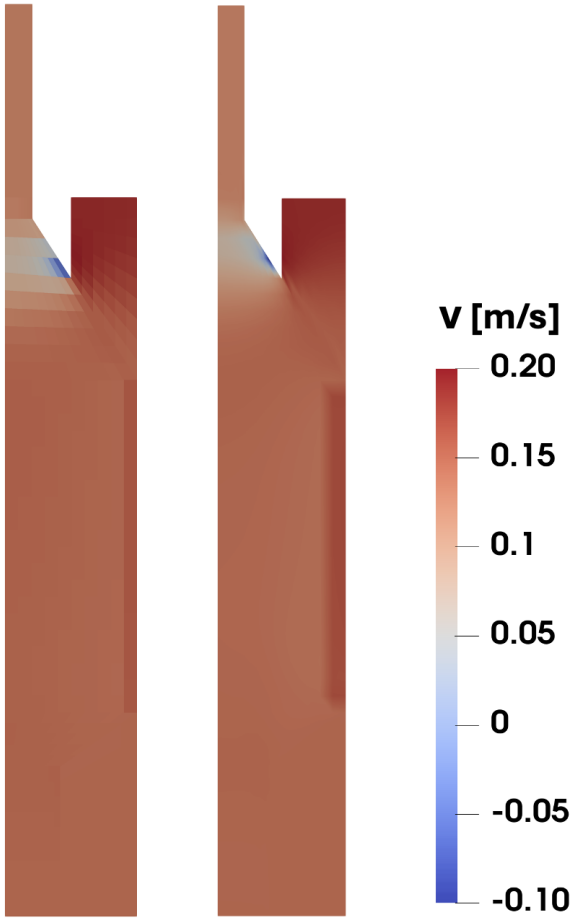

Figure 49. Axial velocity distributions from coupled Pronghorn/Griffin (left) and SAM/Griffin (right).

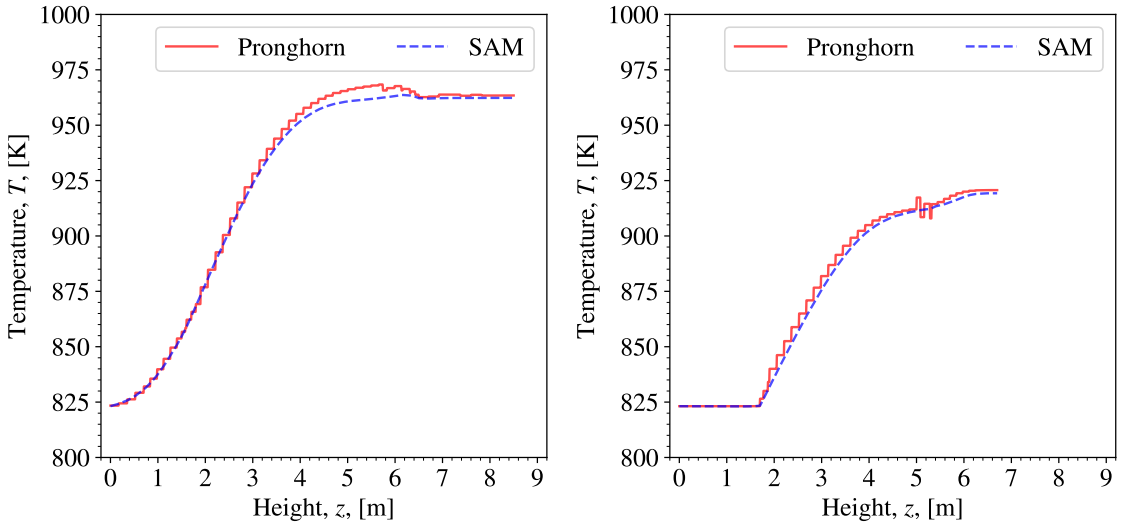

(a) x = 0.15 m (b) x = 0.92 m

Figure 50. Axial temperature distributions from coupled Pronghorn/Griffin and SAM/Griffin at x = 0.15 m and x = 0.92 m.

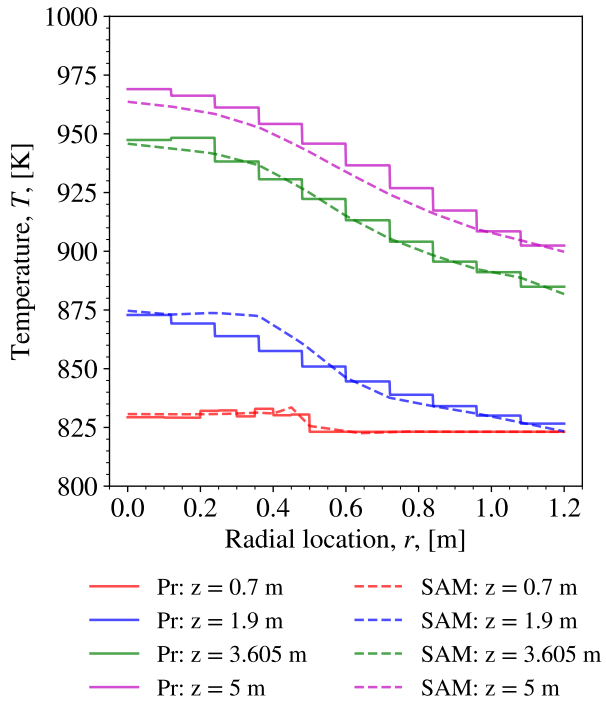

Figure 51. Radial fluid temperature distributions at different elevations from coupled Pronghorn/Griffin and SAM/Griffin.

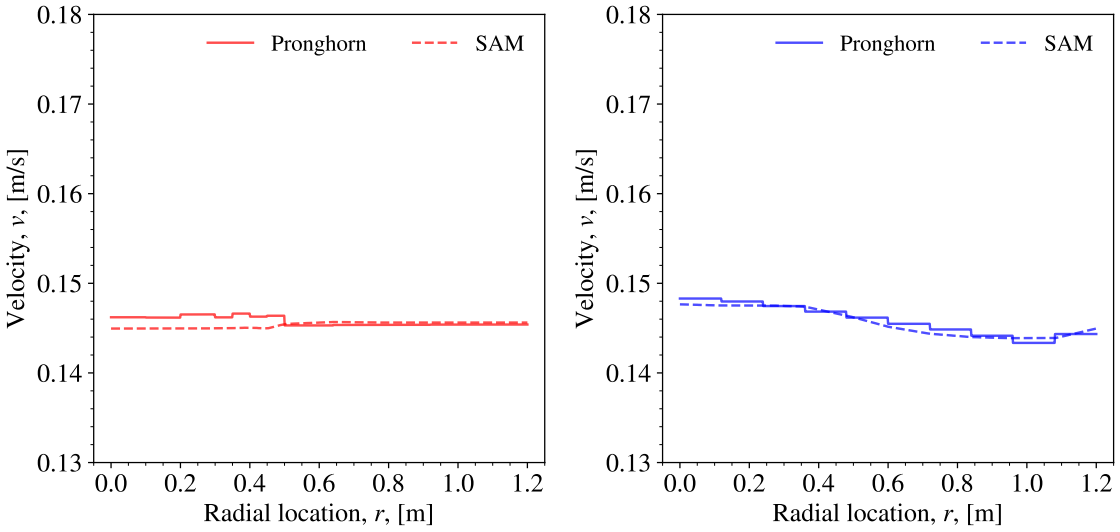

(a) z = 0.7 m

(b) z = 1.9 m

(c) z = 3.605 m

(d) z = 5 m

Figure 52. Radial velocity distributions from coupled Pronghorn/Griffin and SAM/Griffin.

3.1.4. Steady-State SAM Single-Solve and Domain-Overlapping Comparison

This subsection compares the single-solve and domain-overlapping approaches as applied to the steady-state simulation of the full PB-FHR system that includes the RCCS. The single-solve and domain-overlapping approaches were discussed previously in Section 2.5.1. The full PB-FHR system model can be referred to in schematic drawings in Figure 20 for the single-solve approach, and Figure 22 for the domain-overlapping approach, respectively. It is noted that though the RCCS is not shown in Figure 20, it is included in the simulation. For both approaches, the steady-state results were obtained by running null transient simulations until steady states were achieved.

Comparisons between the two approaches were made based on two types of parameters. Table 36 lists the "global" parameters for comparison, including the mass flow rates through the core and the bypass channel, inlet and outlet plenum temperatures as bases for the core temperature rise, and the heat loss to the RCCS. As summarized in Table 36, all parameters included for comparing the two approaches showed very good agreement.

An additional comparison was made for "local" parameters such as the core coolant temperature radial distributions at different elevations. As shown in Figure 53, the agreement between the two approaches is very good.

Based on comparisons of both the global and local parameter values seen in the results from the single-solve and domain-overlapping approaches, it can be concluded that the SAM/SAM domain-overlapping approach can produce results almost identical to those of the single-solve approach.

Table 36. Comparison of SAM/SAM single-solve and domain-overlapping steady-state results.

Parameter	Single-solve	Domain overlapping	Difference
Core mass flow rate [kg/s]	1172.66	1172.59	-0.0060%
Bypass mass flow rate [kg/s]	150.30	150.29	-0.0067%
Inlet plenum temperature [K]	823.08	823.29	0.0255%
Outlet plenum temperature [K]	923.21	923.53	0.0347%
Core temperature rise [K]	100.13	100.24	0.1099%
RCCS cooling [MW]	1.022	1.033	1.0763%

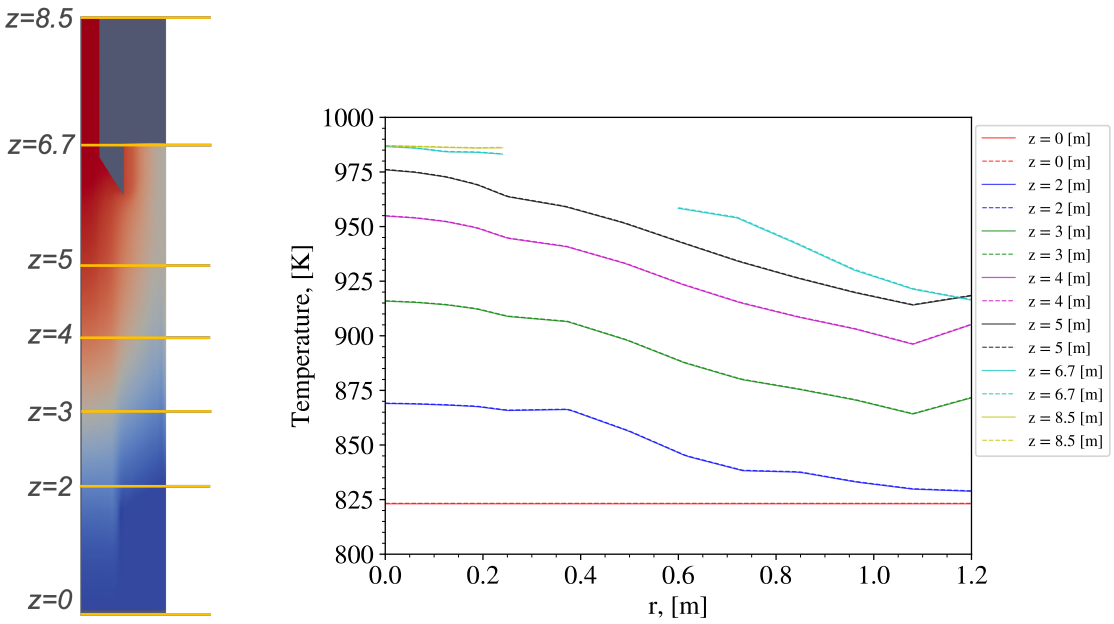

Figure 53. Comparison of fluid temperatures at different vertical locations in the core when using the domain-overlapping and single-solve approaches.

3.1.5. Initial Condition for the 2-D Loss-of-Forced-Circulation Scenarios

This section compares the initial steady-state conditions for the LOFC scenarios when using Pronghorn/Griffin and SAM/Griffin/SAM, as shown in Table 37. Note that the Griffin and Pronghorn models in the Pronghorn/Griffin simulation of LOFC scenarios differ from those in Section 3.1.3. The baseline mesh was used for the Griffin model in Section 3.1.3, as depicted in Figure 7. However, a different mesh was applied to the Griffin models in the coupled Pronghorn/Griffin simulations in this section, as shown in Figure 12. The Pronghorn mesh in this section and in Section 3.1.3 are also different, as illustrated in Figures 13 and 16(b), respectively.

Additionally, there are differences in the closure correlations when comparing the Pronghorn 2-D porous media models in this section and in Section 3.1.3, as shown in Tables 33 and 19. In this Pronghorn model, the pebble-bed and reflector thermophysical properties are temperature- and fluence-dependent. A multi-scale pebble model [26] implemented in SAM solves a built-in 1-D heat conduction model for each pebble at every mesh element of the porous medium model, and includes a lumped parameter model for TRISO fuel kernel temperature. This model was used in the SAM/Griffin/SAM simulation, while the Pronghorn/Griffin model employed a 1-D BISON solid conduction model for both pebbles and TRISO particles for each pebble burnup group in the pebble bed, with thermophysical properties that are temperature- and fluence-dependent.

Due to these differences between the two modeling approaches, the steady-state results between SAM/Griffin/SAM and Pronghorn/Griffin show more discrepancies than the results in Section 3.1.3, but they illustrate the expected range of results under different modeling assumptions. The largest difference in the initial conditions is in the reflector temperature, and is primarily driven by differences in the conductivities for the pebble-bed and reflector zones in Pronghorn. Consequently, this affects the fuel and moderator temperatures and coolant densities, leading to a discrepancy in the eigenvalue of 344 pcm. As a result, there is a 20 K bias between the SAM/Griffin and Pronghorn/Griffin initial conditions when it comes to the feedback temperatures. Another notable finding is the significant difference in the average power density, which is considerably lower in the Pronghorn model. This discrepancy will be further examined in future work.

Table 37. Comparison of steady-state core neutronics parameters for the Pronghorn/Griffin and SAM/Griffin models for the 2-D LOFC scenarios.

Parameter	Pronghorn	SAM	% Rel. diff. or pcm
k_{eff}	1.00711	1.00367	-344 (pcm)
Total core power [MWth]	320.0	320.0	0.
Pebble power density avg [MW/m^3]	2.660e+07	2.711e+07	1.91
Pebble power density max [MW/m^3]	7.083e+07	7.690e+07	8.56
Pebble power peak	1.29	1.28	-0.51
CR position [m]	4.225	4.225	0.00
Pebble surface temp. [K]	922.73	943.46	-1.30
Fuel avg. temp. [K]	969.15	975.20	0.62
Fuel max. temp. [K]	1073.39	1066.68	-0.63
Mod avg. temp. [K]	940.35	956.28	1.69
Mod max. temp. [K]	1013.31	1029.20	1.57
Reflector temp. [K]	853.78	832.76	-2.46
Coolant density avg. [kg/m^3]	1976.79	1972.26	0.23
Coolant density max. [kg/m^3]	2010.77	2011.43	-0.03

3.1.6. Initial Condition for the Simplified 2-D Control Rod Movement Accident Scenarios

This comparison used the baseline mesh for the neutronics and thermal fluids coupling. Table 38 compares key parameters pertaining to the initial conditions of the coupled model when using the overlapping domain approach in Pronghorn/Griffin/SAM and the single-solve approach in SAM/Griffin/SAM. In the Pronghorn/Griffin model, the thermophysical properties of the pebble bed and reflector are constant. In the BISON model, only the kernel is temperature-dependent. Therefore, the differences in the results primarily stem from the treatment of the pebble and TRISO conduction problem.

Upon examination, the coolant densities and pebble surface temperatures show good consistency when comparing the models. The reflector temperatures are also in good agreement. The main difference lies in the fuel and moderator temperatures, which show a bias of 10–15 K. This temperature feedback discrepancy explains the -134 pcm difference between the two coupled models and suggests that in the LOFC initial conditions from the previous section, the pebble-bed and reflector conductivities account for the remaining -210 pcm discrepancy.

Table 38. Comparison of steady-state core neutronics parameters for the Pronghorn/Griffin and SAM/Griffin models.

Parameter	Pronghorn	SAM	% Rel. diff. or pcm
k_{eff}	0.95696	0.95568	-133.5 (pcm)
Total core power [MWth]	320.0	320.0	0.
Pebble power density avg. [MW/m^3]	2.695e+07	2.695e+07	0.00
Pebble power density max. [MW/m^3]	1.169e+08	1.151e+08	-1.60
Pebble power peak	1.23	1.23	-0.16
CR position [m]	2.37	2.37	0.00
Pebble surface temp. [K]	944.59	943.46	-0.12
Fuel avg. temp. [K]	972.11	983.03	1.12
Fuel max. temp. [K]	1138.51	1158.77	1.78
Mod avg. temp. [K]	948.22	964.24	1.69
Mod max. temp. [K]	1058.96	1095.51	3.45
Reflector temp. [K]	842.13	834.69	-0.88
Coolant density avg. [kg/m^3]	1966.83	1968.04	0.06
Coolant density max. [kg/m^3]	2012.78	2011.93	-0.04

3.1.7. Initial Condition for the 3-D/2-D/0-D Control Rod Movement Accident Scenarios

The neutronic initial conditions for the 3-D and 2-D models, with all rods banked at 2.21 m, are shown in Table 39. There is excellent agreement in the initial conditions, with a bias of only 5 K in the pebble surface, moderator, and fuel temperatures. The thermal fluids initial conditions for the 3-D and 2-D models are shown in Table 40. The same 5 K bias is observed in the core fluid temperature, which increases in the cone and defueling chute. The outlet annulus conditions are consistent between the 3-D and 2-D Pronghorn models.

Table 39. Comparison of steady-state core neutronics parameters for the Pronghorn/Griffin 3-D and 2-D models with control rods at 2.21 m.

Parameter	3-D	2-D	% Rel. diff. or pcm
k_{eff}	0.97313	0.97313	0.10
Total core power [MWth]	320	320	0.00
Pebble power density avg. [MW/m^3]	2.6503e+07	2.6502e+07	0.00
Pebble power density max. [MW/m^3]	9.2003e+07	9.2129e+07	0.14
Pebble power peak	1.29	1.29	-0.17
CR position [m]	2.21	2.21	0.00
Pebble surface avg. temp. [K]	928.51	933.71	0.56
Fuel avg. temp. [K]	975.02	980.35	0.55
Fuel max. temp. [K]	1132.69	1138.14	0.48
Mod avg. temp. [K]	946.17	951.43	0.56
Mod max. temp. [K]	1067.95	1058.60	-0.88
Reflector temp. [K]	888.68	894.93	0.70
Coolant density avg. [kg/m^3]	1974.00	1971.80	-0.11
Coolant density max. [kg/m^3]	2010.83	2010.83	-0.00

Table 40. Comparison of steady-state core fluid parameters for the Pronghorn/Griffin 3-D and 2-D models with control rods at 2.21 m.

Parameter	3-D	2-D	% Rel. diff.
Inlet mass flow rate [kg/s]	1324.60	1324.60	0.00
Inlet annulus mass flow rate [kg/s]	1011.64	1011.64	0.00
Fueling chute fluid temp. [K]	840.97	841.30	0.04
Fueling chute mass flow rate [kg/s]	192.70	192.70	0.00
Lower cone fluid temp. [K]	847.52	848.73	0.14
Core avg. fluid temp. [K]	898.91	903.41	0.50
Cyl. core avg. fluid temp. [K]	894.95	899.40	0.50
Reflector top temp. [K]	975.72	985.42	0.99
Reflector side temp. [K]	884.62	890.71	0.69
Upper cone fluid temp. [K]	952.25	959.17	0.73
Defueling chute mass flow rate [kg/s]	61.99	61.10	-1.43
Defueling chute pressure [Pa]	1.0e5	1.0e5	0.00
Defueling chute fluid temp. [K]	975.44	986.02	1.08
Defueling chute solid temp. [k]	975.94	986.48	1.08
Defueling chute axial velocity [m/s]	0.16	0.16	-1.17
Outlet annulus mass flow rate [kg/s]	1256.70	1257.59	0.07
Outlet annulus pressure [Pa]	1.0e5	1.0e5	0.00
Outlet annulus temp. [K]	921.15	920.67	-0.05
Outlet annulus velocity [m/s]	0.43	0.43	0.07
Barrel temp. [K]	884.57	890.72	0.70

3.2. Protected Loss-of-Forced-Circulation Scenario

3.2.1. 2-D SAM/1-D SAM Results

For this section, the Protected Loss Of Forced Circulation (PLOFC) transient was simulated using the coupled 2-D SAM/1-D SAM model with the single-solve approach. At the start of the transient, the reactor was scrammed and only the decay heat remained. Therefore, this PLOFC simulation does not involve Griffin; instead, a predefined decay heat curve was applied in a coupled 2-D SAM/1-D SAM simulation. The transient simulation was initialized from the steady-state solution obtained from the coupled SAM/Griffin/SAM simulation so as to ensure accurate initial conditions, including the power density distribution.

At the beginning of the transient, the primary and secondary pump heads were assumed to decrease following an exponential coast-down curve with a halving-time of 4.5 s, and complete loss of pump heat was reached at 76.5 s, as shown in Figure 6. The evolution of the core inlet flow rate from the SAM simulation is presented in Figure 54. The pump trip at the beginning of the transient reduced the flow rate in the primary loop. Shortly after the pump shutdown, the fluidic diode opened, enabling natural circulation between the hot core region and the cold downcomer through the diode. As a result, natural circulation was established, reaching approximately 3% of the steady-state inlet flow rate. The decay heat and heat removal through the RCCS loop are shown in Figure 55. After the transient began, the increasing temperature of the primary salt raised the reactor vessel wall temperature, enhancing radiative heat transfer to the RCCS panels. As the decay heat continued to decrease while the RCCS heat removal continued to increase, at ~ 47000 s the RCCS heat removal exceeded the decay heat, initiating reactor cooldown.

Figure 56 (a) presents the time evolution of the core peak fuel kernel and peak pebble temperatures during the transient. Initially, both temperatures dropped sharply due to the sudden loss of fission power. Then the peak fuel kernel and pebble temperature increased because the heat rejected to the RCCS was less than the decay heat. After ~ 65000 s, the peak fuel kernel and pebble temperature started to decrease once the RCCS heat removal rate exceeded the decay heat, and then the core cooled down. Figure 56 (b) shows the core inlet, outlet, and vessel outer surface average temperatures during the PLOFC transient. Oscillatory behavior was observed in both the RCCS heat removal and core temperatures, indicating the presence of flow oscillations in the natural circulation loop during the transient. A closer look at these oscillations is provided in Figure 57, which zooms in on the inlet velocity and core inlet, outlet, and vessel outer surface average temperatures at the oscillation region. The oscillation period was approximately 500 s, indicating this oscillation phenomenon to be physical rather than numerical in nature. However, in a real PB-FHR design, such oscillations may or may not occur, depending on the specific characteristics of the primary loop and RCCS design.

Figures 58 and 59 show the evolution of the fluid temperature distributions and axial velocity distributions throughout the PLOFC transient. Initially, the core temperature decreased, but then it rose until the RCCS heat removal rate exceeded the decay heat. It is noted that at 1000 s in-core circulations were observed at the core bottom and top. These internal circulations dissipated at later times as the flow became predominantly axial. Figure 60 presents the axial and radial profiles of the fluid temperature at the time of peak fuel temperature (t = 64565 s). At r = 0.15 m, the fluid temperature increased through the core inlet, remaining nearly constant within the defueling chute. At r = 0.92 m, the temperature remained constant within the inlet annulus and began to rise upon entering the lower cone region. In the core upper region, the fluid temperatures at r = 0.15 m and r = 0.92 m were basically identical. Such was also the case with the radial temperature distributions at z = 3.605 m and z = 5 m, with the radial temperature distribution becoming flat.

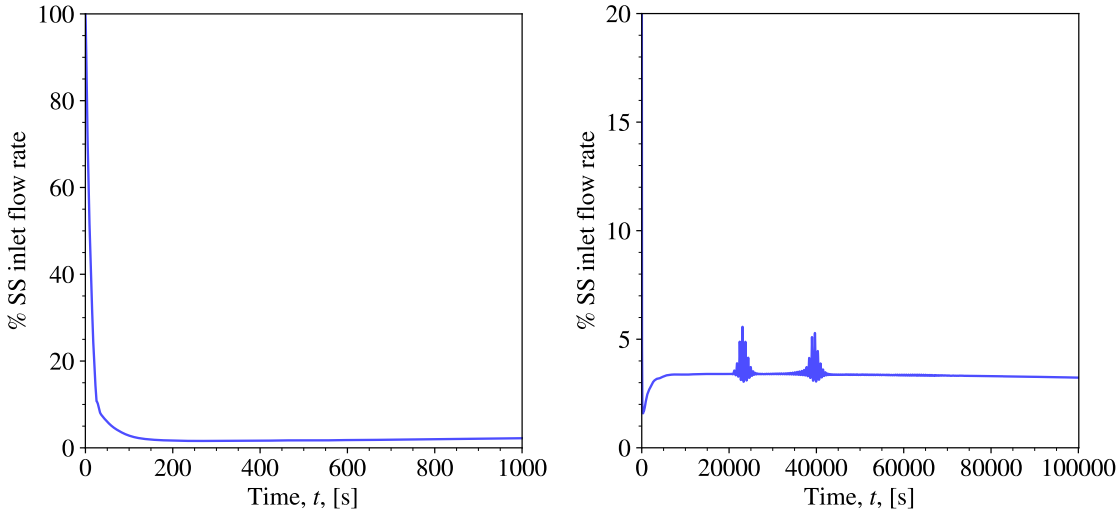

(a) First 1000 s (b) Whole transient

Figure 54. Core inlet velocity of SAM during the PLOFC transient.

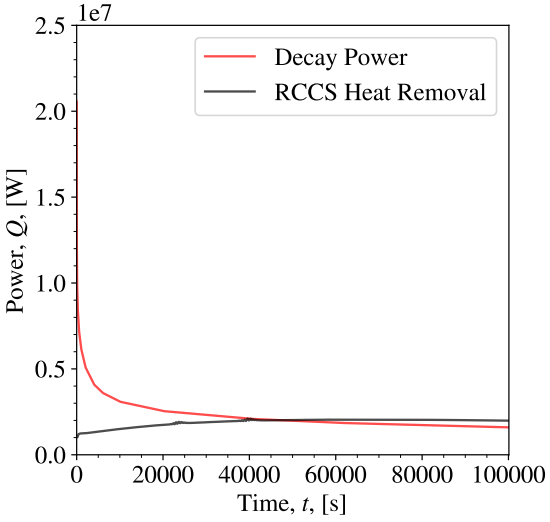

Figure 55. Decay heat and RCCS heat removal rate during the PLOFC transient.

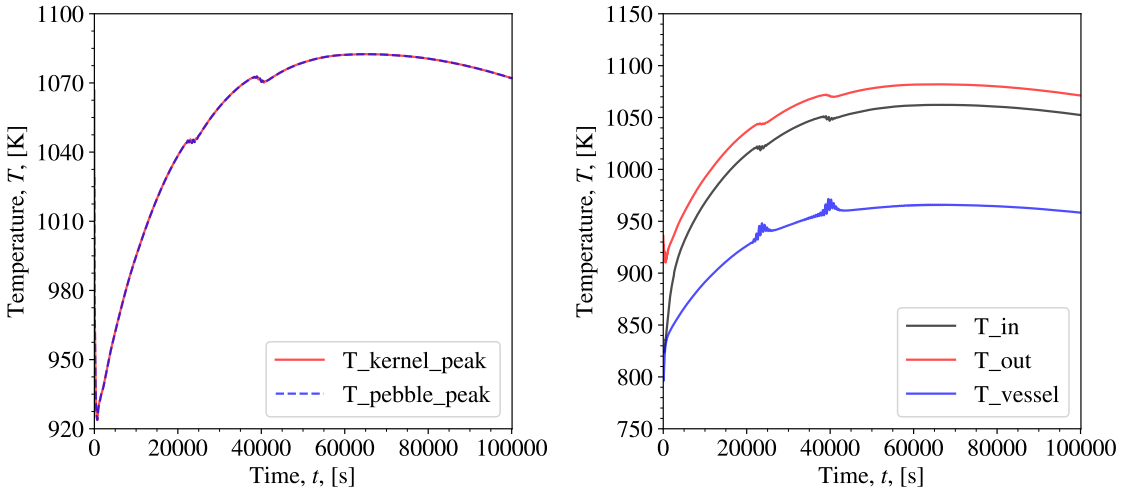

(a) Peak pebble and fuel kernel T (b) Core inlet, outlet, and vessel outer surface T

Figure 56. Peak pebble, fuel kernel, core inlet, core outlet, and vessel outer surface temperature from the SAM calculation during the PLOFC transient.

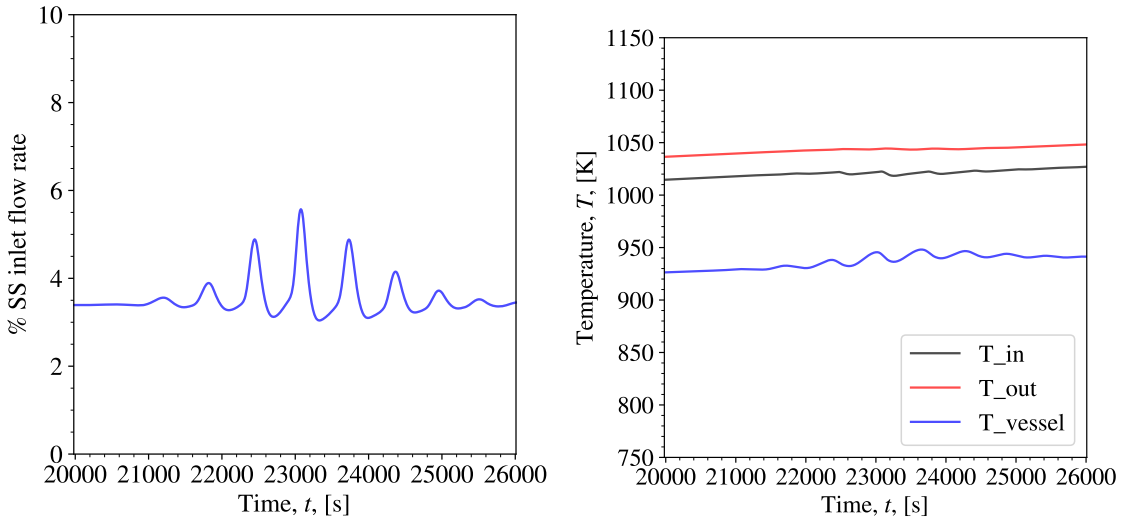

(a) Inlet velocity (b) Core inlet, outlet and vessel out surface T

Figure 57. Inlet velocity and inlet, outlet, and vessel outer surface temperature from the SAM calculation at the oscillation region during the PLOFC transient.

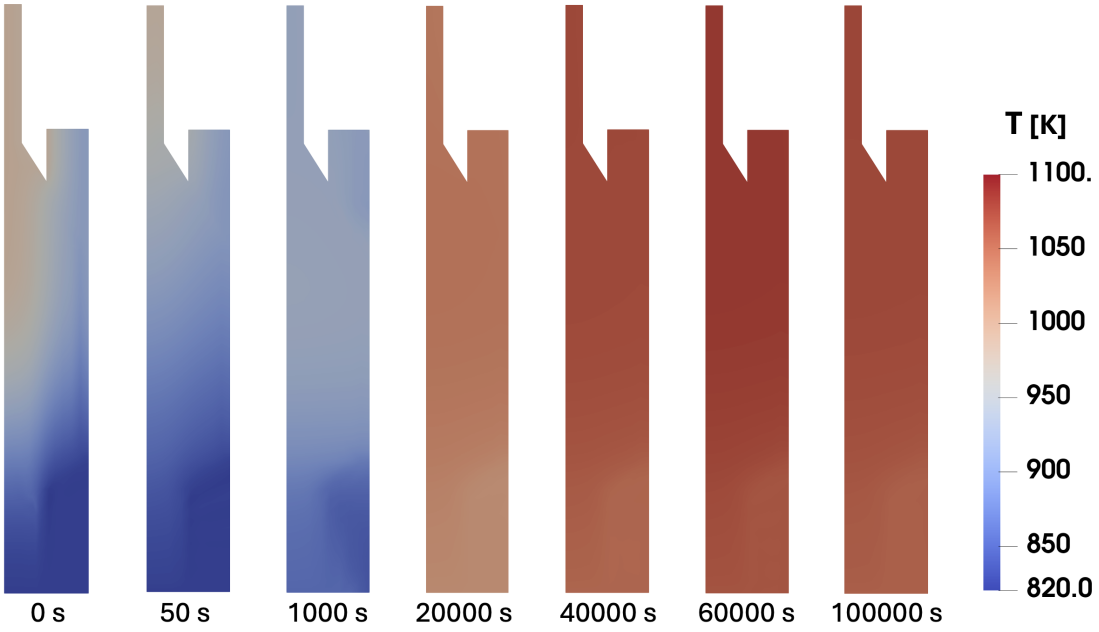

Figure 58. Fluid temperature distributions from SAM during the PLOFC.

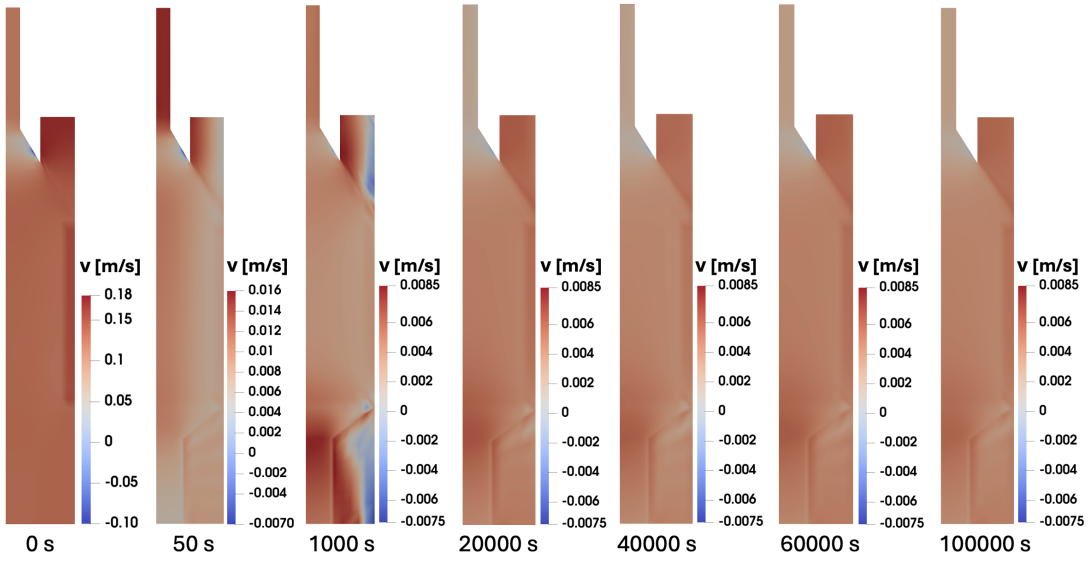

Figure 59. Axial velocity distributions from SAM during the PLOFC.

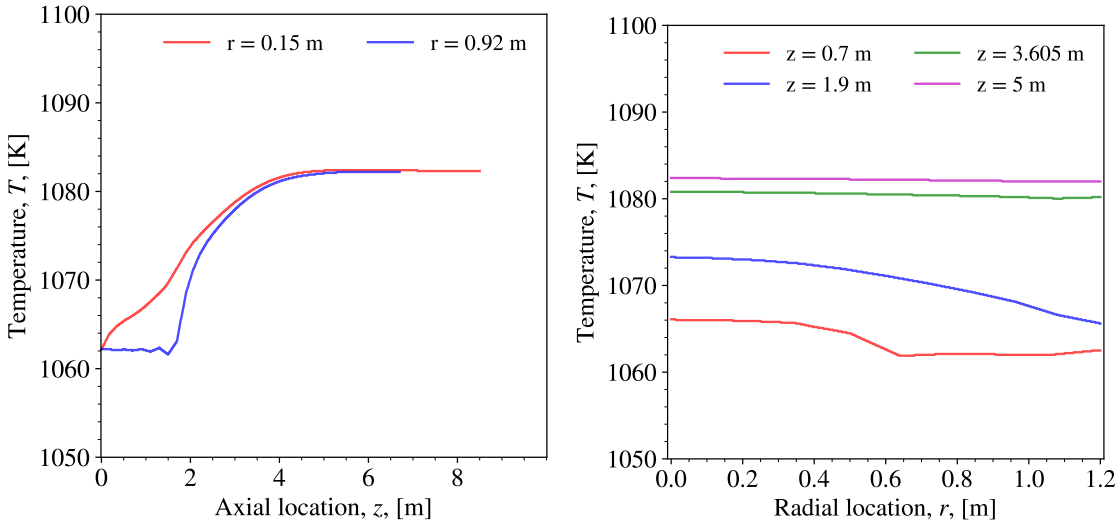

(a) Axial Distributions

(b) Radial Distributions

Figure 60. Axial and radial fluid temperature distributions from SAM during the PLOFC at peak pebble/TRISO-kernel temperatures (t = 64565 s).

3.2.2. 2-D Pronghorn/Griffin Results

This section provides results pertaining to the Pronghorn/Griffin coupled PLOFC transient. The model consists of the core, reflector, plena, diode, and downcomer in the 2-D R-Z Pronghorn model. During the transient, the inlet and outlet of the core were replaced with walls, as it was assumed that this flow was negligible compared to the mass flow rate of the circulation through the diode. During the steady-state simulation, the diode in the Pronghorn model was initially closed via the use of "hydraulic separators" in Pronghorn, which essentially isolated the fluid in the diode from the rest of the domain. These separators were removed during the transient, thus opening the diode and allowing flow to pass through.

The flow path of the fluid through the core during the PLOFC transient is shown in Figure 61. The snapshot in Figure 61 was taken at roughly t = 6000 s. From this figure, it can be seen that the coolant followed the expected flowpath once the diode was opened: it entered the bottom of the core, rose quickly through the heated region, and eventually flowed up and through the fluidic diode before descending in the downcomer and returning to the inlet plenum. The complex nature of this case can also be seen, as there are several clear regions of minor recirculation in addition to the main flowpath. These minor recirculations tend to occur in unheated regions adjacent to the reflector, such as in the inlet and outlet plena. Recirculations such as these are expected, as hot fluid from the core will be cooled by the reflector, increasing its density and causing it to move downward. The additional recirculations are a key factor in why multidimensional simulation is necessary for transient simulations of these cores, as the flow demonstrates several multidimensional features not capturable by 0-D or 1-D models.

The primary flow path, however, occurred through the fluidic diode. The mass flow rate through the flow diode is shown in Figure 62. This mass flow rate was initially high, as the reactor power was still slightly elevated, providing substantial buoyancy for natural circulation. As the reactor power dropped, so too did the natural circulation, and the flow through the diode steadily decreased.

The FLiBe velocity and temperature at several instances throughout the PLOFC transient are shown in Figures 63 and 64. The fluidic diode was initially closed at t = 0 s, and the fluid temperature was only affected by conduction from the surrounding structure. By t = 50 s, the diode had opened, and hot fluid from the outlet plenum and hotwell could then be seen to enter the diode and begin to flow down the downcomer.

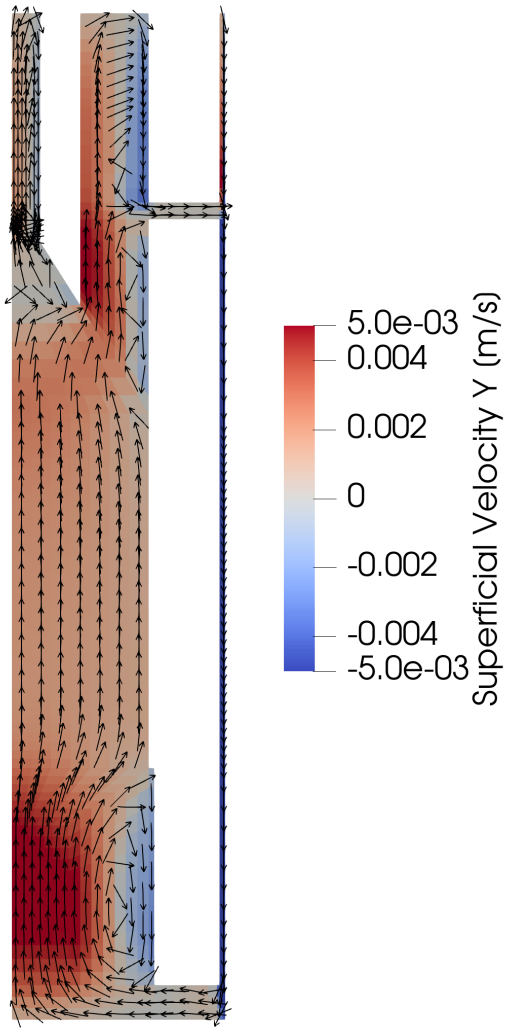

Figure 61. Flow path of FLiBe through the core in the PLOFC transient, with Pronghorn/Griffin coupling.

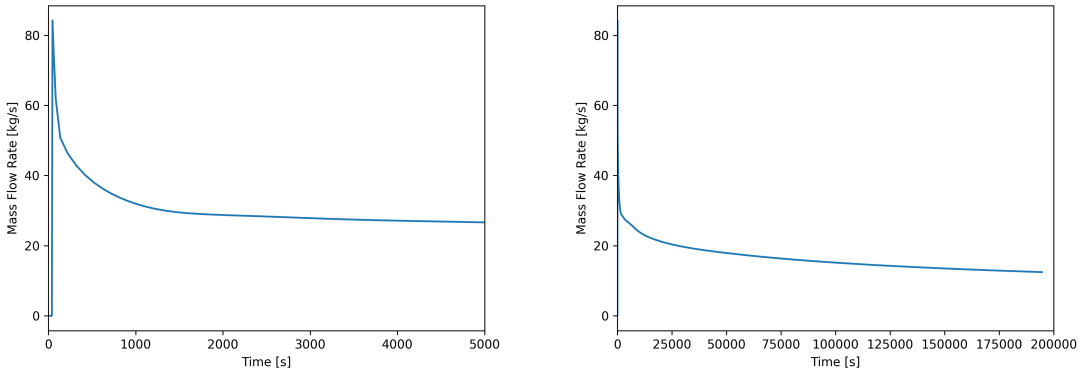

(a) First 5000 s

(b) Whole Transient

Figure 62. Mass flow rate through the fluidic diode during the PLOFC transient, with Pronghorn/Griffin coupling.

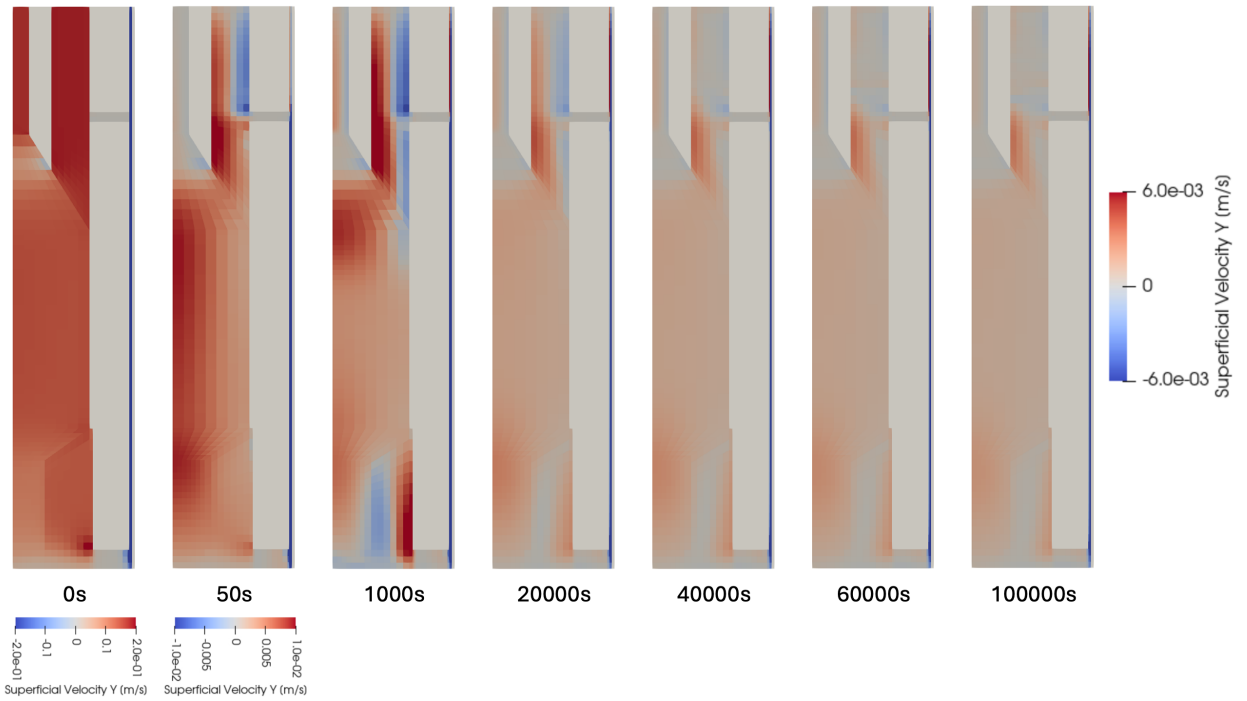

Figure 63. Superficial velocity in the y-direction at several snapshots throughout the PLOFC, with Pronghorn/Griffin coupling. Note that the plots for t = 0 s and t = 50 s use a different scale than the rest of the plots.

At t = 1000 s, the cooling effect of the downcomer became visible, as a large gradient existed between the diode/downcomer interface and the downcomer/bottom plenum interface. The temperature rose until the RCCS began to remove more heat than what was generated by the decay power, and the temperatures gradually decreases in the final three snapshots.

The reactor power and decay heat removal are shown in Figure 65. The reactor total power quickly dropped due to loss of fission power as the reactor was shut down a the start of the transient. The power then continued to decrease with the decay power. The RCCS heat removal initially increased due to the increased temperatures in the core, and it exceeds the total decay power at around t = 30,000 s. From there, it slowly decreased as the reactor gradually cooled for the remainder of the transient.

Figure 66 shows the core average and maximum graphite temperatures, along with the vessel temperature. All three temperatures initially rose for the first 25,000 seconds as the primary reactor flow was lost. As heat was transferred to the structural components and eventually to the vessel, the RCCS power increased until it overcame the decay heat generation seen in Figure 65. After this point, all three temperatures began to decrease for the remainder of the transient.

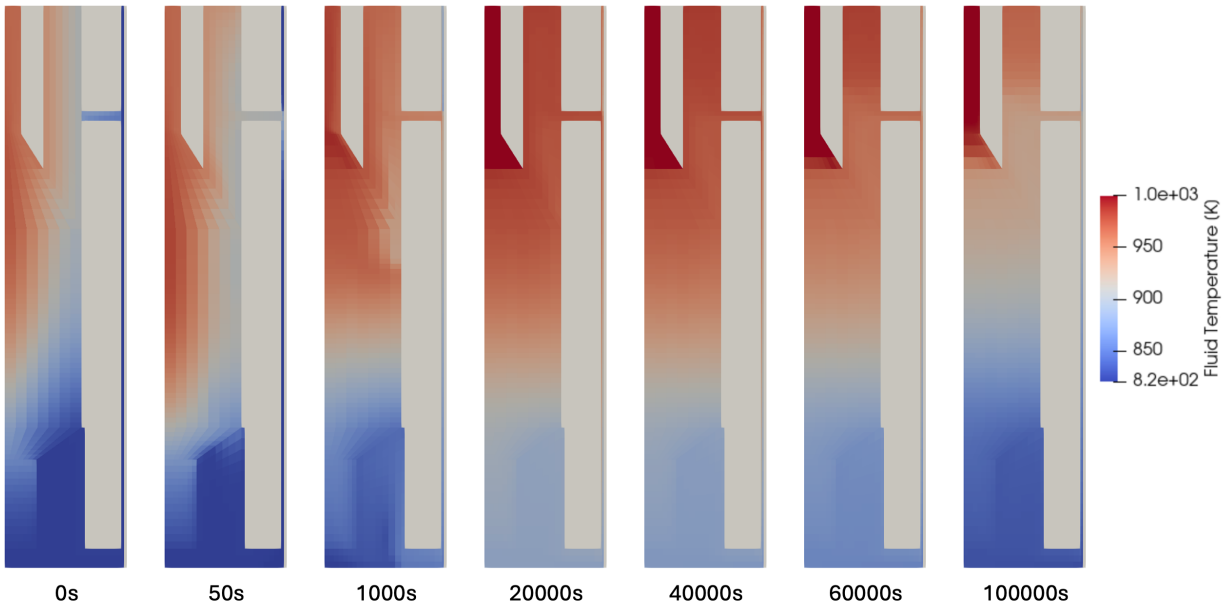

Figure 64. FLiBe temperature at several snapshots throughout the PLOFC, with Pronghorn/Griffin coupling.

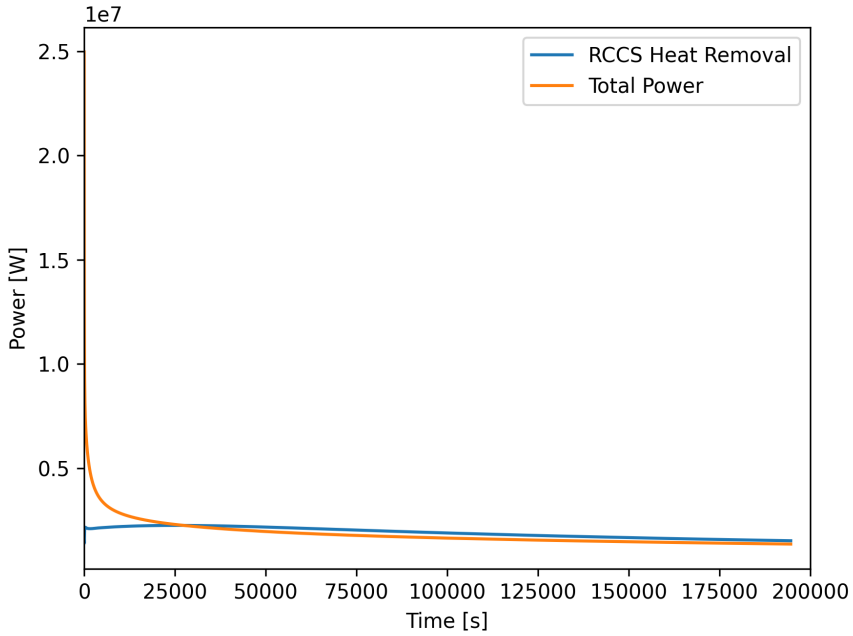

Figure 65. Total core power and RCCS heat removal power during the PLOFC transient, with Pronghorn/Griffin coupling.

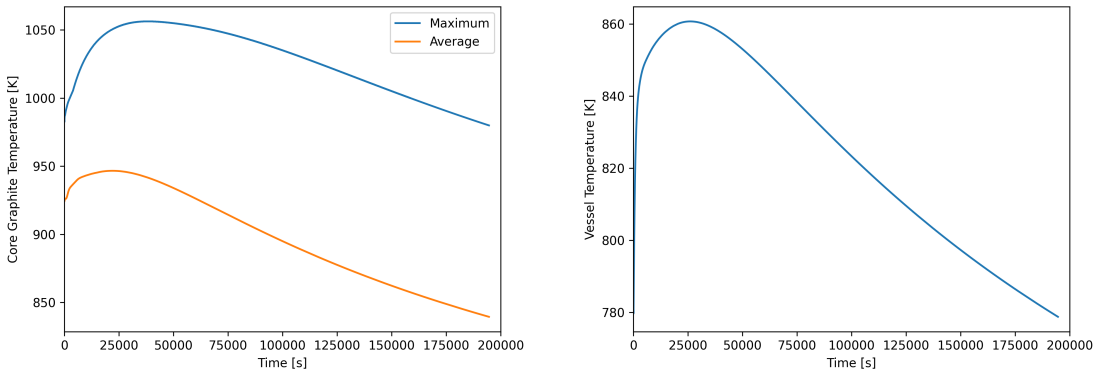

(a) Core graphite

(b) Vessel

Figure 66. Average and maximum core graphite temperature and average vessel temperature for the PLOFC transient, with Pronghorn/Griffin coupling.

3.2.3. Comparison of the 2-D SAM/1-D SAM and 2-D Pronghorn/Griffin Results

In the analysis of the PLOFC scenario, both 2-D SAM/1-D SAM and 2-D Pronghorn/Griffin predicted that the RCCS could adequately remove decay heat following reactor shutdown. Overall, the two simulations exhibited similar trends in the RCCS heat removal rates. Figure 67 (a) shows the power and RCCS heat removal rate during the PLOFC transient. Because a predefined decay heat curve was applied in the coupled 2-D SAM/1-D SAM simulation, whereas in the Pronghorn simulation the power was calculated by Griffin, a small power discrepancy existed between the two simulations. The RCCS heat removal rate from Pronghorn exceeded that from SAM at the beginning of the transient. In the later stage of the transient, the RCCS heat removal rates from the two simulations converged to a similar value. However, due to differences in the RCCS modeling approaches, Pronghorn predicted a lower vessel wall temperature, as shown in Figure 67(b). The Pronghorn/Griffin simulation did not include a coupled RCCS loop model, whereas the 2-D SAM/1-D SAM simulation incorporated a RCCS model within the SAM 1-D system model. This affected the panel temperatures and the resulting radiative heat transfer to the RCCS surfaces.

The downcomer mass flow rates from the two simulations are presented in Figure 68. In the 2-D SAM/1-D SAM simulation, pump coastdown was modeled by reducing the pump head in accordance with an exponential decay function in the SAM 1-D system model. In contrast, the Pronghorn/Griffin simulation did not account for pump coastdown, as it was not coupled to the SAM 1-D system model. Instead, in the Pronghorn model, the core outlet and downcomer inlet boundaries were set to wall conditions at the beginning of the transient. A fluid diode was then opened at a later time to establish a natural circulation flow path. This modeling difference resulted in a reduced mass flow rate, and thus reduced the heat removal from the core for approximately the first 300 seconds of the transient in the Pronghorn/Griffin simulation. These differences between the two models will be addressed in future work with the fully coupled Pronghorn/Griffin/SAM simulation, once the overlapping domain coupling between the Pronghorn 2-D core porous media model and the SAM 1-D loop model becomes available.

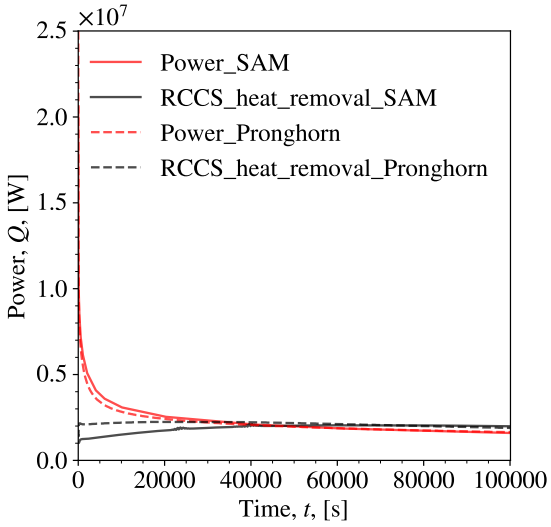

(a) Power and RCCS heat removal rate

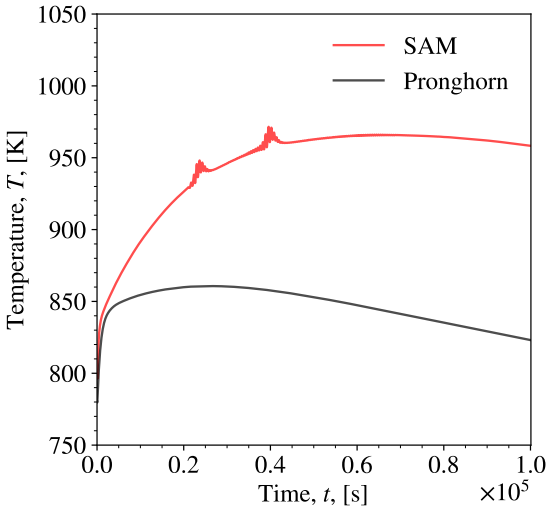

(b) Vessel wall temperature

Figure 67. Power, RCCS heat removal rate, and vessel wall temperatures from 2-D SAM/1-D SAM and Pronghorn/Griffin calculations during the PLOFC transient.

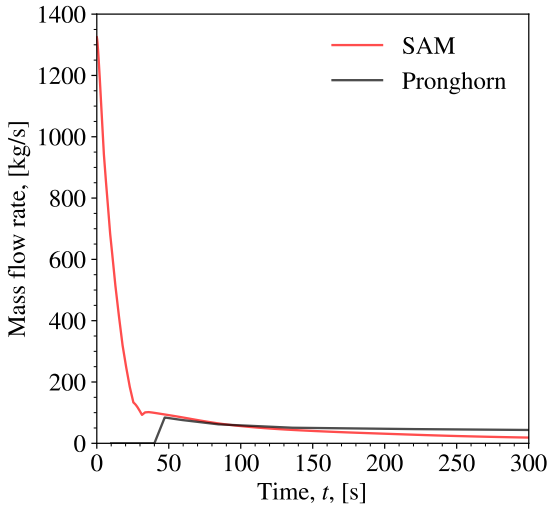

(a) First 300 s

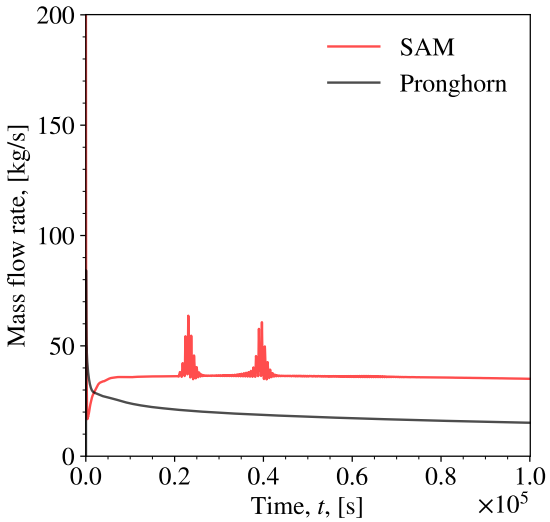

(b) Whole transient

Figure 68. Downcomer mass flow rate temperatures from 2-D SAM/1-D SAM and Pronghorn/Griffin calculations during the PLOFC transient.

3.2.4. SAM Single-Solve and Domain-Overlapping Comparison

This section compares PLOFCs as an extension of the steady-state results comparison covered in Section 3.1.4. In this section, both the SAM single-solve and SAM/SAM domain-overlapping approaches were used to simulate the PLOFC event as described in Section 1.2.1. During the PLOFC, as the pump coastdown and pump head reduced, the core flow decreased with time. As the pressure difference across the fluidic diode reduced, the diode opened to enable a pathway for natural circulation to develop.

As in Section 3.1.4, both global and local parameters from the results were used for the comparison. Figure 69 shows the mass flow rate through the fluidic diode, as taken from both approaches. Per the figure, both approaches consistently predict the fluidic diode mass flow rate (i.e., the time at which the diode opens, the value and time of the peak mass flow rate, and the overall behavior of the reduction in flow rate following the peak. Figure 70 compares the inlet and outlet plena temperatures between the two approaches. Overall, the comparison showed good agreement between the two methods.

Figures 71 to 75 compare the "local" core coolant temperature distributions at different core vertical locations and at different times (i.e., at 10, 50, 100, 300, and 600 seconds after initiating the PLOFC transient). The vertical locations can be referred to in Figure 53. As in the steady-state results comparison, the local coolant temperatures showed very good agreement between the two modeling approaches. However, a few minor deviations were observed; for example, z = 6.7 [m] in Figures 73 and 74, and z = 0 [m] in Figure 75. The temperature difference in Figure 75 at z = 0 [m] is due to the different boundary condition types used at the core inlet. As discussed in Section 2.5.1, the single-solve approach applies pressure and temperature boundary conditions and therefore allows for flow reversing. However, the domain-overlapping method applies velocity and temperature boundary conditions, which do not allow for flow reversing. The different boundary condition setups and local flow reversing cause the differences observed in Figure 75. The differences in temperature at z = 6.7 [m] in Figures 73 and 74 occur at the annulus outlet of the core. As observed in the results, flow reversing also takes place at this outlet. The more obvious temperature difference could be an outcome of small localized differences in the flow reversing pattern.

Figure 76 compares the fluidic diode mass flow rates for the first 1000 seconds of the PLOFC transient. The deviation between the two approaches becomes larger after $\sim$ 600 seconds and the oscillation appears in the domain-overlapping results. This indicates that the domain overlapping may experience difficulty when the driving force—in this case, the buoyancy force—becomes weak in comparison to other momentum source terms, such as hydrostatic pressure difference. It is noted that, in the current domain-overlapping approach, both momentum source terms (including the true friction force, buoyancy, and hydrostatic pressure difference) were lumped together to compute an effective frictional coefficient used in the surrogate model. Due to the large difference between those terms, the domain-overlapping approach may suffer from loss of accuracy. This requires further improvements to the methodology in future work.

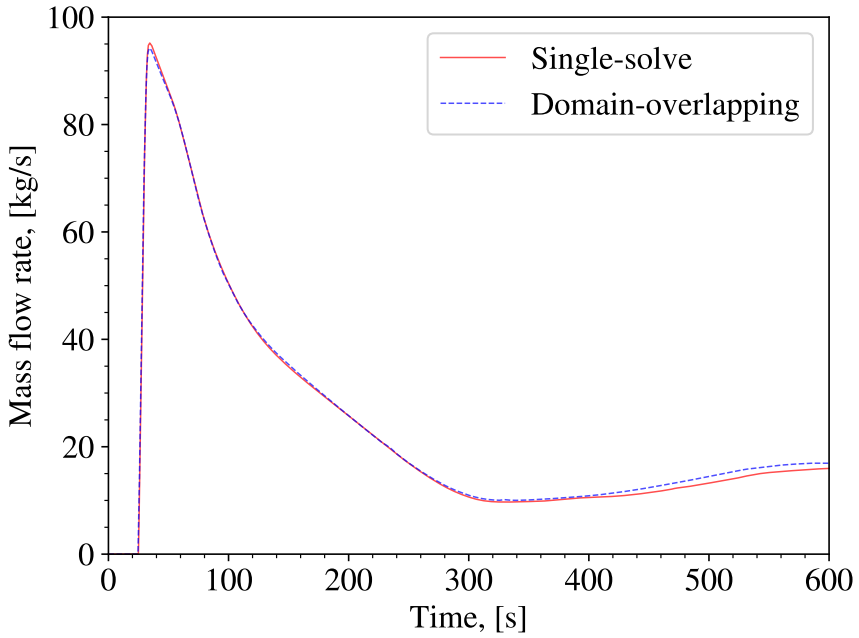

Figure 69. Comparison of mass flow rates through the fluidic diode for the first 600 seconds when using the domain-overlapping and single-solve approaches.

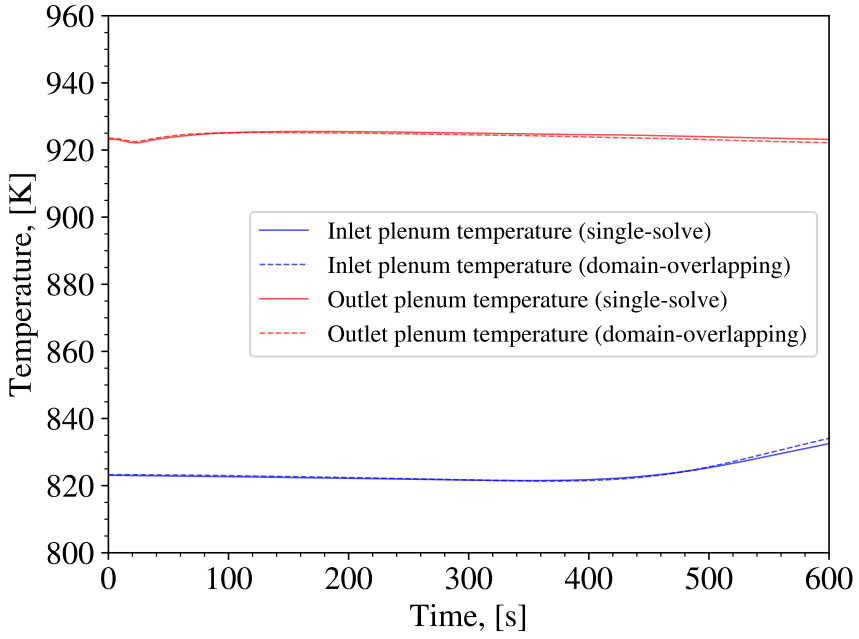

Figure 70. Comparison of inlet/outlet plena temperatures when using the domain-overlapping and single-solve approaches.

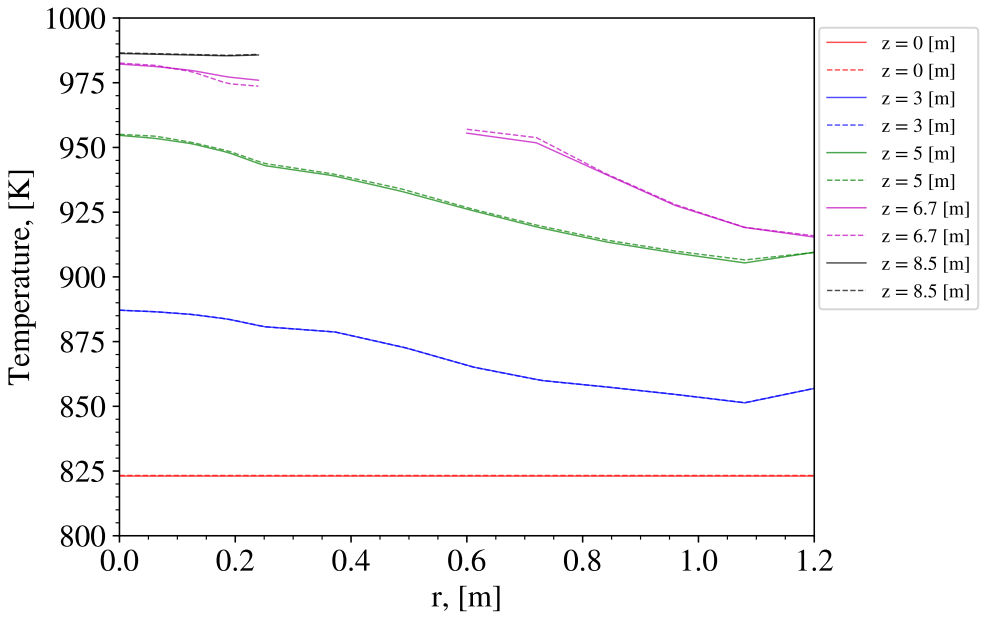

Figure 71. Comparison of fluid temperatures at different vertical locations when using the domain-overlapping (dashed lines) and single-solve (solid lines) approaches at time $\sim$ = 10 seconds.

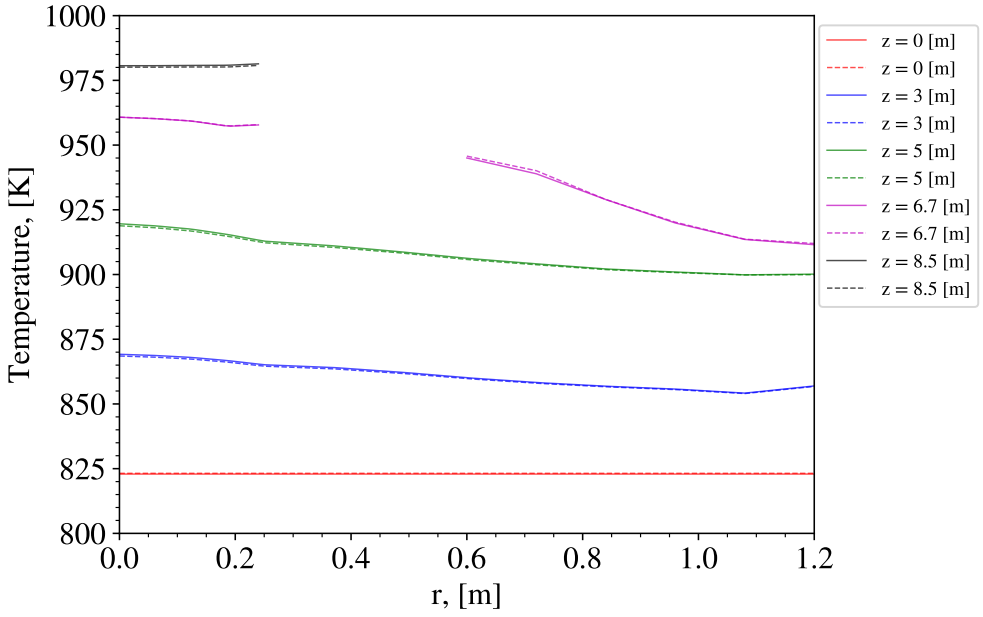

Figure 72. Comparison of fluid temperatures at different vertical locations when using the domain-overlapping (dashed lines) and single-solve (solid lines) approaches at time $\sim$ = 50 seconds.

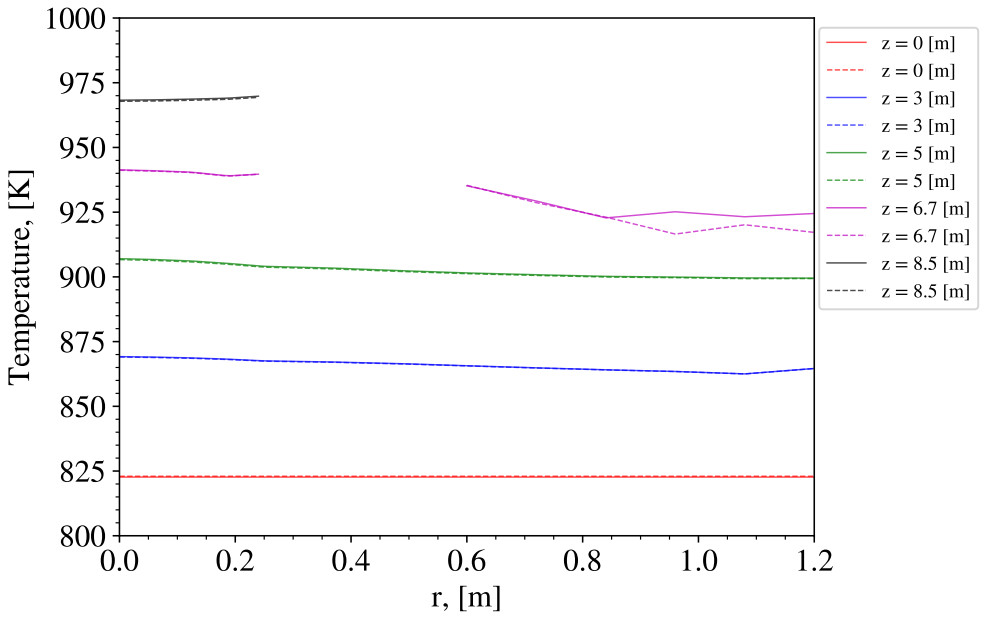

Figure 73. Comparison of fluid temperatures at different vertical locations when using the domain-overlapping (dashed lines) and single-solve (solid lines) approaches at time $\sim$ = 100 seconds.

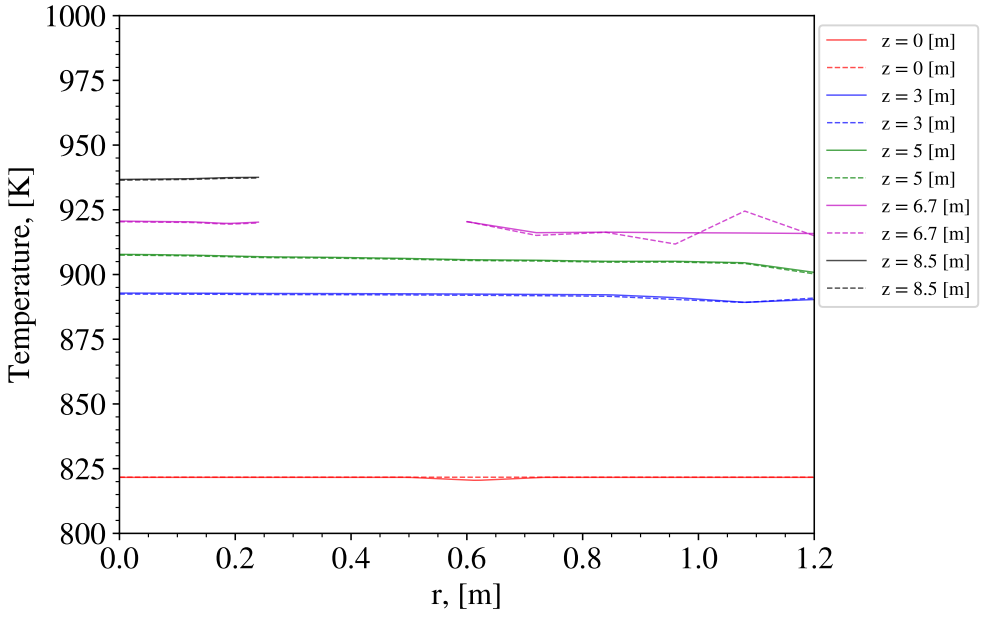

Figure 74. Comparison of fluid temperatures at different vertical locations when using the domain-overlapping (dashed lines) and single-solve (solid lines) approaches at time $\sim$ = 300 seconds.

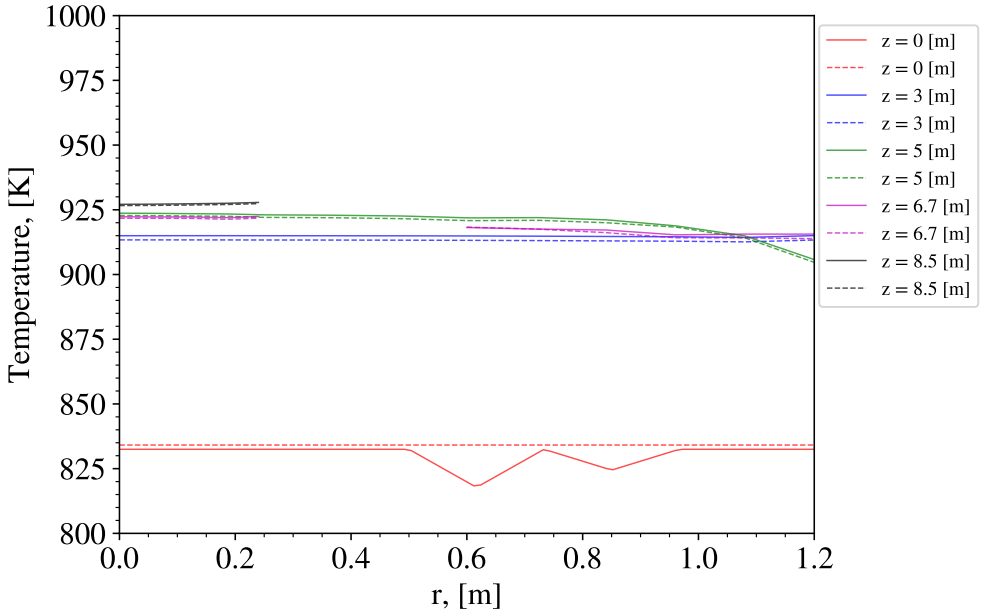

Figure 75. Comparison of fluid temperatures at different vertical locations when using the domain-overlapping (dashed lines) and single-solve (solid lines) approaches at time $\sim$ = 600 seconds.

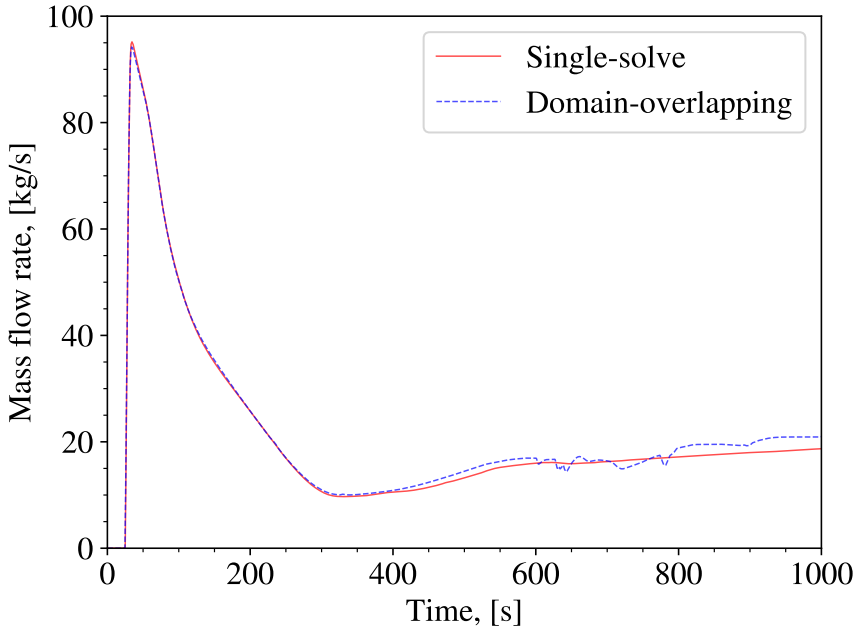

Figure 76. Comparison of mass flow rate through the flow diode for the first 1000 seconds when using the domain-overlapping and single-solve approaches.

3.3. Unprotected Loss-of-Forced-Circulation Scenario

3.3.1. SAM/Griffin/SAM Results

For this section, the unprotected loss Of forced circulation (ULOFC) transient was simulated using the coupled SAM/Griffin/SAM model. The single-solve approach was employed for the 2-D SAM/1-D SAM fluid-fluid coupling. The coupled transient simulation was first restarted from the steady-state results of the coupled SAM/Griffin/SAM steady state model. Then the coupled SAM/Griffin/SAM transient simulation was performed for 5000 s. At t = 5000 s, when the total power primarily stemmed from decay heat, the coupled SAM/Griffin simulation was terminated, and a SAM standalone calculation was restarted from the results of the coupled calculation at t = 5000 s, with only decay heat being applied thereafter to accelerate the transient analysis.

At the beginning of the transient, primary and secondary pump trip was assumed to occur at t = 0 s, and the pump head decreased as shown in Figure 6. Unlike in the PLOFC transient, no reactivity control mechanisms were activated for shutting down the reactor during the ULOFC transient. The control rod position remains at the steady-state position during the transient, and the reactor relies on its internal reactivity feedback mechanisms to reach an approximate shutdown state. The evolution of the core inlet flow rate from the SAM simulation is presented in Figure 77. The decreased pump head at the beginning of the transient decreased the flow rate in the primary loop. The fluidic diode opened shortly after the primary pump was tripped, at around 25 s into the transient. A flow path for natural circulation between the hot core region and cold downcomer region was then established through the fluidic diode. During the ULOFC transient, a natural circulation flow corresponding to $\sim 2.8\%$ of the steady state inlet flow rate was established. The total, prompt, and decay power evolution during the first 5000 s of ULOFC transient are illustrated in Figure 78(a). As the inlet flow rate decreased, the core temperature increased, in turn leading to a negative thermal feedback and causing a reduction in reactor power. At t = 5000 s, the prompt power dropped to approximately 0.035% of the steady-state level. The decay power decreased from 19.6 to 3.4 MW at 5000 s. Figure 78(b) shows the decay heat and heat removal by the RCCS beyond t = 5000 s. As the decay heat continued to decrease while heat removal by the RCCS continued to increase, eventually (at approximately t = 35,000 s) the RCCS heat removal rate exceeded the decay heat. After this time, the reactor slowly cooled down and the amount of heat rejected to the RCCS began to decline.

Figure 79 presents the core peak fuel kernel and peak pebble temperatures reached during the ULOFC transient. At the beginning of the transient, the core peak fuel kernel and pebble temperatures increased due to rapid reduction in coolant flow. Then the peak fuel kernel and pebble temperatures started to decrease after t = 25 s. They increased again as the RCCS heat removal was initially lower than the decay heat. After ~ 50000 s, the peak fuel kernel and pebble temperatures started to decrease as the RCCS heat removal became sufficient to cool the core. Figure 80 presents the core inlet, core outlet, and vessel outer surface average temperatures reached during ULOFC transient. As in the PLOFC transient, oscillatory behavior was observed in both the RCCS heat removal and core temperatures, indicating the presence of flow oscillations in the natural circulation loop during the transient. A closer look at these oscillations is provided in Figure 81, which zooms in on the inlet velocity and the core inlet, core outlet, and vessel outer surface average temperatures at the oscillation region. The oscillation period was approximately 500 s, indicating that this oscillation phenomenon was physical rather than numerical in nature. In a real PB-FHR design, there may not be oscillations in the natural circulation flow during ULOFC, depending on the actual primary loop and RCCS designs.

Figures 82 and 83 illustrate the evolution of the fluid temperature distributions and axial velocity distributions during the ULOFC transient, respectively. At around t = 1000 s, in-core circulations were observed at the core bottom and top. These recirculation patterns dissipated at later times, and the flow became predominantly axial. Figure 84 shows the axial and radial profiles of the fluid temperature at peak

fuel temperature (t = 49,116 s). At r = 0.15 m, the fluid temperature increased from the core inlet. After the flow entered the defueling chute, the temperature remained nearly constant due to the minimal power deposition in that region. At r = 0.92 m, the fluid temperature remained constant through the inlet annulus region and began to increase from the lower cone region. In the core upper region, the fluid temperatures at r = 0.15 m and r = 0.92 m were nearly identical. That is also shown in Figure 83, with the radial temperature distributions being nearly flat at z = 3.605 m and z = 5 m.

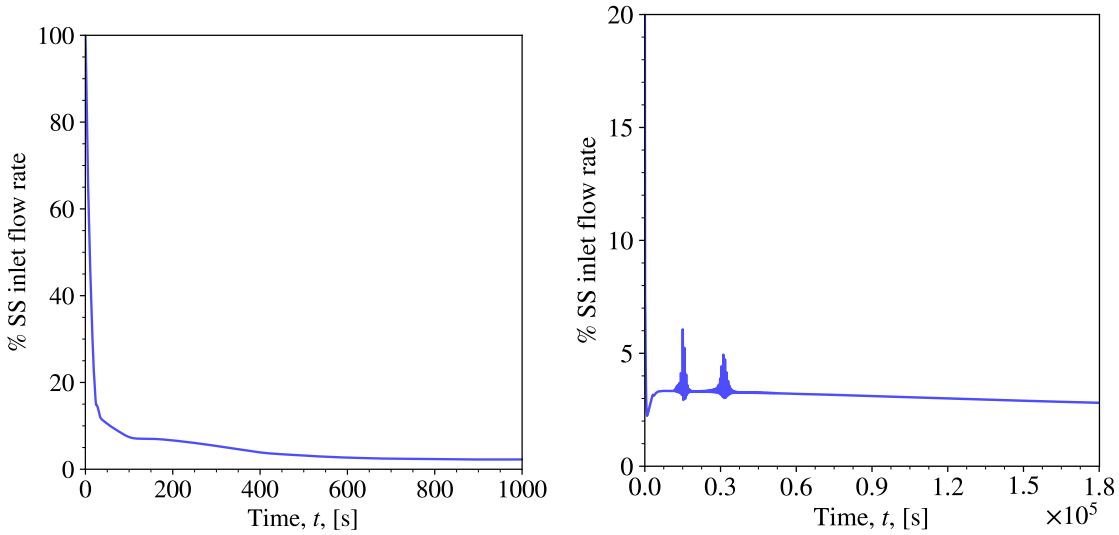

(a) Before 1000 s

(b) Whole transient

Figure 77. Core inlet velocity of SAM/Griffin/SAM during the ULOFC transient.

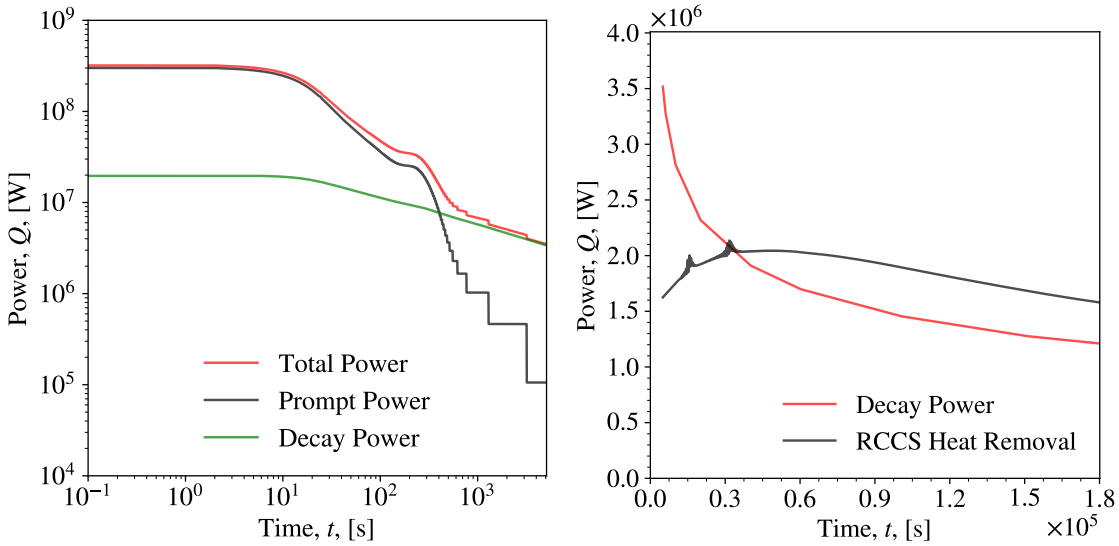

(a) Power before 5000 s

(b) Decay heat and RCCS heat removal rate after 5000 s

Figure 78. Power before 5000 s, and decay power and RCCS heat removal rate after 5000 s, from SAM/Griffin/SAM during the ULOFC transient.

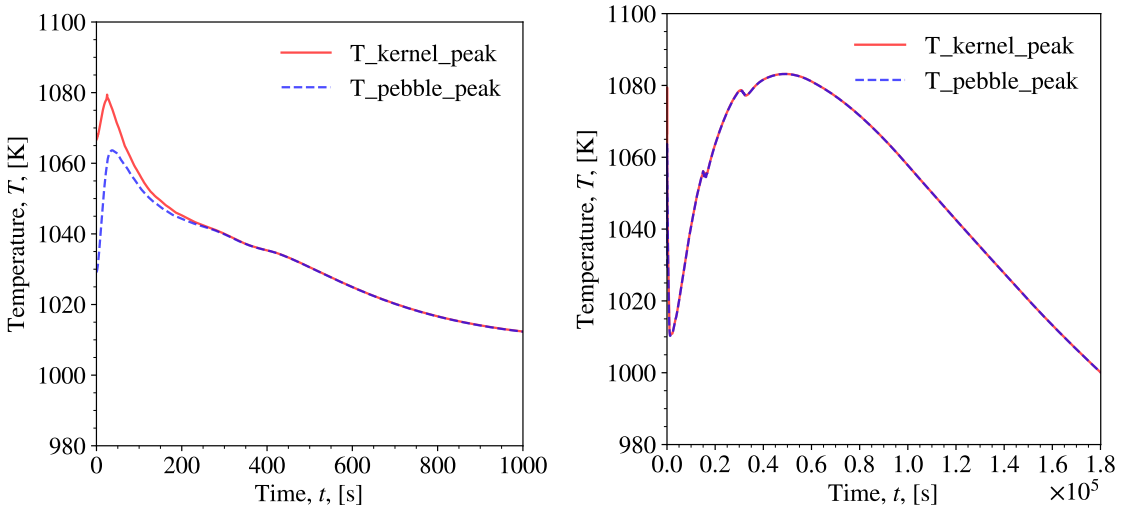

(a) Before 1000 s (b) Whole transient

Figure 79. Peak pebble and fuel kernel temperature from the coupled SAM/Griffin/SAM calculation during the ULOFC transient.

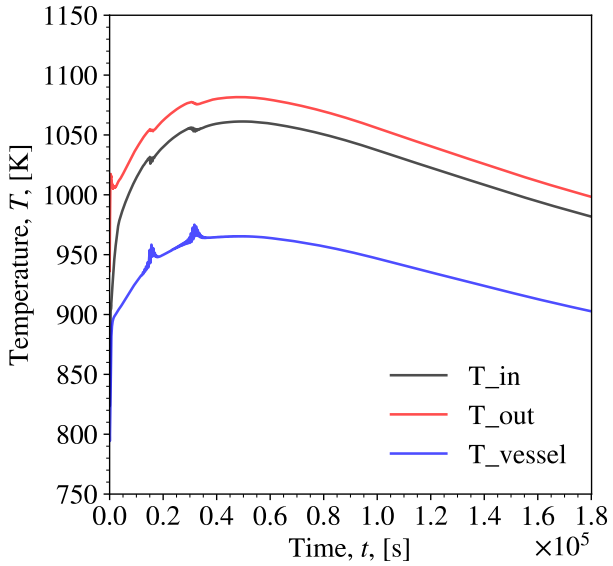

Figure 80. Core inlet, outlet, and vessel outer surface temperature from coupled SAM/Griffin/SAM calculation during the ULOFC transient.

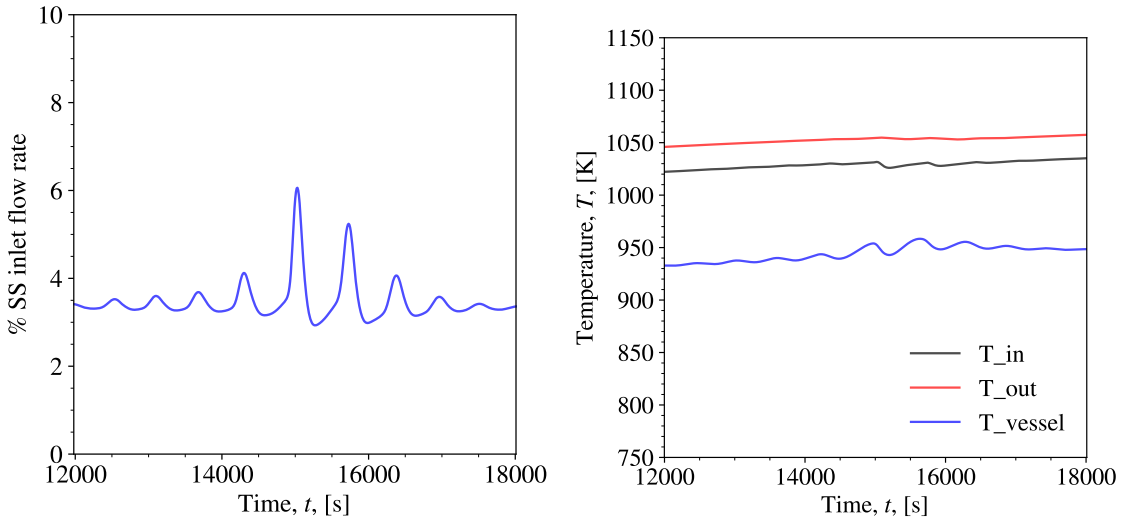

(a) Inlet velocity (b) Core inlet, outlet, and vessel outer surface T

Figure 81. Inlet velocity and the core inlet, outlet, and vessel outer surface temperature from the coupled SAM/Griffin/SAM calculation at the oscillation region during the ULOFC transient.

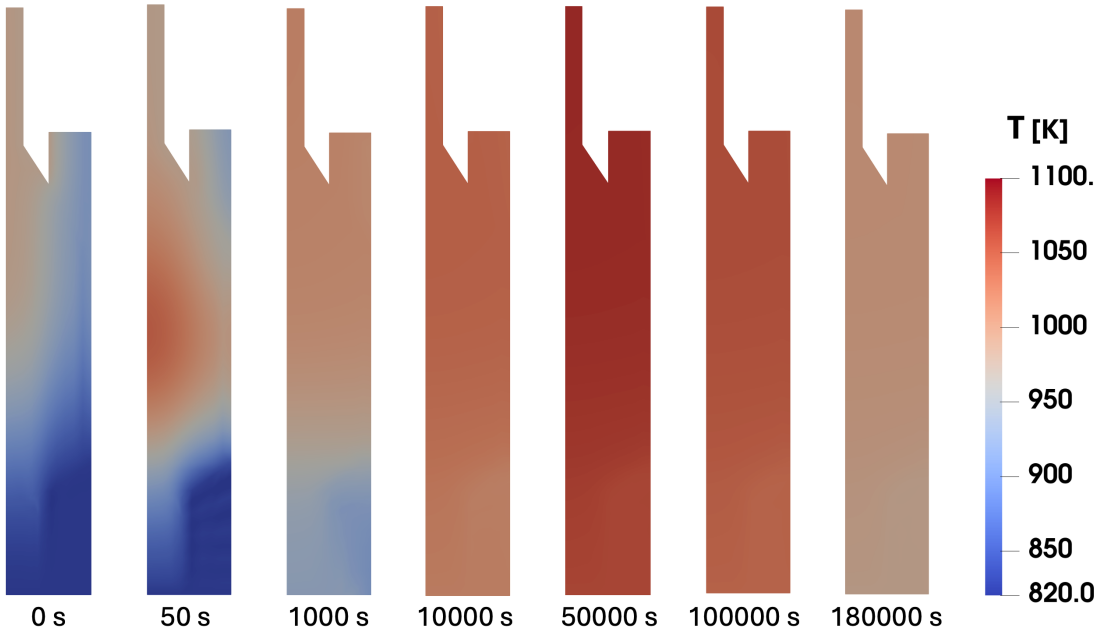

Figure 82. Fluid temperature distributions from coupled SAM/Griffin/SAM during ULOFC

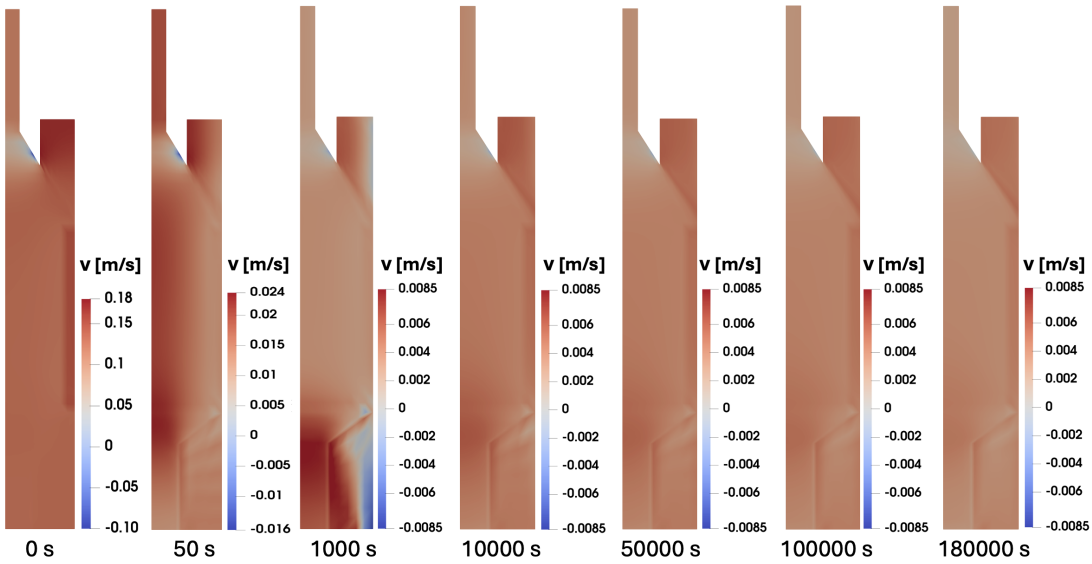

Figure 83. Axial velocity distributions from the coupled SAM/Griffin/SAM during the ULOFC transient.

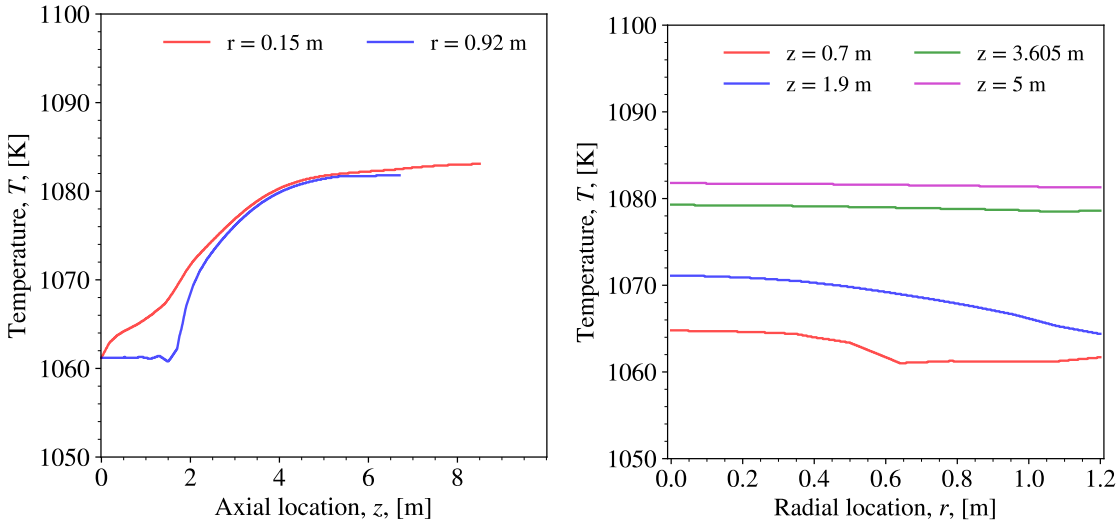

(a) Axial distributions

(b) Radial distributions

Figure 84. Axial and radial fluid temperature distributions from the coupled SAM/Griffin/SAM during the ULOFC transient at peak pebble/TRISO-kernel temperatures (t = 49, 116 s).

3.3.2. SAM/PKE/SAM Results

For this section, the ULOFC transient was simulated using the SAM/PKE/SAM model. The single-solve approach was utilized in the 2-D SAM/1-D SAM fluid coupling. The SAM/PKE/SAM simulation was restarted from the coupled SAM/Griffin/SAM steady-state results to ensure accurate initial conditions, including the spatial power distribution.

Figure 85 compares the power evolution predicted by coupled SAM/Griffin/SAM and SAM/PKE/SAM calculations during the ULOFC transient. Both simulations show a monotonic decrease in power; however, differences are observed in the rate of power reduction. At the early stage of the transient, the SAM/PKE/SAM model predicted a slower drop in power as compared to the SAM/Griffin/SAM results. After approximately 45 s, the SAM/PKE/SAM model exhibited a more rapid power decrease than the SAM/Griffin/SAM simulation. Figure 86 compares the peak fuel kernel and pebble temperature from the coupled SAM/Griffin/SAM and SAM/PKE/SAM calculations during first 1000 s and over the entire transient period. The peak fuel kernel and pebble temperatures from SAM/PKE/SAM show a similar trend when compared with the results from coupled SAM/Griffin/SAM. However, SAM/PKE/SAM predicted a higher initial peak fuel kernel temperature of 1088.0 K at t = 26 s, as compared to 1079.4 K from the SAM/Griffin/SAM model. This is due to SAM/PKE/SAM predicting a higher power than did coupled SAM/Griffin/SAM at the beginning of the transient, as shown in Figure 87, which indicates a higher power density throughout most of the pebble-bed region at t = 26 s. At around t = 50,000 s, the SAM/Griffin/SAM model predicted a higher peak fuel kernel value of 1083.2 K, while SAM/PKE/SAM gave a slightly lower value of 1075.6 K. Toward the later stage of the ULOFC transient, the peak fuel kernel and pebble temperatures from both models converged. Overall, SAM/PKE/SAM gave a higher maximum value of peak fuel kernel temperature than did the coupled SAM/Griffin/SAM. The time at which this maximum occurred also differed: in the initial peak at t = 26 s for SAM/PKE/SAM, and in the long term rise at t = 49,116 s for SAM/Griffin/SAM. Figure 88 compares the core inlet, outlet, and vessel wall outer surface average temperatures predicted by the coupled SAM/Griffin/SAM and SAM/PKE/SAM calculations. The trend in the SAM/PKE/SAM results is similar to that seen in the coupled SAM/Griffin/SAM results. The SAM/PKE/SAM results show lower maximum inlet, outlet, and vessel wall average temperatures during the transient. In the later stage of the simulation, the temperature predictions from both models converged and showed good agreement.

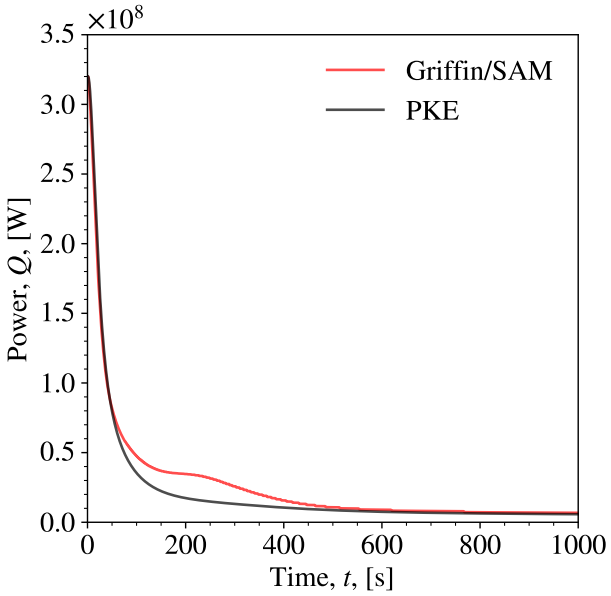

Figure 85. Power predicted by SAM/Griffin/SAM and SAM/PKE/SAM during the ULOFC transient.

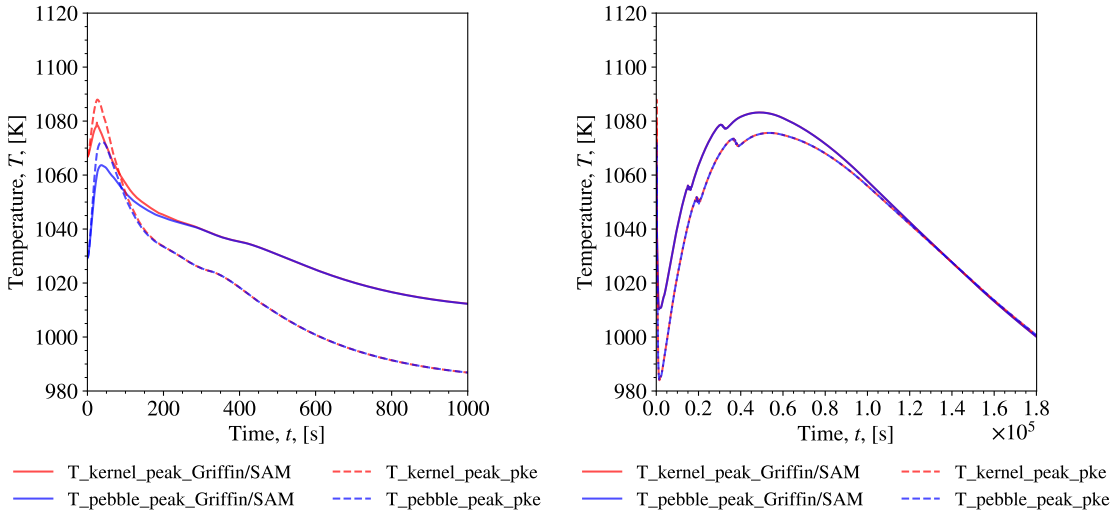

(a) Before 1000 s

(b) Whole transient

Figure 86. Peak pebble and fuel kernel temperature from the coupled SAM/Griffin/SAM and SAM/PKE/SAM calculations during the ULOFC transient.

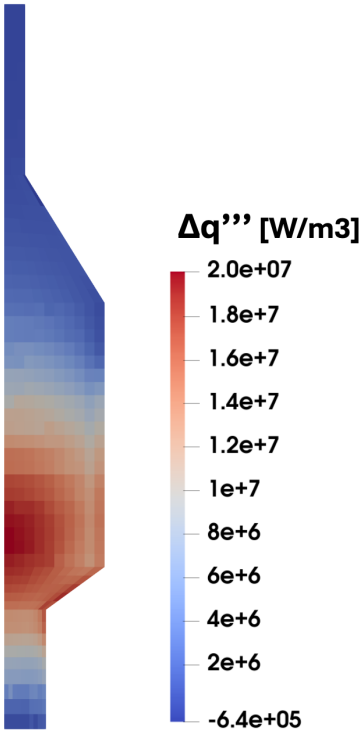

Figure 87. Power density difference (SAM/PKE/SAM - SAM/Griffin/SAM) predicted by SAM/Griffin/SAM and SAM/PKE/SAM at 26 s into the ULOFC transient.

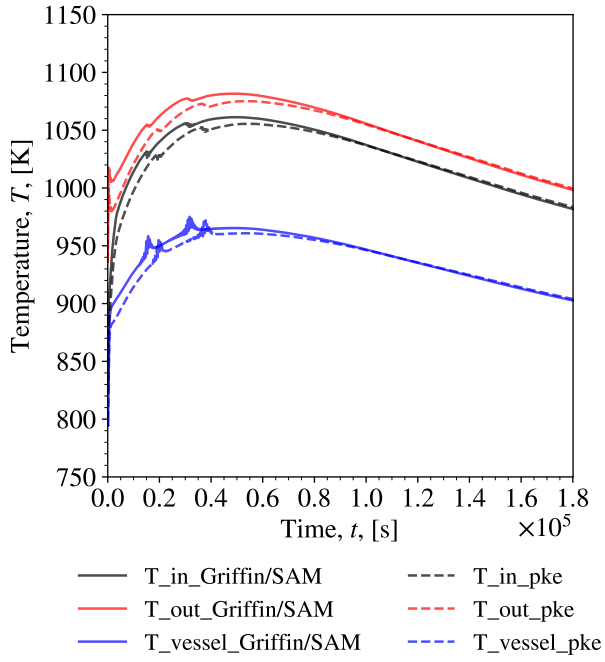

Figure 88. Core inlet, outlet, and vessel outer surface temperature from the coupled SAM/Griffin/SAM and SAM/PKE/SAM calculations during the ULOFC transient.

3.3.3. SAM/PKE/SAM Sensitivity Demonstration

Dakota [54], an optimization and uncertainty quantification analysis code developed by Sandia National Laboratories, is of interest to support sensitivity and uncertainty studies. Dakota has the flexibility to support these types of analysis with any desired simulation code via black-box interfaces. In this structure, Dakota supplies parameter values (e.g., steps in a parameter study or sets of random samples from input distributions), then receives response values back for summary and statistical processing, with no knowledge of the simulation code or underlying physics. The functions of preprocessing Dakota-supplied parameters for a simulation code, executing the simulation, and post-processing/returning responses to Dakota can be accomplished by analysis driver scripts. An analysis driver script was previously developed to interface Dakota with the SAM code [55], and was modified in this work to demonstrate the application of Dakota to support analyses within the BlueCRAB framework. Within this scope, a basic parameter sensitivity study was carried out using the SAM-standalone PKE ULOFC transient model with a version of SAM built within the BlueCRAB code suite.

Figure 89 shows transient curves used in a parameter study that investigated the SAM-standalone PKE model maximum fuel temperature's sensitivity to variations in the transient pump head and decay heat. The initial pump head was maintained in each case, with perturbations applied to the coastdown rate (via pump head half-life). For the decay heat cases, the initial power level was maintained in each perturbed case, while the fraction of decay heat at the initial state and decay heat levels during the transient ranged from 80% to 120% of the nominal values.

Each perturbed version of the model was generated and executed by Dakota in parallel to similar studies on other input parameters. Maximum fuel temperatures and the peak values achieved by each of these curves during the first 1000 s of the ULOFC transient are shown in Figures 90 and 91 for the pump head and decay heat cases, respectively.

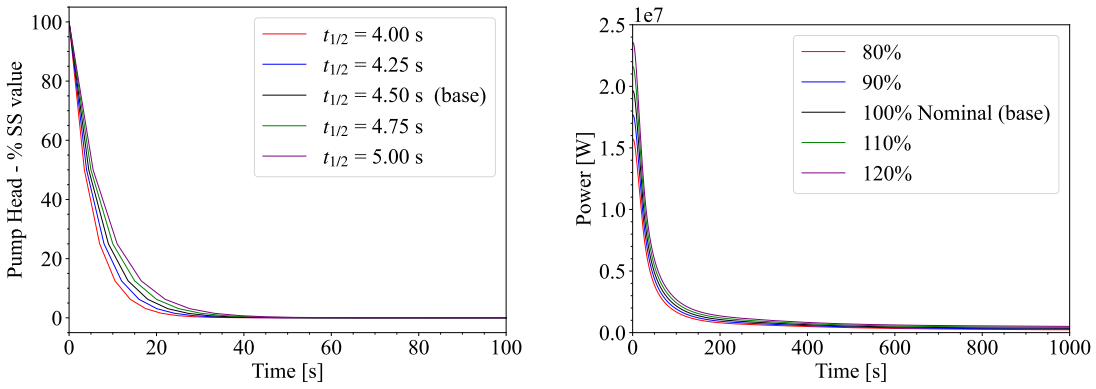

(a) Pump Head

(b) Decay Heat

Figure 89. Parameter study input curves from Dakota for the SAM-standalone PKE model during the ULOFC transient.

Additional studies can be carried out with any parameter accessible through the model inputs, including, for example, reactivity coefficients, material properties, boundary conditions, and built-in sensitivity coefficients for correlations. Beyond assessing the sensitivity to individual parameters as demonstrated here, Dakota provides other methods such as multi-variate sensitivity analysis and uncertainty propagation using random sampling. These other analysis methods can be applied by using the same analysis driver scripts, without further modification.

Future work in this area may further explore and demonstrate practical applications of interfacing with Dakota, as well as the generalization of interface scripts for other codes in the BlueCRAB suite. The long-term

goal of this effort is to provide analysts with a framework that can support diverse BlueCRAB analyses, ranging from individual parameter sensitivity studies to multiphysics uncertainty propagation.

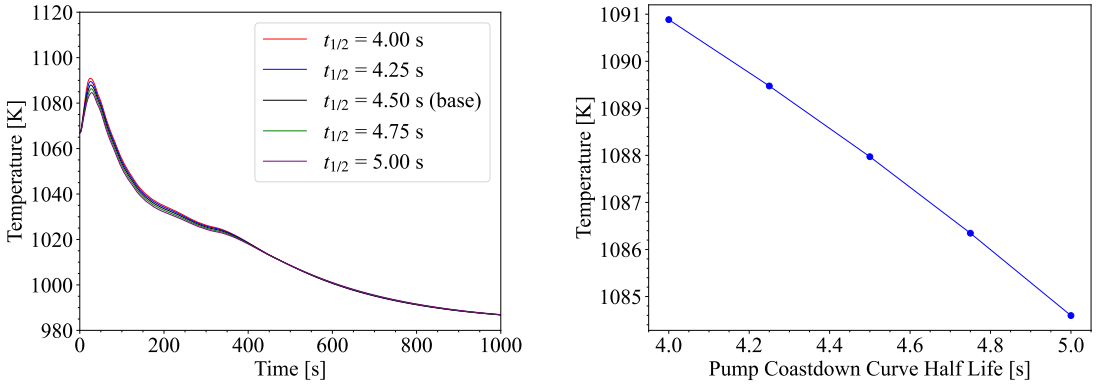

(a) Before 1000 s (b) Peak Value

Figure 90. Maximum fuel temperatures for a parameter study of the pump coastdown curve, using the Dakota/SAM-standalone PKE model during the ULOFC transient.

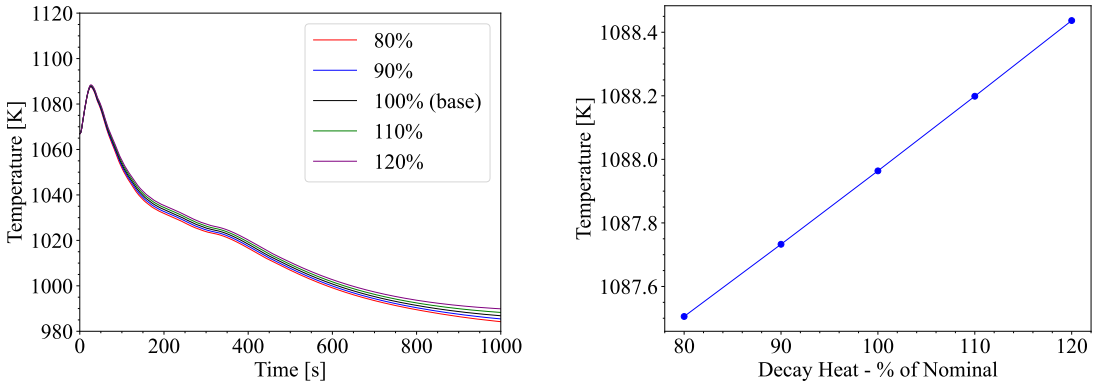

(a) Before 1000 s (b) Peak Value

Figure 91. Maximum fuel temperatures for a parameter study on decay heat when using the Dakota/SAM-standalone PKE model during the ULOFC transient.

3.3.4. 2-D Pronghorn/Griffin Results

For this section, the ULOFC transient was simulated with the coupled Pronghorn/Griffin model. As was the case with the PLOFC transient, this model consists of the core, reflector, plena, diode, and downcomer in the 2-D R-Z Pronghorn model. During the transient, the outlet of the core and the inlet of the downcomer were replaced with walls, as this flow was assumed to be negligible compared to the mass flow rate of the circulation through the diode. The diode in the Pronghorn model was initially closed during the steady-state simulation. This was accomplished through the use of "hydraulic separators" in Pronghorn, which essentially isolated the fluid in the diode from the rest of the domain. These separators were removed during the transient, opening the diode and allowing flow to pass through. The prompt fission and decay heat power was computed in Griffin.

Figures 92 and 93 show the axial velocity and fluid temperature at several snapshots during the ULOFC transient. The flow path of the fluid is very similar to that observed in the PLOFC transient, with the primary flow passing through the diode and descending in the downcomer, while smaller recirculation regions are present near the reflector walls. In Figure 93, opening of the diode at around t = 50 s is once again visible, as the fluid begins to pass through the diode and into the downcomer. Additionally, it can be seen from this figure how the hotspot in the fluid temperature tends to shift as the transient progresses. Initially, the fluid is hottest in the top-center of the core. The hotspot briefly shifts downward at the start of the transient toward the region of highest power generation, due to the loss of flow. As flow is reestablished through the diode at t = 1000 s, the hotspot again shifts upward, and remains toward the top of the core as hot fluid advects upward due to buoyancy.

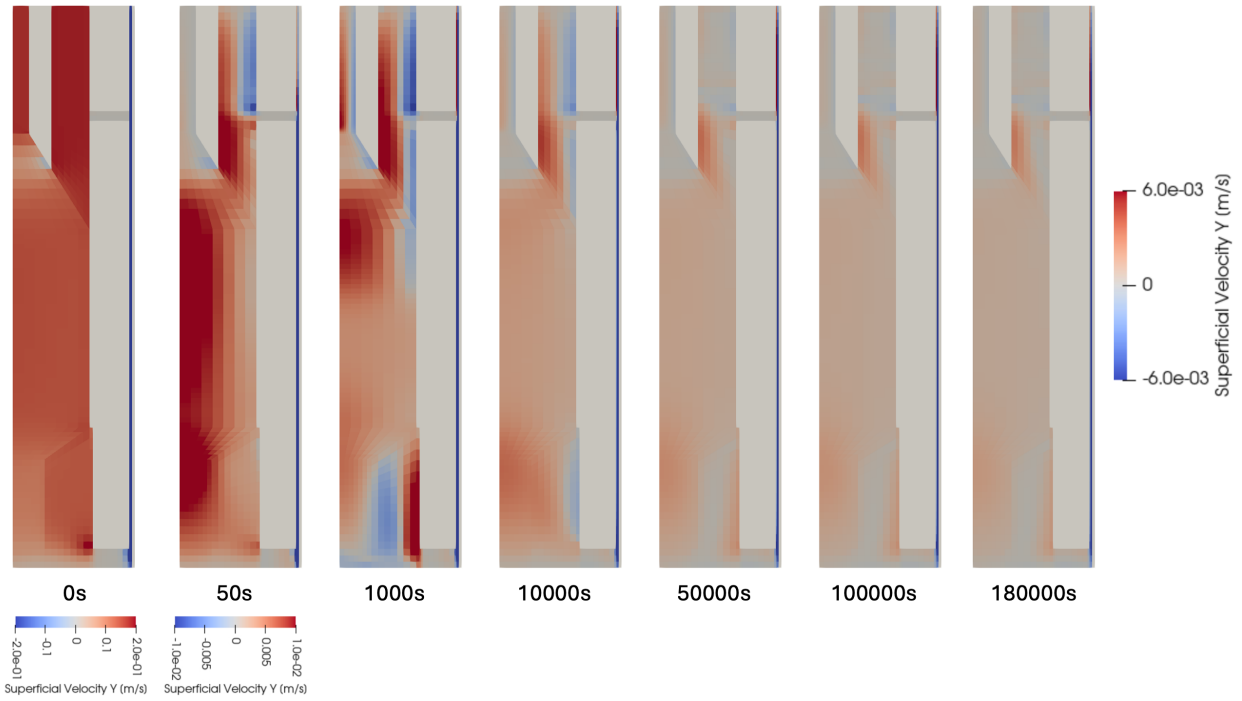

Figure 92. Superficial velocity in the y-direction at several instances during the ULOFC transient, with Pronghorn/Griffin coupling. Note that the plots for t = 0 s and t = 50 s use a different scale than the rest of the plots.

The mass flow rate through the diode is shown in Figure 94. Immediately upon opening, the diode mass flow rate peaks at around 100 kg/s. The lack of reactor shutdown in this transient means that the core power is higher when the diode opens (compared to the PLOFC transient), and this extra power is reflected in the higher diode mass flow rate as compared to the PLOFC transient. The flow through the diode then continues to steadily decrease as the core power rapidly drops during this time, where it falls to around 2%–3% of the steady-state mass flow rate. There is a short period of relatively constant mass flow rate through the diode as heat propagates through the solid structures of the core. As the decay power continues to slowly decrease, so does the natural circulation mass flow rate.

The core maximum and average graphite temperatures, along with the reactor pressure vessel temperature during the ULOFC transient, are shown in Figure 95. The average and maximum temperatures initially peak as the flow rate in the core quickly decreases. Because no reactor shutdown is used in this transient, the core power is still relatively high, leading to a rapid increase in core graphite temperatures. This temperature increase leads to power feedback, reducing the core power. Eventually, a steady flow rate through the diode

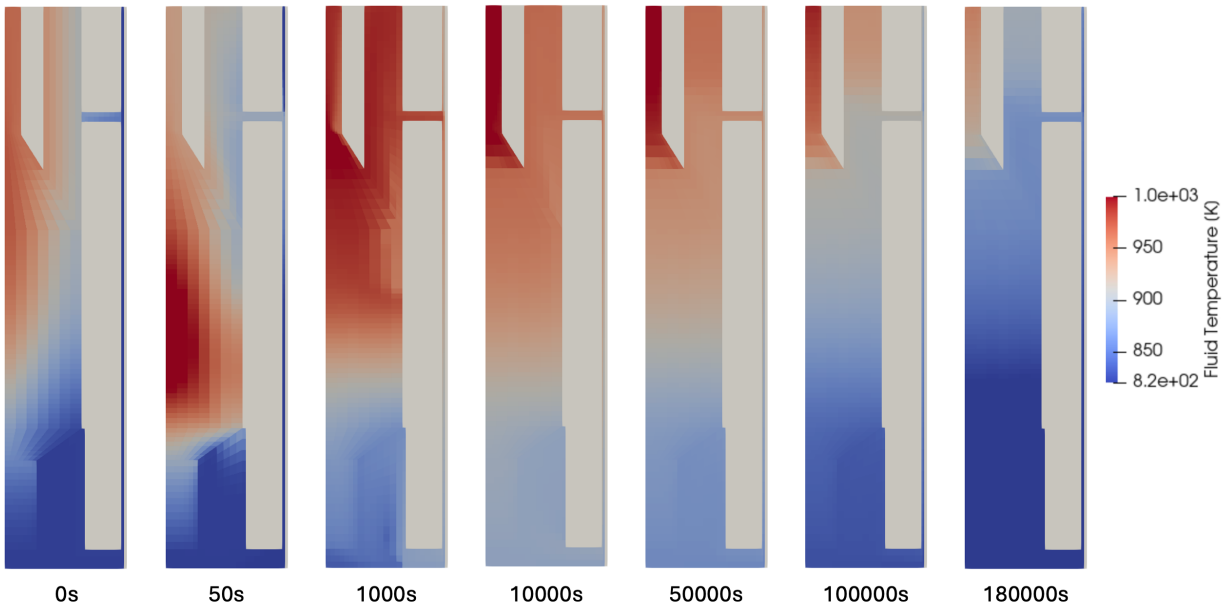

Figure 93. FLiBe temperature at several instances during the ULOFC transient, with Pronghorn/Griffin coupling.

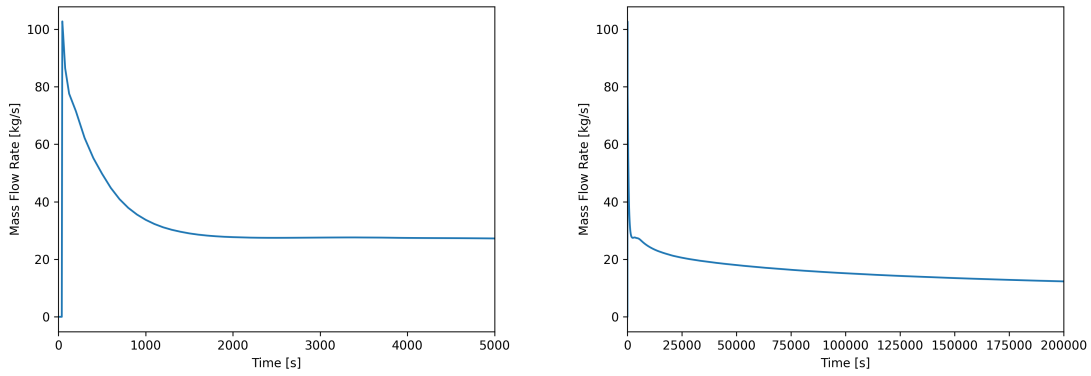

(a) First 5000s

(b) Whole Transient

Figure 94. Mass flow rate through the fluidic diode during the ULOFC transient, with Pronghorn/Griffin coupling.

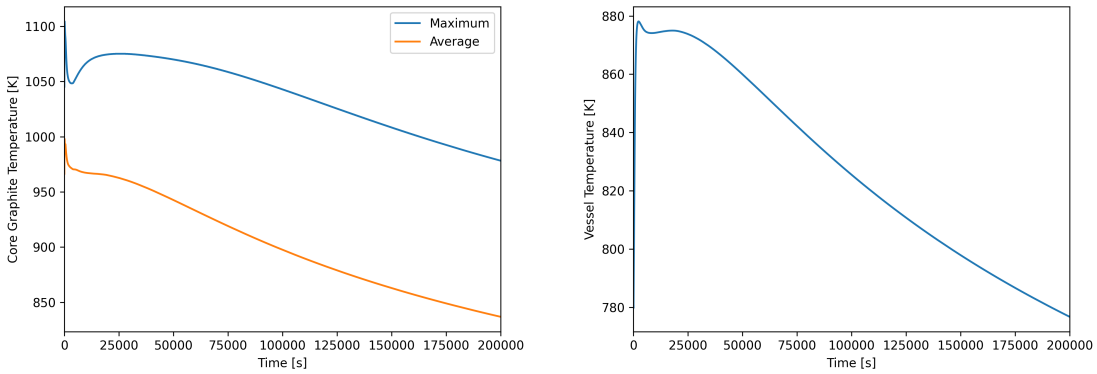

(a) Core graphite (b) Vessel

Figure 95. Core graphite and vessel temperatures during the ULOFC transient, with Pronghorn/Griffin coupling.

is established, and heat can be effectively removed from the core. The maximum fuel temperatures peak at around 1100 K during the initial loss of flow. A second peak at around 1080 K occurs in the fuel temperature maximum at around t = 25,000 s as heat is slowly transferred through the structural components. The core average temperature tends to decrease more steadily throughout the transient. The vessel follows a similar but slightly different trend. It too has a double-peaked shape, though the first peak occurs later than it did for the core graphite, as additional time is required for the core graphite temperature to propagate out to the vessel.

3.3.5. Comparison of SAM/Griffin/SAM and Pronghorn/Griffin Results

In the analysis of the ULOFC scenario, both SAM/Griffin/SAM and Pronghorn/Griffin predicted that the reactor would reach a near-shutdown state during the transient with internal reactivity feedback mechanisms. As illustrated in Figure 96, the two simulations exhibited similar trends in reactor power. However, due to different modeling assumptions on the primary loop, pump coastdown, and RCCS models, the power and temperatures from the two simulations show noticeable differences. The downcomer mass flow rates from the two simulations are shown in Figure 97. In the SAM/Griffin/SAM simulation, pump coastdown was modeled by reducing the pump head in accordance with an exponential decay function within the SAM 1-D system model. In contrast, the Pronghorn/Griffin simulation does not account for pump coastdown, as it is not coupled to the SAM 1-D system model. Instead, in the Pronghorn model, the core outlet and downcomer inlet boundaries were set to wall boundary conditions at the beginning of the transient. A fluid diode was opened at a later time to establish a natural circulation flow path. This modeling difference lowered the mass flow rate and thus reduced the heat removal from the core for approximately the first 300 seconds of the transient in the Pronghorn/Griffin simulation. Consequently, a more rapid decrease in reactor power was observed, as shown in Figure 96. Figure 96(b) presents the vessel wall temperature evolutions during the ULOFC transient. The vessel temperature predicted by Pronghorn/Griffin is lower than the value reflected in the SAM/Griffin/SAM results. This is due to the RCCS modeling being handled differently by the two models. The Pronghorn/Griffin simulation does not currently couple with an RCCS loop model, whereas the SAM/Griffin/SAM simulation includes a RCCS loop model in the SAM 1-D system model. This can impact the RCCS panel temperature and thus the radiative heat transfer to the RCCS panels. Additionally, Pronghorn and SAM use slightly different radiative heat transfer models. Pronghorn utilizes an infinite-cylinder radiative heat transfer boundary condition with a fixed sink temperature, whereas SAM models the radiative heat transfer between the reactor vessel wall and water panels with two concentric cylinders. These differences

between the two models will be addressed in future work with the fully coupled Pronghorn/Griffin/SAM simulation once overlapping domain coupling between the Pronghorn 2-D core porous media model and the SAM loop model becomes available.

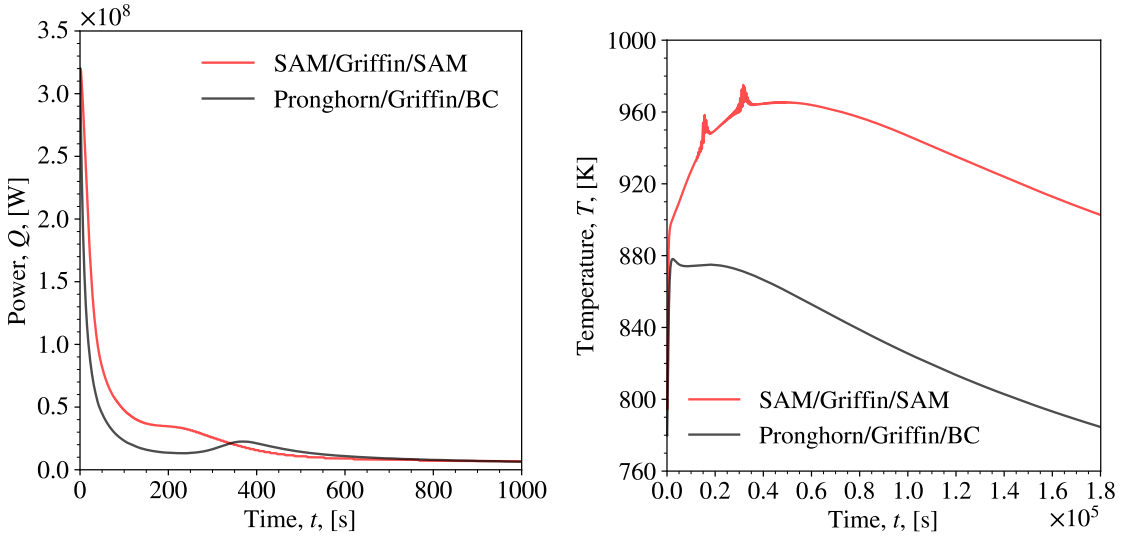

(a) Power

(b) Vessel wall temperature

Figure 96. Power and vessel wall temperatures predicted by SAM/Griffin/SAM and Pronghorn/Griffin/BC during the ULOFC transient.

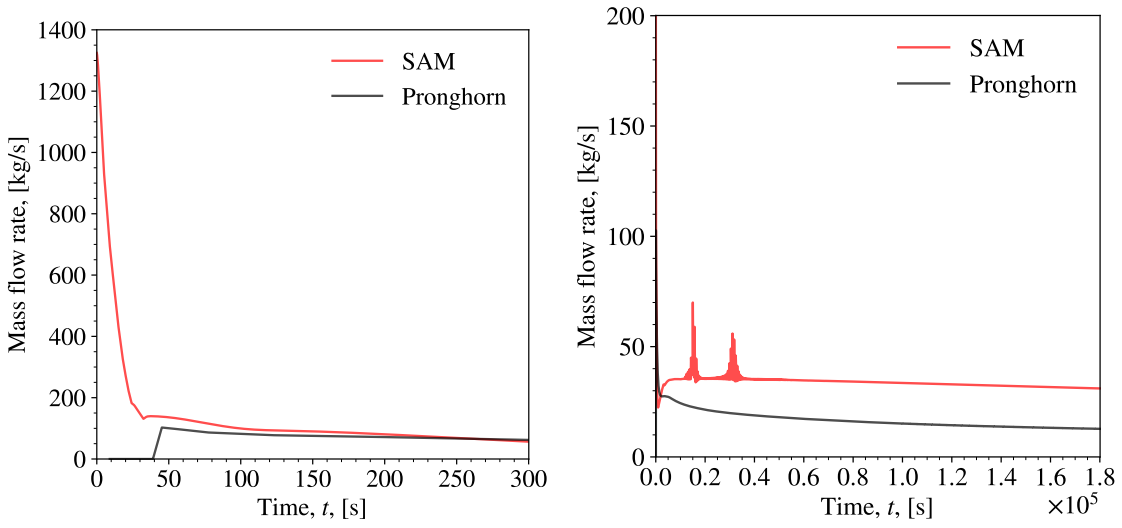

(a) First 300 s

(b) Whole transient

Figure 97. Downcomer mass flow rates from SAM/Griffin/SAM and Pronghorn/Griffin/BC during the ULOFC transient.

3.4. Control Rod Movement Accident Scenarios - 2-D Simulation With Baseline Model

This control rod transient event is similar to the prompt supercritical insertion discussed in Section 3.5.2, but it uses the baseline model to compare the solutions from the Pronghorn/Griffin and SAM/Griffin/SAM models. The most significant difference between the two models lies in the calculation of fuel and moderator temperatures. The Pronghorn/Griffin simulation relies on the explicit 1-D BISON solution for the kernel and pebble temperatures, using the thermophysical properties from Table 20 for each pebble burnup group, whereas SAM uses its multiscale pebble model.

The second difference between the models is the exclusion of the primary system loops in the Pronghorn/Griffin transient results, although the overlapping domain methodology with the SAM loops was used to establish the initial conditions. In contrast, the SAM/Griffin solution relies on the direct-solve coupling methodology as applied to the SAM loops. Therefore, any system coupling effects will be observed in the SAM/Griffin solution, primarily as delayed effects arising from changes to the fluid conditions in the core.

The time evolution of the reactivity from the Pronghorn/Griffin simulation is shown in Figure 98. The time evolution of the power, control rod position, fuel and moderator temperatures, and fluid density are included in Figures 99 to 102.

Upon the withdrawal of the control rod at between 10 and 30 seconds, the dynamic reactivity quickly rises to +35¢, initiating a power escalation from 320 MW_{th} to over 700 MW_{th} within a few seconds. The fuel temperature feedback rapidly counteracts this positive insertion, reversing the power increase and initiating a subsequent decrease. While the moderator temperature and fluid density feedback also contribute, their effects are of a lesser magnitude.

The control rods were driven back to their initial position at between 40 and 42 seconds, inserting additional negative reactivity. The value of -120¢ is likely an overestimation, as such a sharp inflection requires much finer time-stepping. The results indicate that the power peak is 725 MW_{th} for the Pronghorn/Griffin model and 790 MW_{th} for the SAM/Griffin model, which is unsurprising given the differences in fuel temperature modeling. This result illustrates the sensitivity of this type of transient scenario to fuel temperature modeling.

Figure 100 confirms that the initial temperature for the SAM/Griffin model is already higher than that in the Pronghorn/Griffin model. Additionally, the fuel temperature rise during the initial phase of the transient is smaller in the SAM/Griffin model. These two factors result in a smaller fuel temperature feedback in the SAM model, as well as a higher power level.

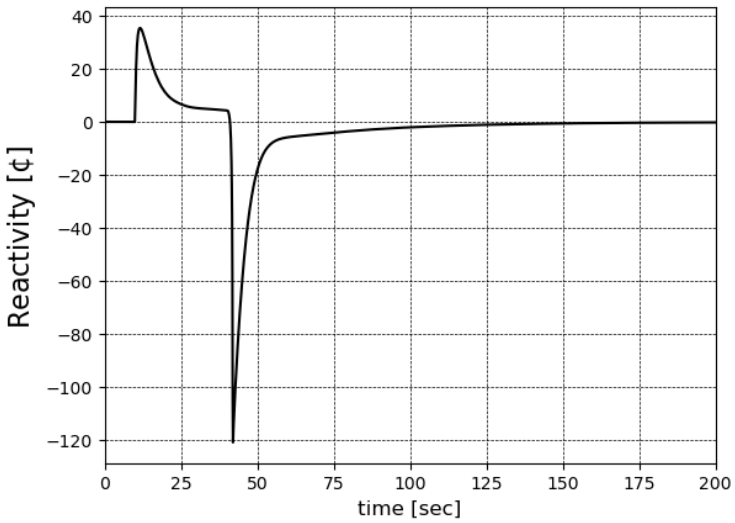

Figure 98. Dynamic reactivity evolution during a prompt supercritical CR withdrawal, obtained with Pronghorn/Griffin.

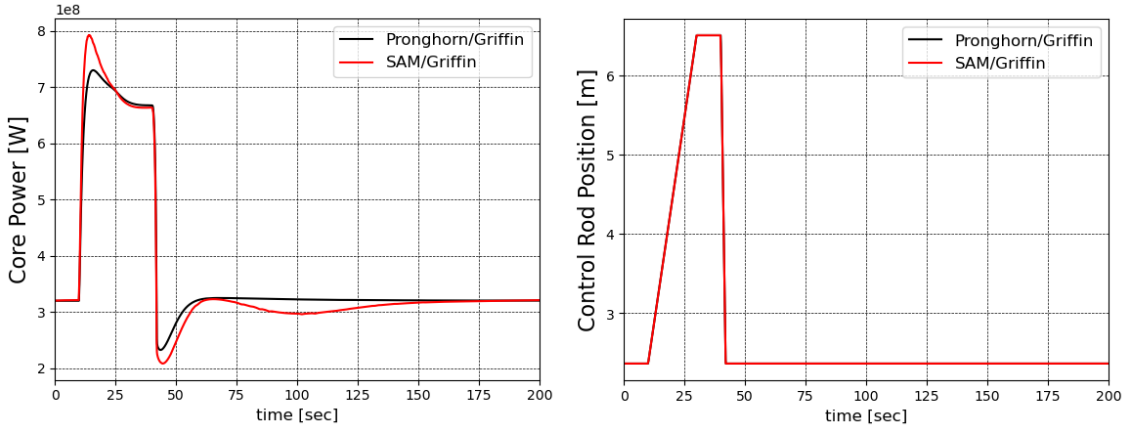

(a) Core power (b) Control rod movement

Figure 99. Comparison between Pronghorn/Griffin and SAM/Griffin in regard to the control rod movement and core power predicted for the control rod movement accident.

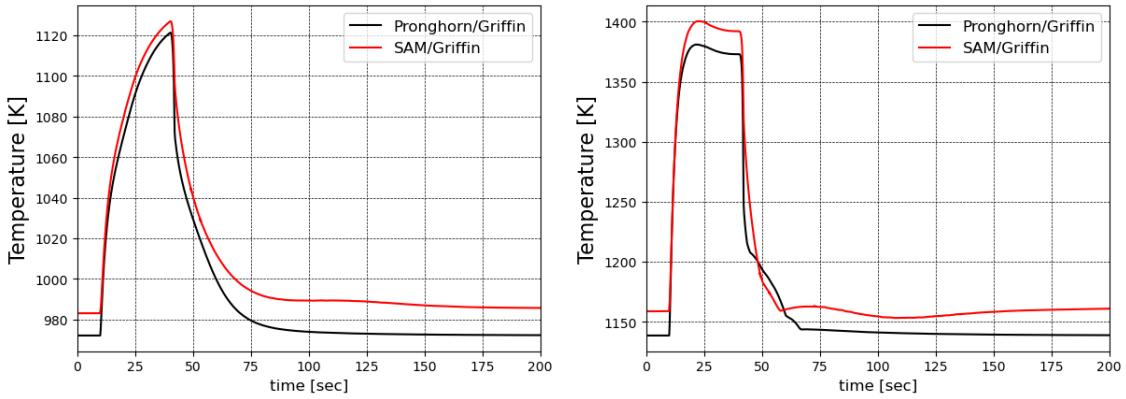

(a) Volume-average (b) Maximum

Figure 100. Comparison between Pronghorn/Griffin and SAM/Griffin in regard to the volume-averaged and maximum fuel temperatures predicted for the control rod movement accident.

The moderator temperature appears to experience a similar rise in both models, as shown in Figure 101, but this is due to the coolant temperature behavior. In Figure 102(a), we observe that the Pronghorn/Griffin model experiences a slightly larger coolant density change than does the SAM/Griffin model, and this is driven by the power response and modeling of the primary loop. This becomes apparent when examining Figure 102(b). The coolant inlet temperature in the Pronghorn value is constant, since it relies on a boundary condition—whereas the SAM model relies on recirculation of the coolant through the primary system. We observe that the core inlet temperature would increase as the power increases, and reach its highest value at t = 100 seconds, thus contributing to the power fluctuation at 100 seconds that is observed in the SAM/Griffin model (Figure 99). This transient exemplifies the tight coupling of the various feedback physics for this reactor design, as well as the many negative feedback mechanisms available. In addition, the predicted maximum fuel temperatures are below 1400 K—well below the historical limit of 1873.15 K (1600°C).

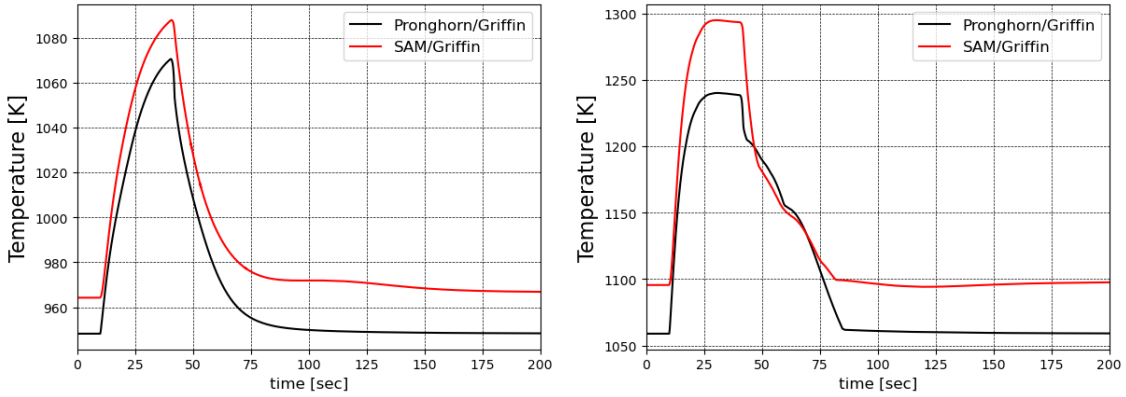

(a) Volume-average (b) Maximum

Figure 101. Comparison between Pronghorn/Griffin and SAM/Griffin in regard to the volume-averaged and maximum moderator temperatures predicted for the control rod movement accident.

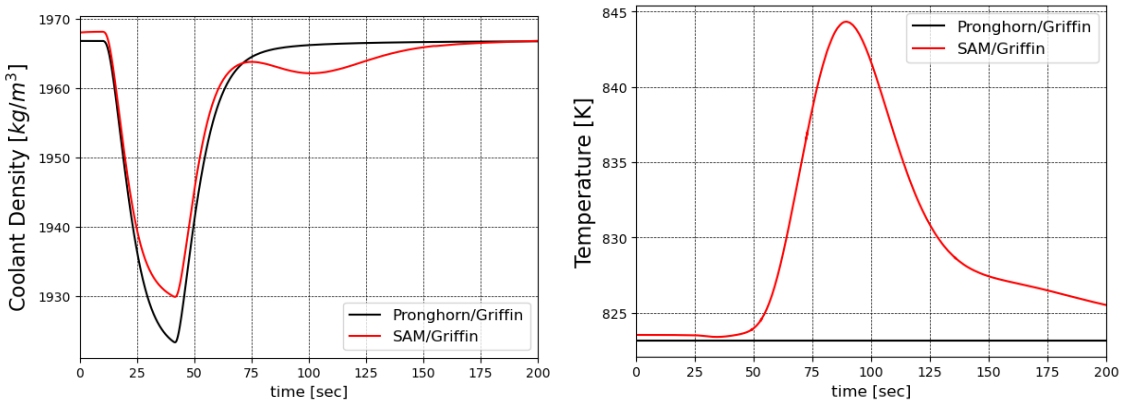

(a) Volume-average coolant density

(b) Coolant inlet temperature

Figure 102. Comparison between Pronghorn/Griffin and SAM/Griffin in regard to the volume-averaged coolant density and inlet fluid temperature predicted for the control rod movement accident.

3.5. Control Rod Movement Accident Scenarios - 3-D/2-D/0-D Simulation

This section focuses on comparing the 3-D reference model to the equivalent 2-D and 0-D/PKE models. Section 3.5.1 provides an in-depth analysis of the delayed supercritical scenario, while Section 3.5.2 is dedicated to analysis of the prompt supercritical scenario. We encountered significant challenges in developing a 0-D/PKE model that can replicate the solutions from the 3-D reference. This task was somewhat simplified for the 2-D model, though it was heavily ”tuned” to produce solutions consistent with the 3-D model. The analysis further confirms that both the 0-D and 2-D models must be informed by a higher-fidelity model—preferably one coupled to a thermal fluids code—to achieve similar predictive capability.

3.5.1. Delayed Supercritical Transient

This delayed supercritical transient was intentionally designed to introduce reactivity in a very short period of time: precisely 0.85 seconds. Although this scenario is not physically realistic, as it neglects the maximum withdrawal speed of the control rod drive mechanism, it is crucial for evaluating the behavior of delayed neutrons in the PB-FHR. In this scenario, delayed neutrons limit the rates of both power ascent and descent.

As outlined in the control rod withdrawal event sequence in Table 6, the rods are rapidly withdrawn at 10–10.85 s, held in place from 10.85 to 22 seconds, and finally reinserted to their initial position over 2 seconds (from 22 to 24 s).

The time evolution of the power and power peak is depicted in Figure 103. The 3-D and 2-D equivalent models exhibit similar power behavior during the event. However, the first 0-D/PKE model, based on static and dynamic reactivity predictions without feedback, overpredicts the rise in power. Adjusting the reactivity insertion to match the 3-D power results in a maximum value closer to the 3-D model, but the power response remains dissimilar. This indicates that the linear combination reactivity model is inadequate for this reactor type.

The ultimate goal for the predictive capability is to reproduce this power curve by using the static reactivity insertion value, indicating that improvements to the feedback reactivity model are needed. The power peak for the transient is defined as the maximum pebble power during the transient, divided by the average pebble power in the steady state. The higher resolution in the 3-D model captures the local effects and predicts a peak power of 4.5, whereas the 2-D and PKE models predict a value of 2.1. It is worth noting that the

0-D/PKE model includes partial power fractions from the 2-D steady-state simulation, so it is unsurprising that it predicts a power peak consistent with the 2-D model. Without this inclusion, the peak power value would be significantly different.

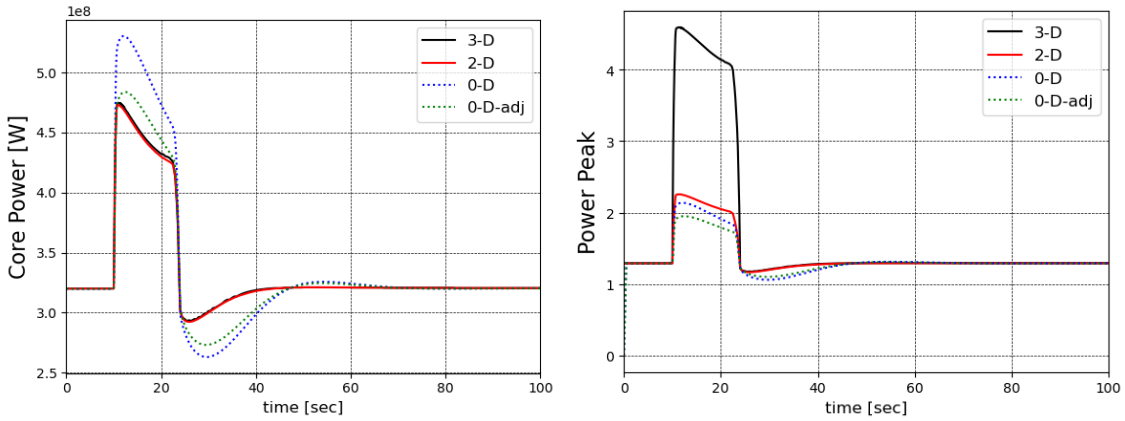

Power Power peak

Figure 103. Power and power peak evolution during a delayed supercritical control rod withdrawal.

Examination of the fuel and moderator temperature responses in Figures 104 and 105 shows that, though the initial temperatures in the 3-D and 2-D models differ by 5 K, the temperature rises in both remain similar during the transient, resulting in comparable power solutions. The original 0-D/PKE model predicts higher temperatures, while the adjusted model approaches the 2-D simulation values. However, the shape of the temperature response in the 0-D/PKE model differs from that in the spatial dynamics models. Similar trends are observed in the coolant density response, with the 0-D/PKE models overestimating the density changes.

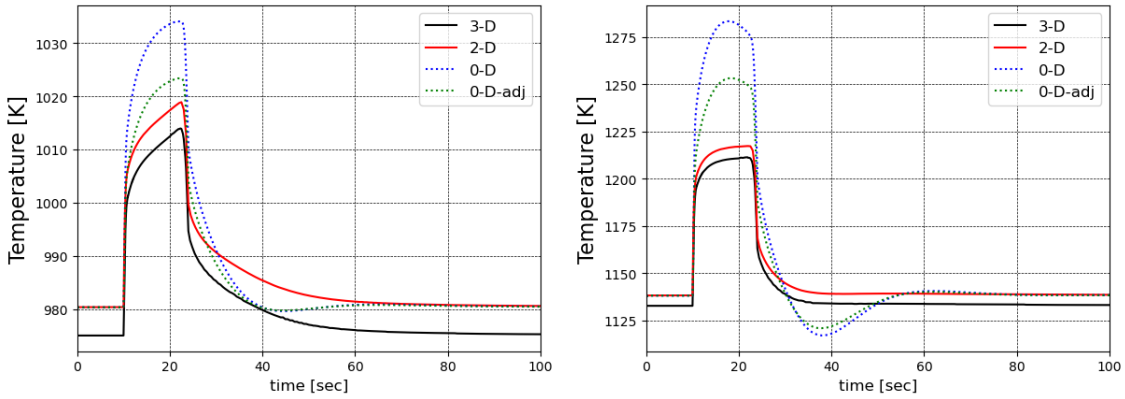

Average Maximum

Figure 104. Fuel temperature evolution during a delayed supercritical control rod withdrawal.

The dynamic reactivity response for all solutions is shown in Figure 107. The 3-D and 2-D models produce consistent solutions, whereas the 0-D/PKE models deviate in terms of both the magnitude and shape of the response. However, this deviation is not significant for this particular transient scenario. Figure 108 provides the time evolution of the various reactivity components for the two 0-D/PKE models. The control rod reactivity is 64 ¢for the nominal case and 52 ¢for the adjusted case. The plots show an early and very strong fuel temperature reactivity feedback, while the moderator temperature and coolant density feedback

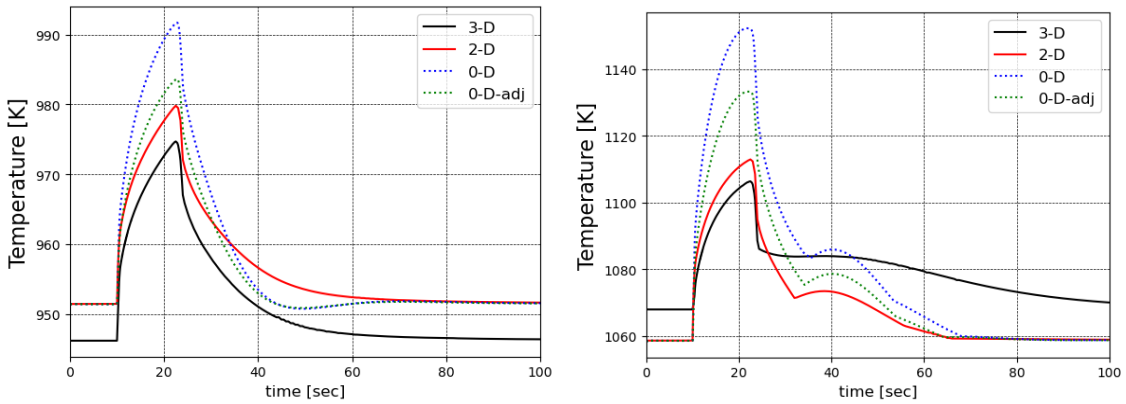

Average Maximum

Figure 105. Moderator temperature evolution during a delayed supercritical control rod withdrawal.

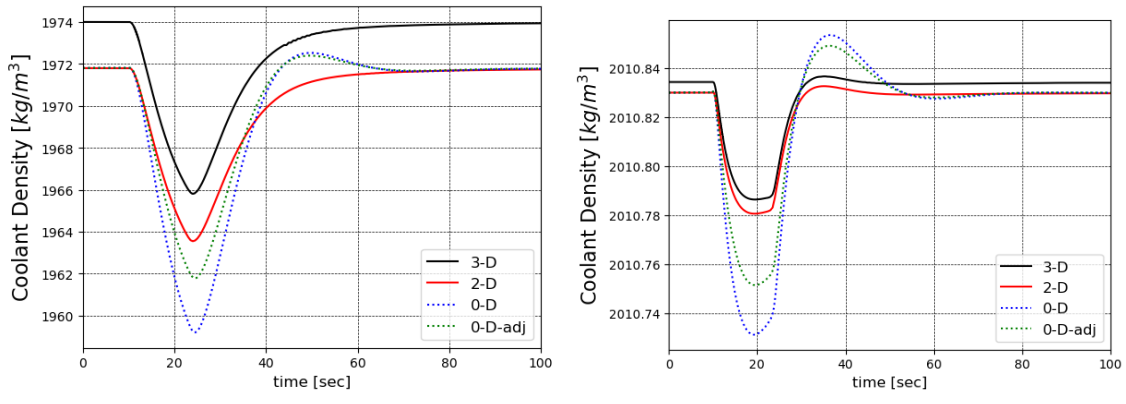

Average Maximum

Figure 106. Coolant density evolution during a delayed supercritical control rod withdrawal.

are much smaller in magnitude as well as delayed in time.

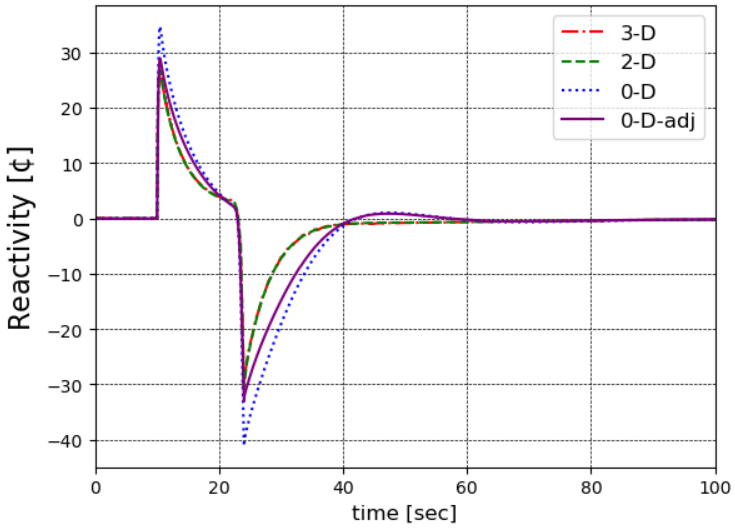

Figure 107. Dynamic reactivity evolution during a delayed supercritical control rod withdrawal.

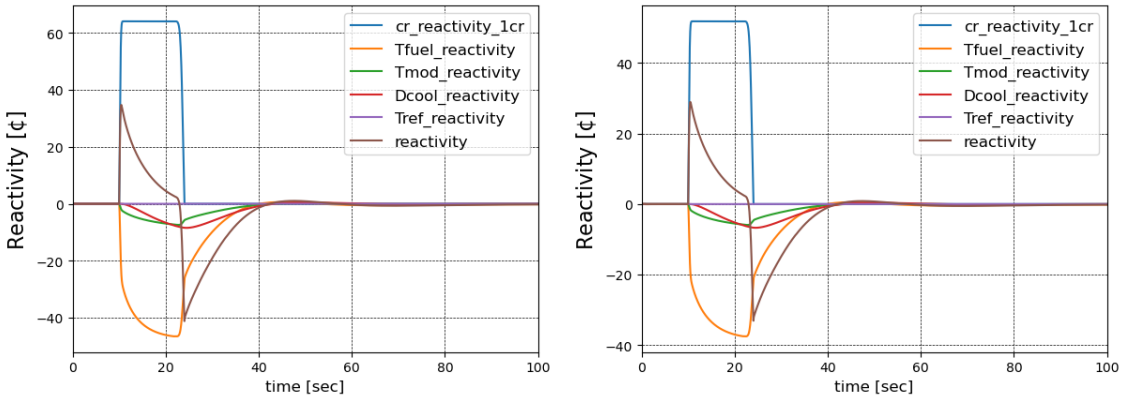

Nominal Adjusted

Figure 108. PKE model reactivity component evolution during a delayed supercritical control rod withdrawal.

Spatial power distributions from the 3-D and 2-D Pronghorn/Griffin simulations are shown in Figure 109. Although the 2-D model includes some spatial information, it cannot capture the power peak from this asymmetric transient. The changes in the power distribution over time for an axial plane at the core bottom (1.9 m) are depicted in Figure 110. It is important to note that a solution with an SN transport solver would display a sharper peak near the reflector zone, as diffusion tends to produce smoother power distributions.

The time evolution of the radial and axial power distributions for the various models are shown in Figures 111 and 112, respectively. The 2-D and 3-D models provide near-identical results, but there are some differences in the 0-D/PKE solutions since the steady-state shape assumed in that model changes during the control rod movement. This is most noticeable at t = 15 s. Similar curves are provided for the radial and axial temperature profiles in Figures 113 and 114, again confirming a similar trend—although the axial temperature distributions maintain the bias longer during the transient, since the energy is not transferred to the coolant until a later time.

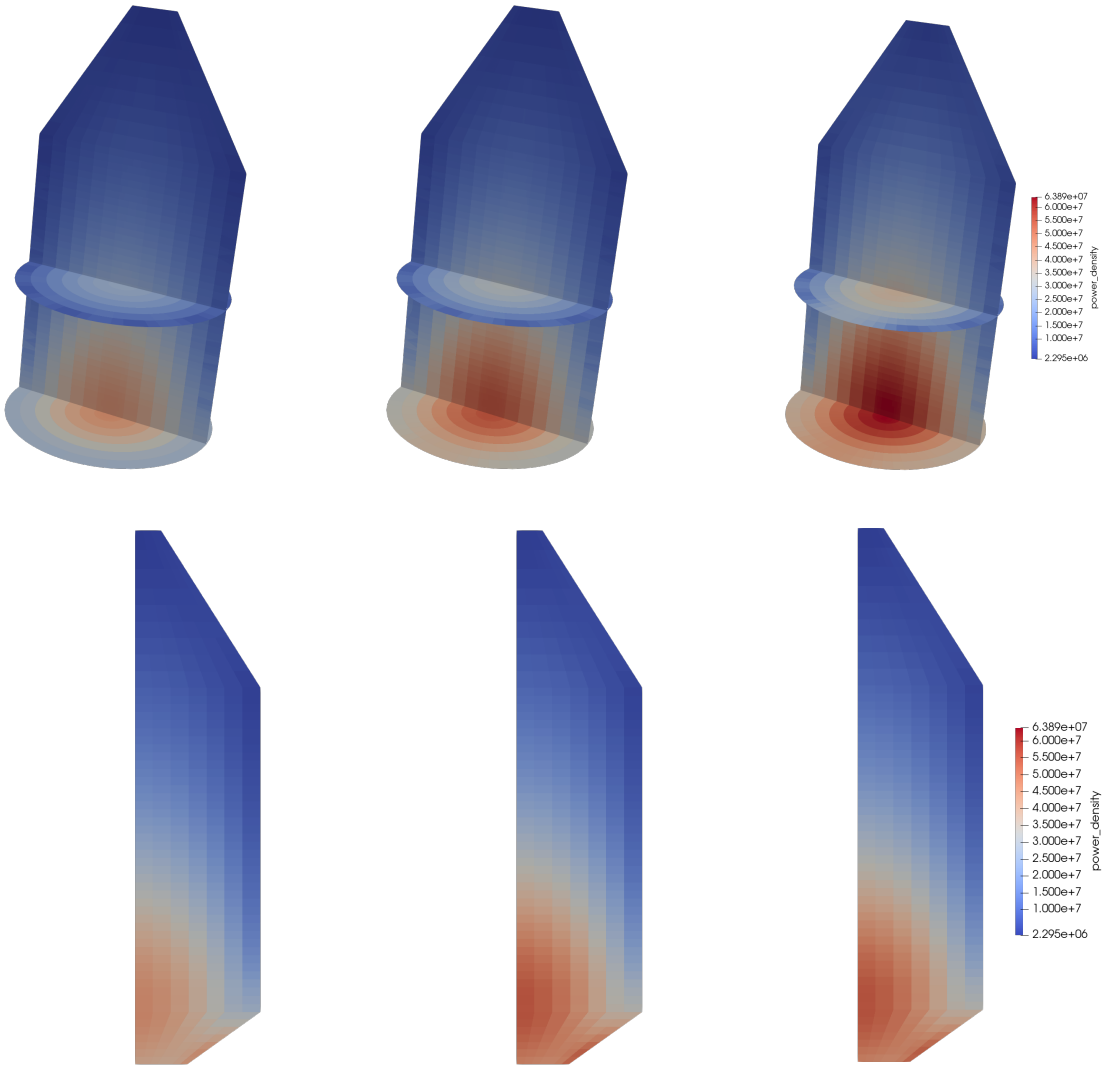

10 sec 10.2 sec 10.95 sec

Figure 109. Power distribution evolution during the delayed supercritical transient (3-D at the top and 2-D at the bottom).

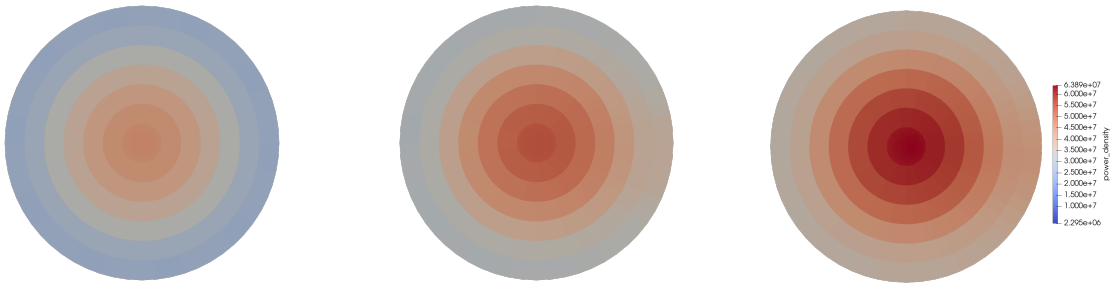

10 sec 10.2 sec 10.95 sec

Figure 110. 3-D power distribution evolution during the delayed supercritical transient Z-plane = 1.9 m.

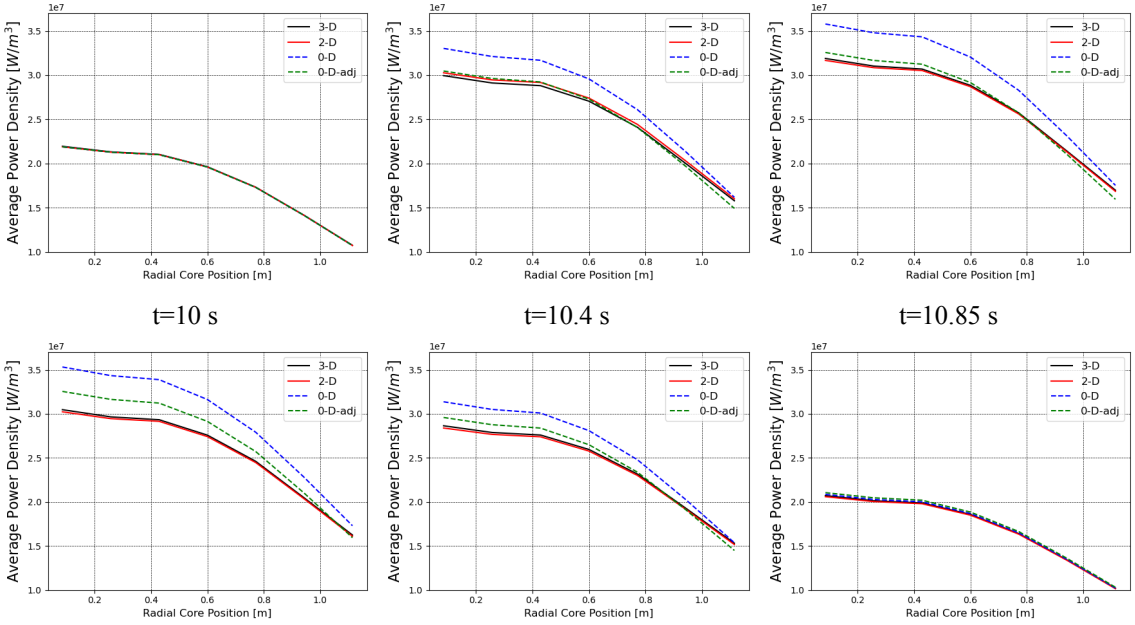

t=10 s t=10.4 s t=10.85 s

t=15 s t=22 s t=24 s

Figure 111. Axially averaged power density during the delayed supercritical control rod withdrawal.

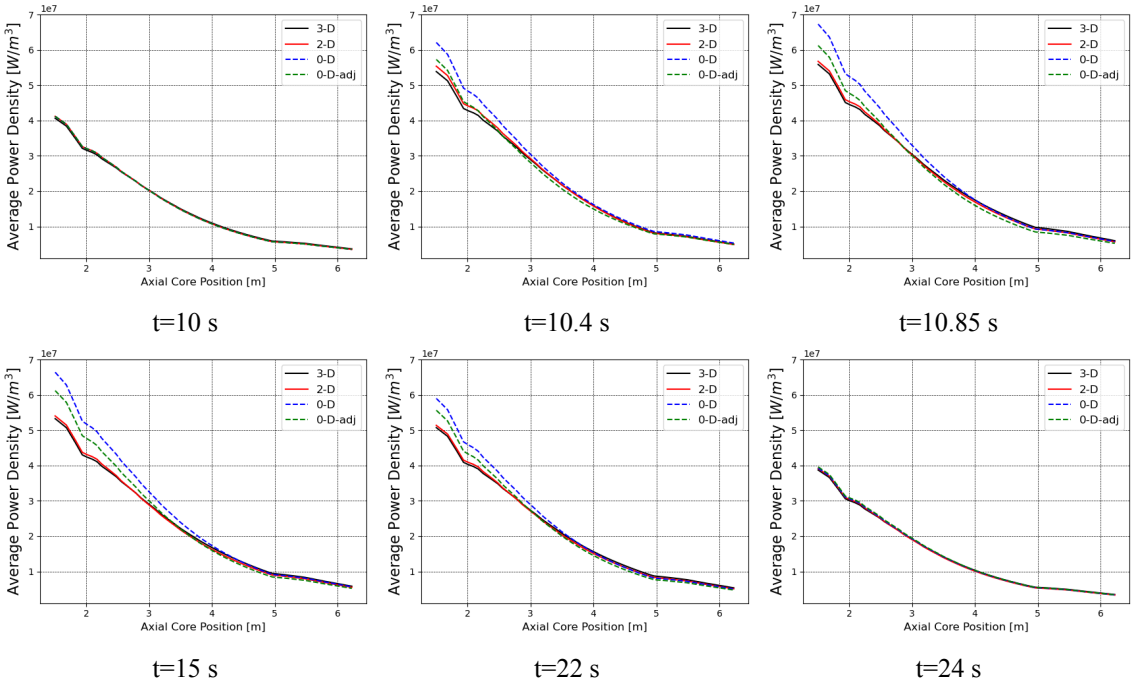

Figure 112. Radially averaged power density during the delayed supercritical control rod withdrawal.

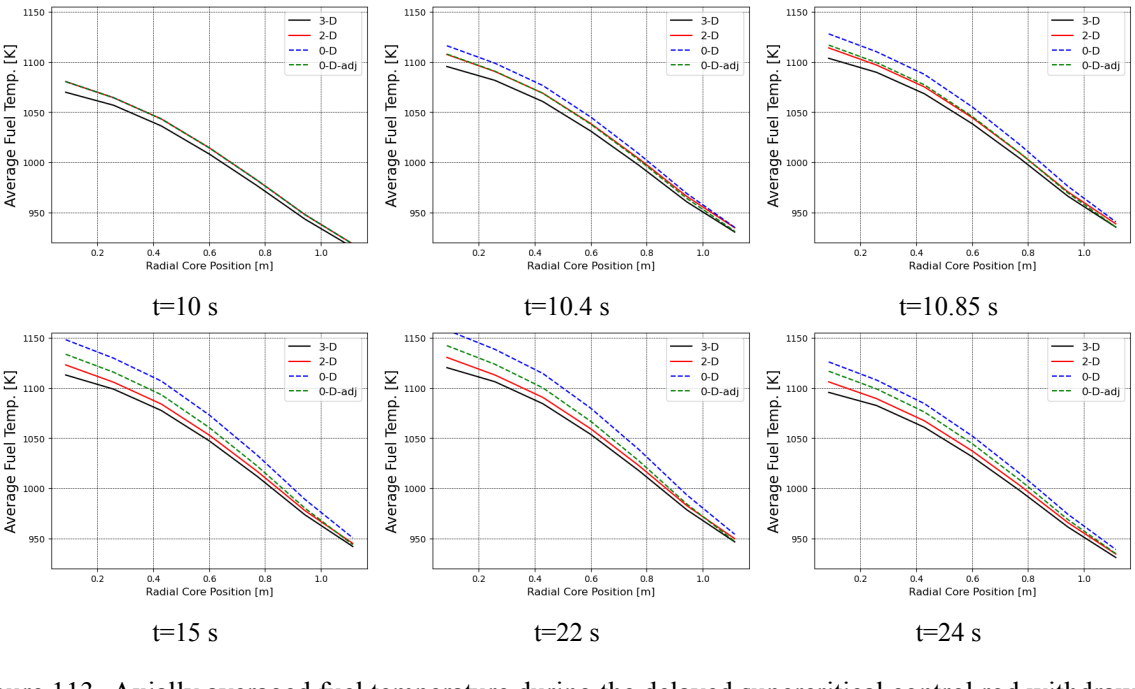

Figure 113. Axially averaged fuel temperature during the delayed supercritical control rod withdrawal.

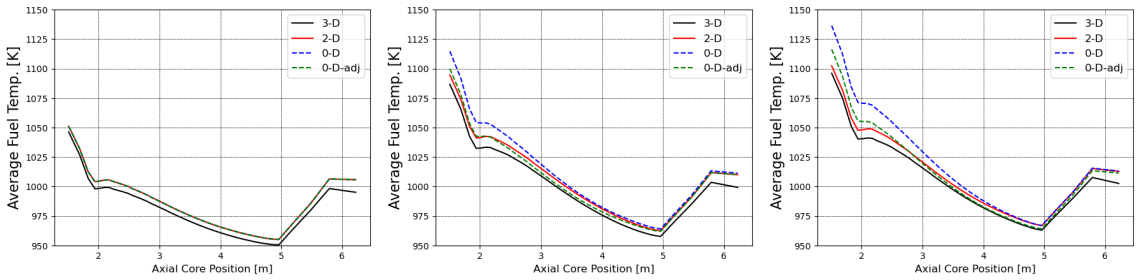

t=10 s t=10.4 s t=10.85 s

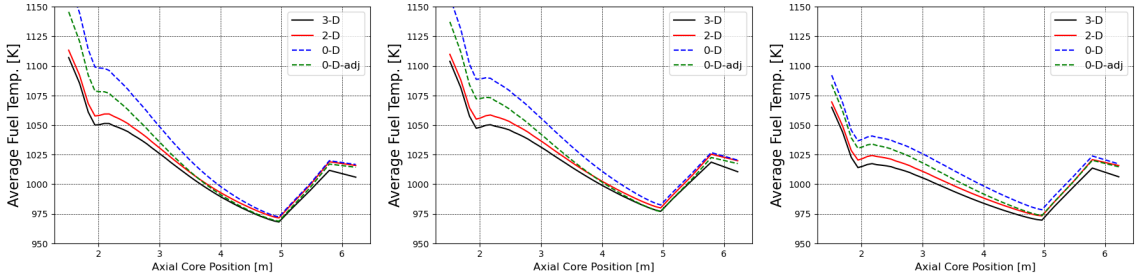

t=15 s t=22 s t=24 s

Figure 114. Radially averaged fuel temperature during the delayed supercritical control rod withdrawal.

3.5.2. Prompt Supercritical Transient

The prompt supercritical transient is more exemplary of this type of control rod withdrawal scenario. Recall from our control rod withdrawal event sequence in Table 7 that the rods are withdrawn from time 10 to 30 seconds, then held in place for 10 seconds, and finally reinserted to their initial position in 2 seconds at 40–42 seconds.

Figure 115 illustrates the time evolution of the power and power peak. In this scenario, with a larger reactivity insertion, some differences begin to emerge between the 3-D and 2-D equivalent models, though these differences are insignificant. They manifest as shifts in the shape of the transient. Similar to the delayed supercritical event, the 0-D/PKE models overpredict the power and exhibit different power evolutions as compared to the 3-D and 2-D solutions. The adjusted PKE model performs better at predicting the initial power increase, but fails to accurately capture the subsequent decrease in power due to various feedback effects. A small power overestimation observed at around 75 s will be explained below, highlighting the need for improvements to the reactivity feedback model.

In this transient scenario, the power peaking predicted by the 3-D model is 7.4, while the 2-D and PKE models predict values closer to 3.0. The shape of the transient response for fuel and moderator temperatures, as well as coolant densities, differs in the 0-D/PKE models, as depicted in Figures 116, 117, and 118. While the solutions for the 3-D and 2-D cases remain very consistent despite their initial differences, the 0-D/PKE model produces different temperature evolutions, resulting in flatter peaks for both the average fuel and moderator temperatures. In contrast, the maximum values are significantly overpredicted in the PKE models, with fuel temperatures exceeding the 3-D and 2-D values by 75–150 K and moderator temperatures by 25–75 K. Notably, the average coolant density response in the 0-D/PKE models tends to overestimate the average density change in the core when the rods are reinserted, thereby contributing to the small power overestimation observed at 75 s.

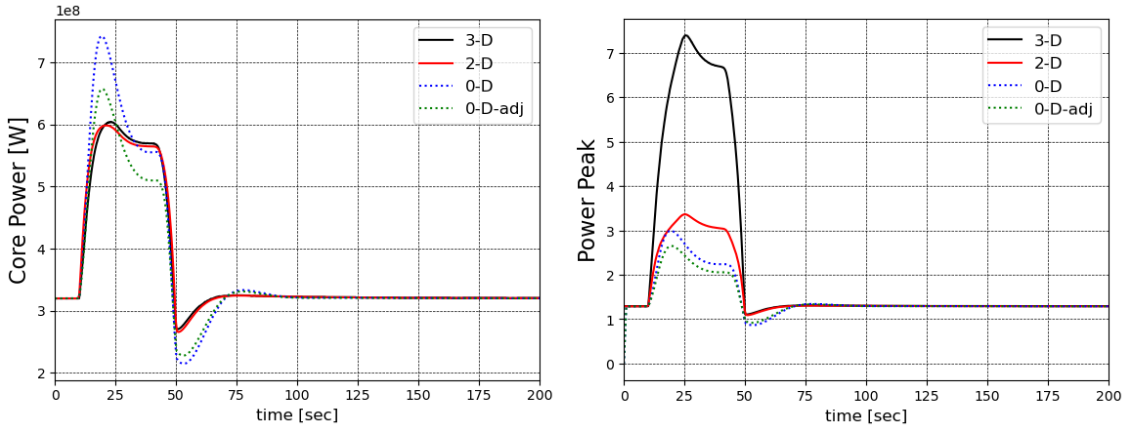

Power Power peak

Figure 115. Power and power peak evolution during a prompt supercritical control rod withdrawal.

The dynamic reactivity for the prompt supercritical event is illustrated in Figure 119. The solutions from the 3-D and 2-D models are consistent, while the 0-D/PKE models exhibit different time responses regarding the initial peak and the subsequent decrease in reactivity, due to various feedback mechanisms prior to the control rods being reinserted. The reactivity changes resulting from the density overshoot in the 0-D/PKE model are particularly evident at between 70 and 75 s.

Figure 120 presents the time evolution of the various reactivity components for the two 0-D/PKE models. The control rod reactivity is 1.52$ for the nominal case and 1.22$ for the adjusted case. The plots again

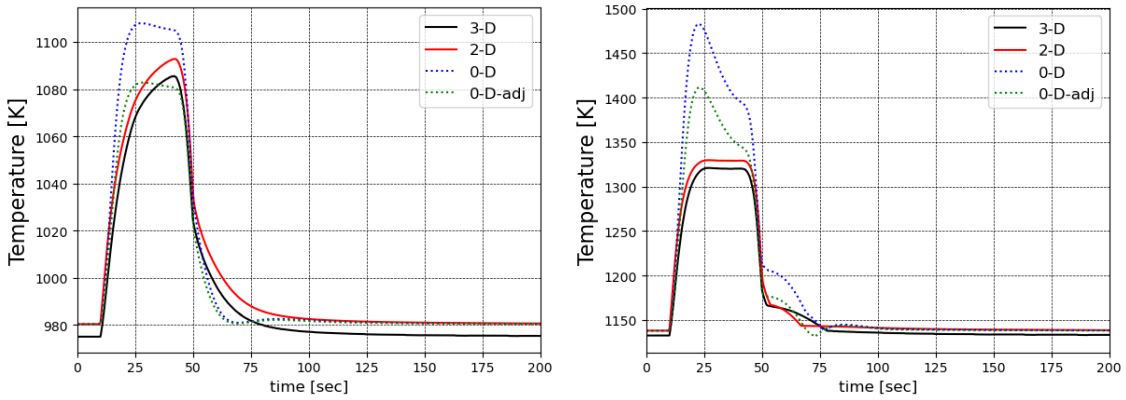

Average Maximum

Figure 116. Fuel temperature evolution during a prompt supercritical control rod withdrawal.

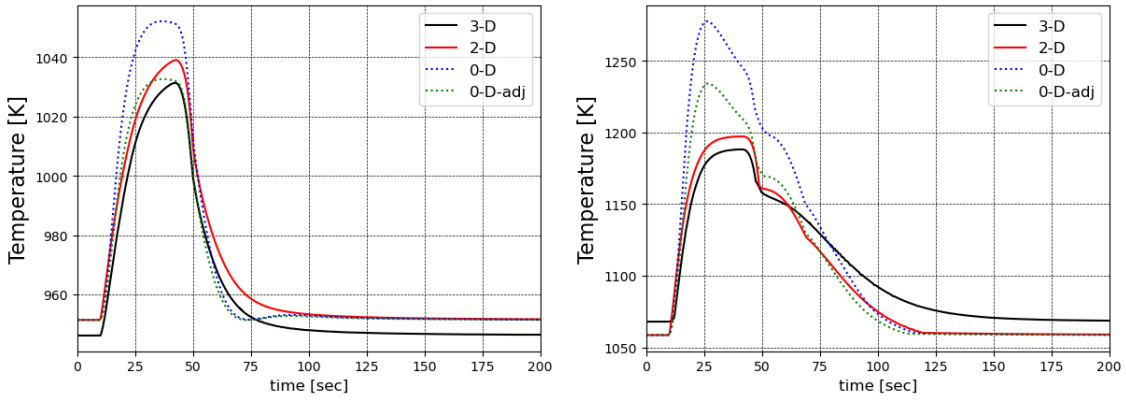

Average Maximum

Figure 117. Moderator temperature evolution during a prompt supercritical control rod withdrawal.

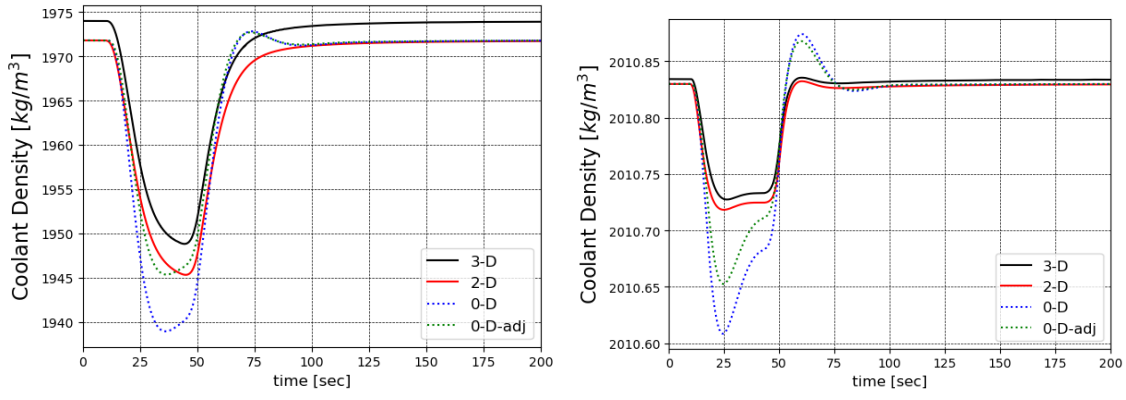

Average Maximum

Figure 118. Coolant density evolution during a prompt supercritical control rod withdrawal.

highlight the early and significant fuel temperature reactivity feedback, while the feedback from the moderator temperature and coolant density is smaller in magnitude and delayed in time. Notably, the shapes and magnitudes of the moderator temperature and coolant density feedback appear to be very similar in this scenario.

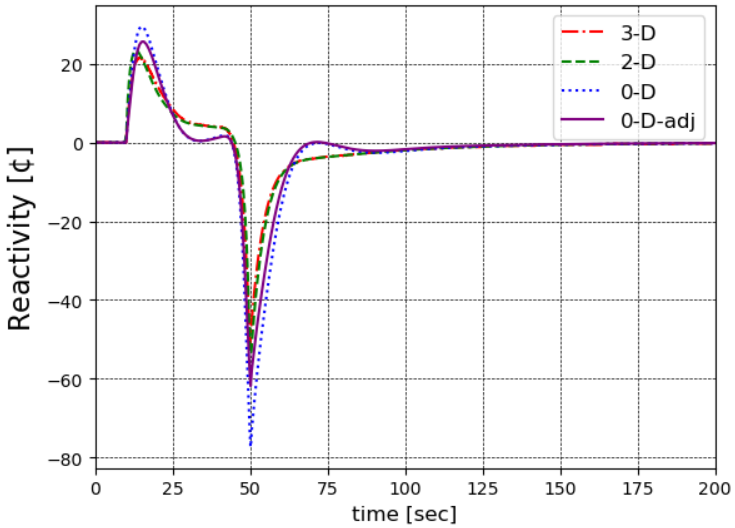

Figure 119. Dynamic reactivity evolution during a prompt supercritical control rod withdrawal.

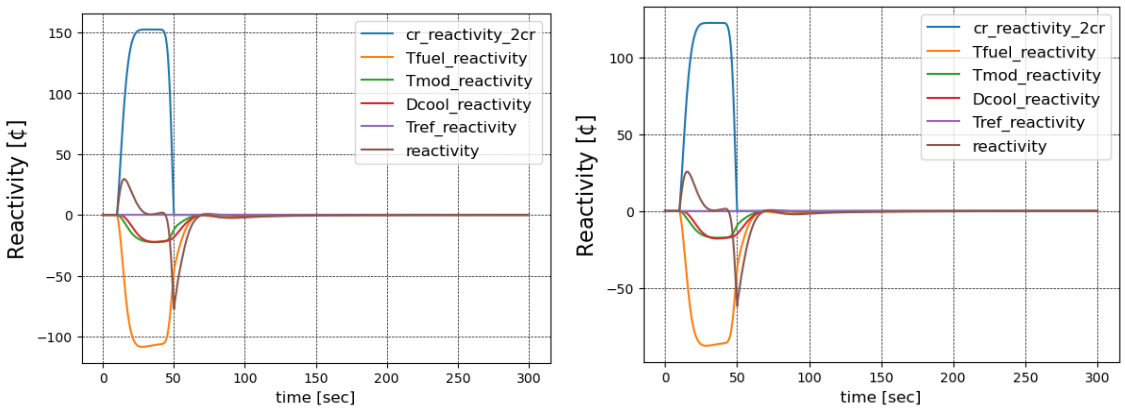

(a) Nominal (b) Adjusted

Figure 120. PKE model reactivity component evolution during a prompt supercritical control rod withdrawal.

Spatial power distributions from the 3-D and 2-D Pronghorn/Griffin simulations are presented in Figure 121. The spatial effects become more pronounced in this scenario, highlighting the limitations of the 2-D model, which fails to capture the power peak generated by this asymmetric transient. This observation is further supported by the axial planes at the core bottom (1.9 m) and at the core center (3.5 m), as shown in Figure 122. In this case, even the diffusion solution reveals differences in the azimuthal distribution of power, which would be even more pronounced with an SN transport solution.

The time evolutions of the radial and axial power distributions for the various models are shown in Figures 123 and 124, respectively. The 2-D and 3-D models yield nearly identical results; however, there are noticeable differences in the 0-D/PKE solutions, due to the steady-state shape assumed in that model

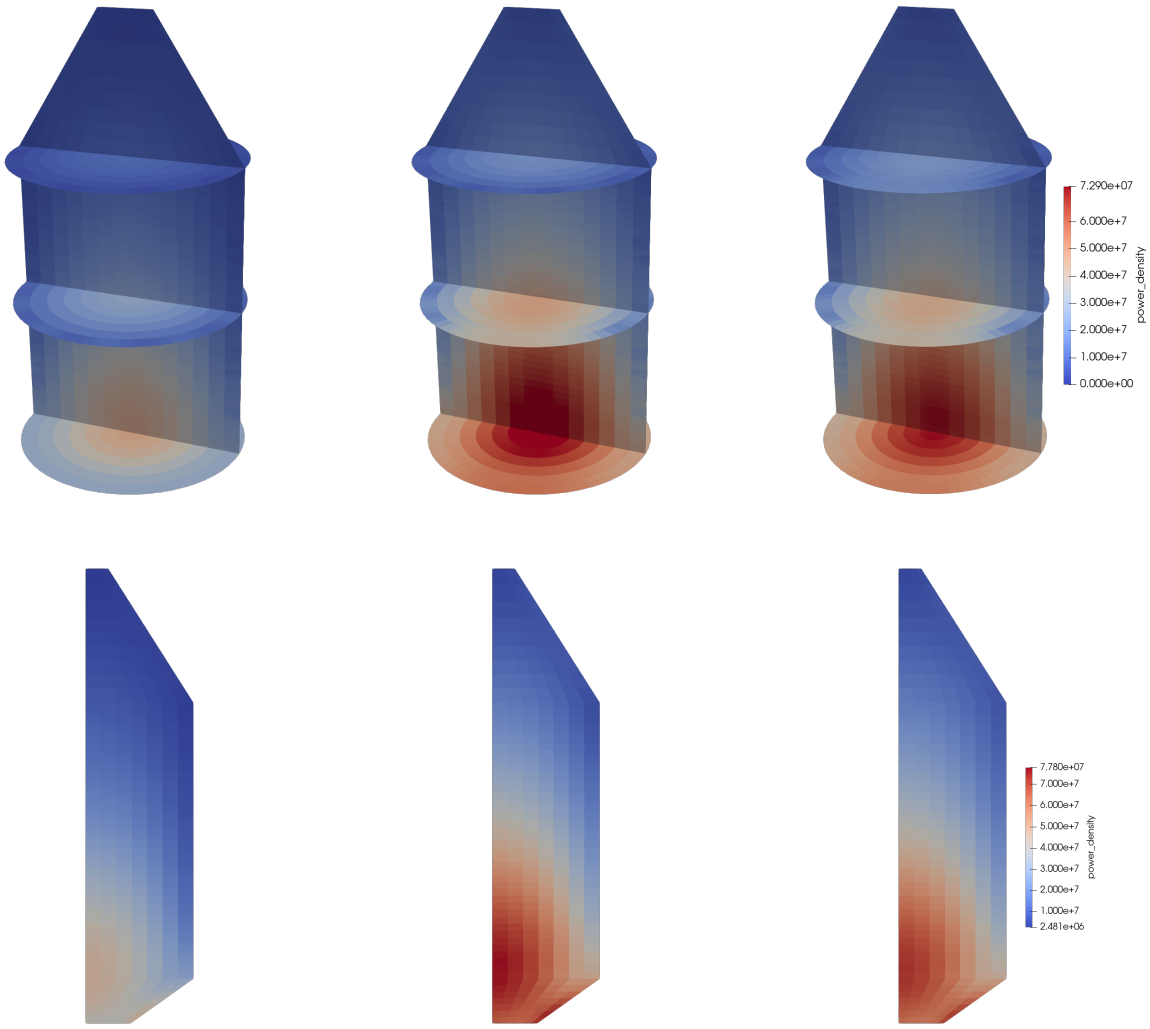

Figure 121. Power distribution evolution during the prompt supercritical transient (3-D at the top and 2-D at the bottom).

changing during the control rod movement. This discrepancy is most apparent at 15 s. Similar curves for the radial and axial temperature profiles are presented in Figures 125 and 126. These figures further confirm a consistent trend, though the axial temperature distributions exhibit a longer-lasting bias during the transient, as energy is not transferred to the coolant until a later time.

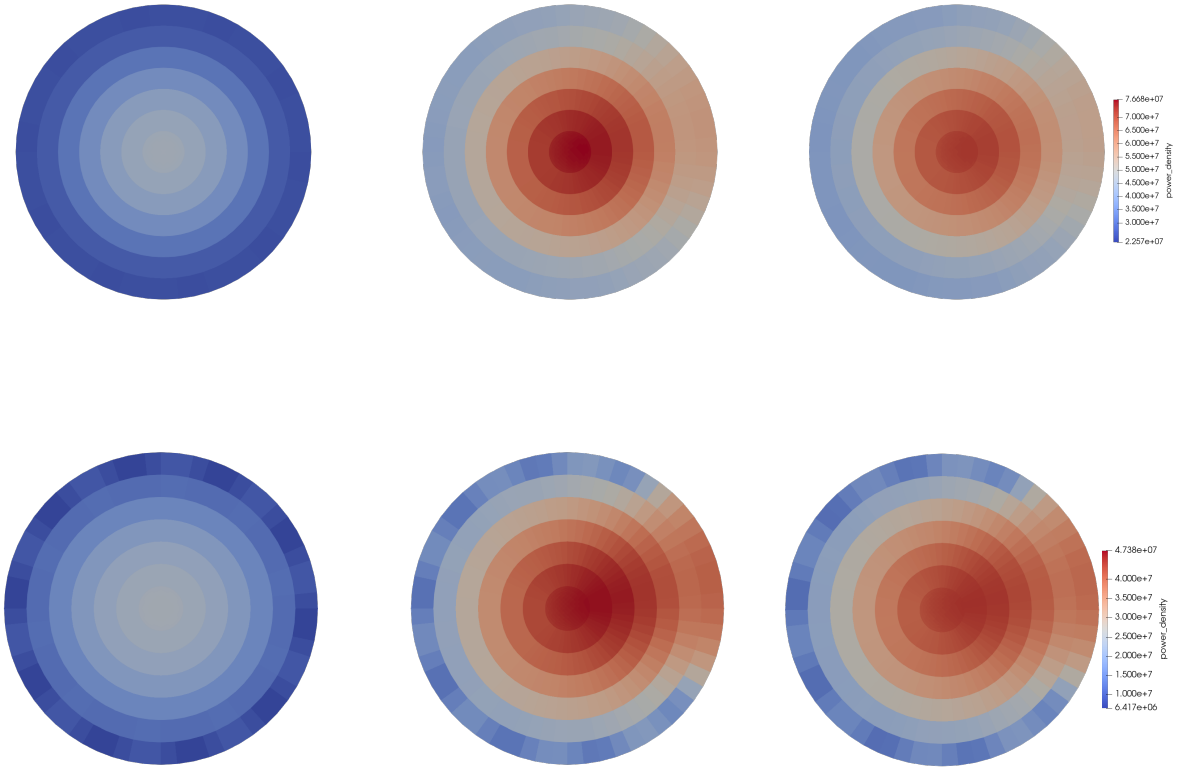

10 sec 20 sec 30 sec

Figure 122. Power density distribution in various axial planes for the 3-D prompt supercritical solution (Z-plane = 1.9 m above and Z-plane = 3.5 m below).

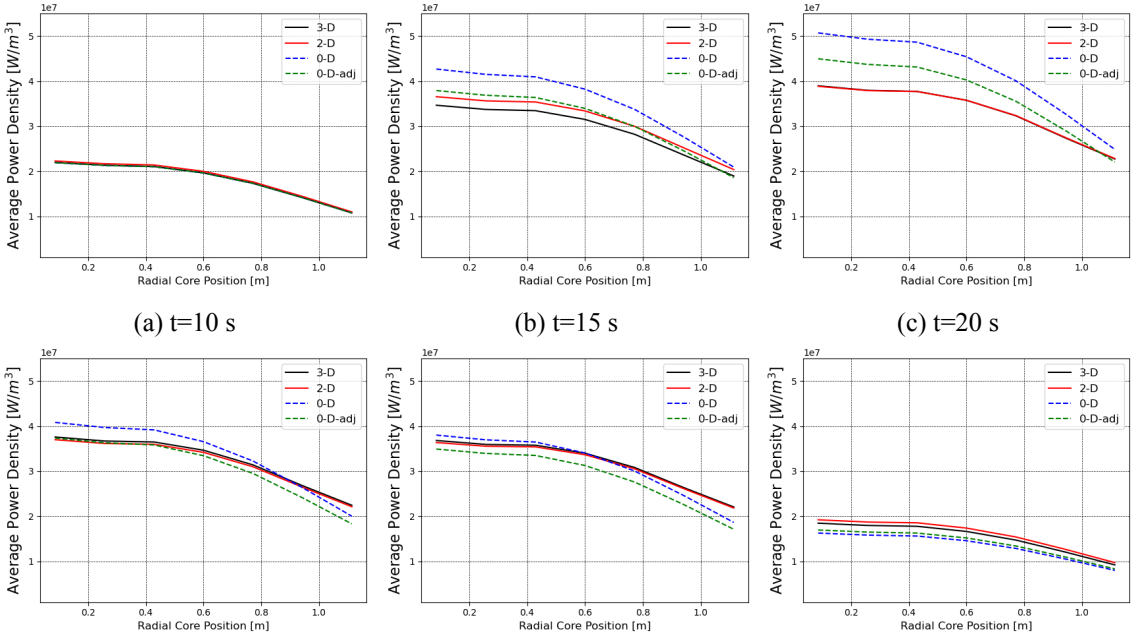

(a) t=10 s (b) t=15 s (c) t=20 s

(d) t=30 s (e) t=40 s (f) t=50 s

Figure 123. Axially averaged power density evolution during a prompt supercritical control rod withdrawal.

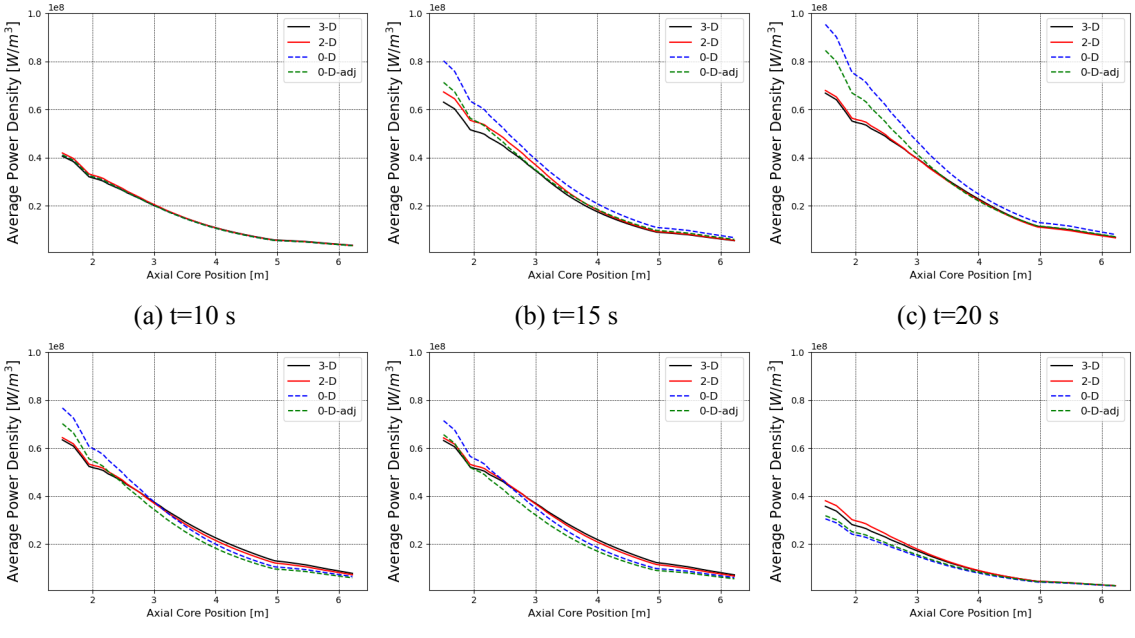

(a) t=10 s (b) t=15 s (c) t=20 s

(d) t=30 s (e) t=40 s (f) t=50 s

Figure 124. Radially averaged power density evolution during a prompt supercritical control rod withdrawal.

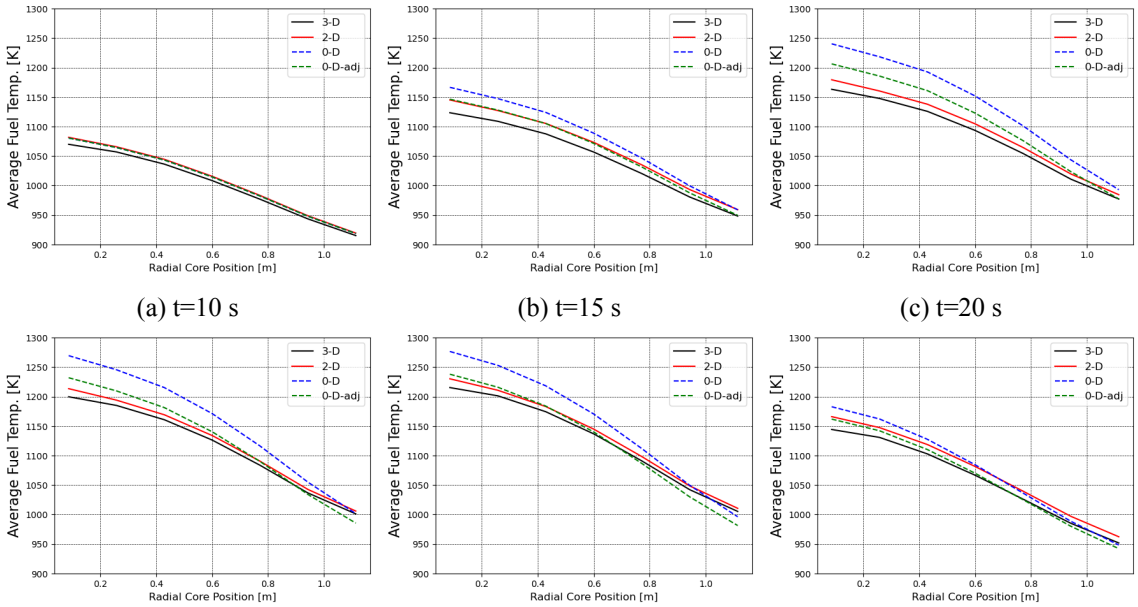

(a) t=10 s (b) t=15 s (c) t=20 s

(d) t=30 s (e) t=40 s (f) t=50 s

Figure 125. Axially averaged fuel temperature evolution during a prompt supercritical control rod withdrawal.

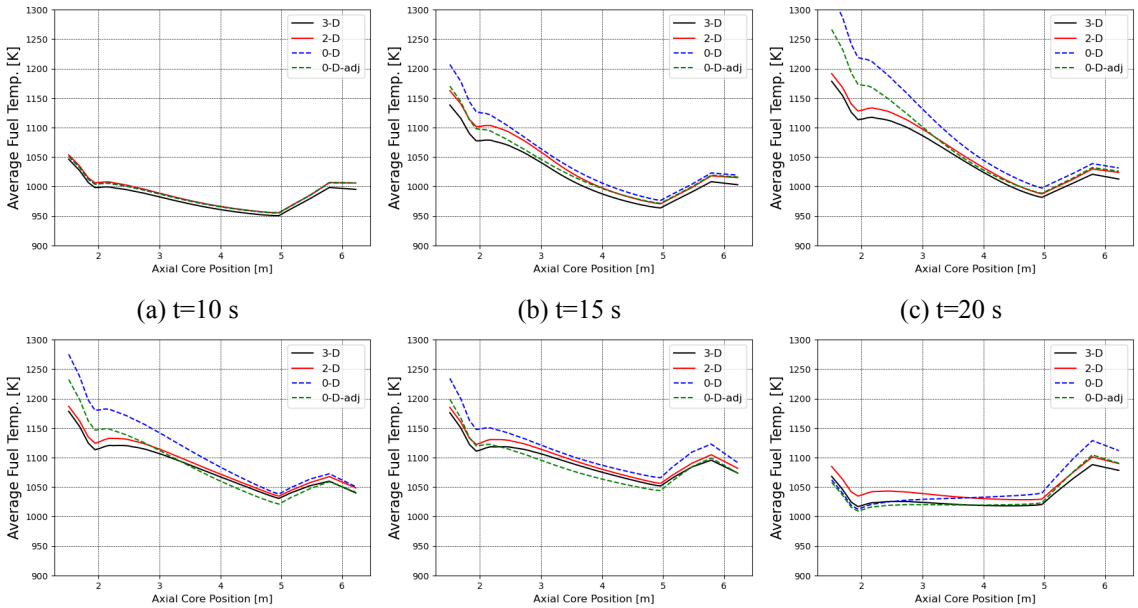

(a) t=10 s (b) t=15 s (c) t=20 s

(d) t=30 s (e) t=40 s (f) t=50 s

Figure 126. Radially averaged fuel temperature evolution during a prompt supercritical control rod withdrawal.

4. DISCUSSION AND CONCLUSION

This work presents improvements to, and investigations performed with, the Fluoride-Cooled High-Temperature Pebble-Bed Reactor reference plant models for the U.S. Nuclear Regulatory Commission (NRC). The reference plant models serve as the foundation for future development of detailed evaluation models based on license applications. The models were built using the Comprehensive Reactor Analysis Bundle (CRAB or alternately BlueCRAB), which is the code suite proposed for non-light-water reactor (non-LWR) systems safety analyses at NRC. BlueCRAB includes the Griffin code for reactor physics, the Pronghorn and SAM codes for core thermal fluids, the BISON code for solid conduction and fuel performance, and the SAM code for system analysis.

The main objective of this work was to assess BlueCRAB's readiness level for modeling fluoride-cooled high-temperature pebble-bed reactors. This was achieved via the following tasks:

- Developing numerical models in BlueCRAB that include the majority of the physics relevant to this technology, thus assuring an adequate level of fidelity for modeling reactor safety performance during accident scenarios.
- Performing comparisons between the thermal fluid porous media models in Pronghorn and SAM with a 2-D geometry for steady state.
- Performing comparisons between coupled Griffin reactor physics and thermal fluid porous media models in Pronghorn and SAM with a 2-D geometry for steady state.
- Performing comparisons between single-solve and domain-overlapping multi-scale thermal fluid coupling approaches for coupling the SAM 2-D porous media core model and SAM 1-D loop model for steady state and a protected loss of forced circulation (PLOFC) transient.
- Performing comparisons between the Pronghorn 2-D porous media core model with boundary conditions and the coupled SAM 2-D porous media core and SAM 1-D loop model for a PLOFC transient.
- Performing comparisons between Pronghorn/Griffin/BC and SAM/Griffin/SAM for the unprotected loss of forced circulation (ULOFC) transient.
- Performing comparisons between SAM/Griffin/SAM and SAM/PKE/SAM models for the ULOFC transient.
- Performing sensitivity analysis for SAM/PKE/SAM model for the ULOFC transient.
- Performing comparisons between Pronghorn/Griffin/BC and SAM/Griffin/SAM for the control rod withdrawal scenario.
- Testing of the 3-D capabilities of the thermal fluid porous media models in Pronghorn.
- Testing of the 3-D capabilities for a coupled model using Griffin and Pronghorn.
- Performing comparison between 3-D, 2-D, and 0-D/PKE models for two control rod withdrawal scenarios: one delayed and one prompt supercritical reactivity insertion.

This work shows that the BlueCRAB models lead to physically intuitive solutions for the scenarios examined. The changes in the various scalar and vector fields (e.g., the neutron flux, power, temperatures, densities, pressures, and velocities) are all within the expected ranges, and their distributions can be explained from the system response during the transients and the geometric and material variations. The steady-state comparison between the standalone SAM and Pronghorn 2-D core thermal-fluids simulations demonstrates good agreement when comparing the predicted solutions. Similar consistency is observed in the coupled SAM/Griffin and Pronghorn/Griffin core models under steady-state conditions. This agreement is expected, as both the SAM and Pronghorn models employ the same set of porous media equations and closure correlations. The differences in solution schemes—a finite volume method in Pronghorn versus a stabilized continuous finite element method in SAM—are not expected to lead to significant discrepancies in the simulation results.

This work compared two multi-scale thermal fluid coupling schemes (i.e., the SAM single-solve and SAM [2-D core]/SAM [1-D system] domain-overlapping approaches) to simulate the full PB-FHR system, which includes a multidimensional porous medium flow model for the core and a 1-D model for the rest of the system. The two coupling schemes were applied to model the full PB-FHR system for two simulations (i.e., steady-state simulation and the PLOFC simulation). The steady-state comparison revealed excellent agreement between the two coupling approaches. The prediction of global parameters such as core mass flow rate, control rod bypass channel flow rate, inlet/outlet plena temperatures, and heat loss to RCCS, and of local parameters such as core radial coolant temperature distributions at different vertical locations, all demonstrated excellent agreement. The PLOFC transient simulation also demonstrated good agreement between the two approaches, based on the comparisons of the global and local parameters used in the steady-state comparison. Some differences were observed in global parameters such as the fluidic diode flow rate, and in local parameters such as the temperature distributions near the core outlet boundary. The difference in the global parameter could be attributed to a possible loss of accuracy when the domain-overlapping scheme is applied to natural circulation simulations. This is something that is planned to be resolved by NEAMS at some point in the near future.

In the analyses of the PLOFC scenario, both SAM/Griffin/SAM and Pronghorn/Griffin/BC predicted that the RCCS could adequately remove decay heat following reactor shutdown. Overall, the two simulations exhibited similar trends in the RCCS heat removal rates. For the ULOFC scenario, both SAM/Griffin/SAM and Pronghorn/Griffin/BC predicted that the reactor would reach a near-shutdown state during the transient with internal reactivity feedback mechanisms. The two simulations exhibited similar reactor power trends. Nevertheless, due to different modeling assumptions in the primary loop, pump coastdown models, and RCCS models when comparing two sets of simulations, Pronghorn/Griffin/BC predicted a more rapid drop in power at the beginning of the transient. A more consistent comparison can be performed once the remaining domain-overlapping coupling scheme issue between the Pronghorn 2-D core porous media model and the SAM 1-D loop model is resolved by the NEAMS program in the near future.

In analyzing the control rod withdrawal events, we determined that the coupled 2-D diffusion model produces similar results as the reference 3-D diffusion model. Overall, the 0-D/PKE results are reasonably close to those from the reference 3-D model, but exhibit evident differences in the time evolution of the solution. We encountered difficulties in determining what precise control rod reactivity insertion value for the PKE models would be equivalent to those in the 3-D and 2-D models. This indicates that either the feedback model requires further improvement or that the procedure used in determining the value of the reactivity inserted requires further review. It is noteworthy that the reduced-order models were developed from the 3-D diffusion model and therefore do not constitute a credible predictive capability outside the evaluated transients. The wall time for 3-D, 2-D, and 0-D/PKE Griffin-Pronghorn calculations for the control rod transients are on the order or 3–20 hours, 0.15–3 hours, and 0.1–0.5 hours, respectively.

In conclusion, this study demonstrates that BlueCRAB shows a satisfactory level of readiness for modeling Fluoride-Cooled High-Temperature Pebble-Bed Reactors. The results for this PB-FHR design indicate there is ample safety margin, based on the specifications, assumptions, and approximations applied in our models. While the results are promising, it is important to recognize that validation of the BlueCRAB codes used in developing the reference plant models and conducting the analyses remains an area for future work. It should be emphasized that the objective of this study was not to validate BlueCRAB or perform a detailed safety analysis, but rather to assess its current applicability and readiness for modeling this type of reactor technology.

5. FUTURE WORK

In addition to demonstrating that BlueCRAB has achieved a satisfactory readiness level for modeling Fluoride-Cooled High-Temperature Pebble-Bed Reactors, this work also identified several areas for potential

code improvements and refinement, and these areas are recommended for consideration by the NEAMS program. Furthermore, various aspects of the current models could be enhanced when updating the reference plant models with detailed design information in support of NRC licensing activities. Below are suggested areas for model refinement, for NRC's consideration.

Suggested refinement areas for the neutronics model:

- Run neutron transport—as opposed to diffusion—for the control rod withdrawal events. This requires a higher-fidelity control rod model but should better approximate the power peak that occurs during the event.
- Develop a Monte Carlo reference model to verify the Griffin solution. Currently, we have a Serpent model with fresh fuel. We recommend developing an equilibrium core model.
- Deploy Griffin-based online cross section preparation, neutron streaming and leakage correction.
- Deploy a better neutron energy group structure.
- Deploy gamma heating of structures and components.
- Deploy the Griffin calculation of the fuel burnup in FIMA.
- Deploy improved fluence calculations or radiation damage models of structures and components.
- Move to fully correlated reactivity PKE models with either surrogate models or the calculation of local coefficients of reactivity.
- Include FLiBe density feedback in the control rod model.
- Calculate Li-6 depletion and tritium production in the FLiBe coolant.
- Deploy macroscopic cross sections for transients with poison (Xe and Sm chains) tracking and a PBR decay heat model.
- Assess the impact of using a constant versus a steady-state shape when calculating reactivity coefficients.

Suggested refinement areas for the thermal fluids model are as follows:

- Improve and finalize the overlapping domain coupling methodology between SAM and Pronghorn.
- Initiate coupling with BISON fuel performance models to determine the fraction of particle failures, based on transient results. Correlate that to the TRISO power and pebble surface temperature. Determine fission product migration from TRISO to graphite, along with graphite retention characteristics.
- Obtain the latest material properties for FLiBe, UCO, SiC, and various graphite materials from DOE programs for the NRC evaluation models.
- Integrate the calculation of the pebble and TRISO thermophysical properties in BISON with the Pronghorn pebble conductivity model. Determine the optimal effective conductivity calculation for the fuel layer in the pebble and the pebble as a whole.
- Perform a comparison between the SAM multiscale pebble model and the coupled BISON/Pronghorn 1-D pebble and TRISO model. Apply the same BISON/Pronghorn 1-D pebble and TRISO model in SAM simulations to evaluate the tradeoff between the two different pebble modeling approaches during transients.
- Perform a mesh sensitivity study in SAM and Pronghorn 2-D porous media models.
- Modify thermal properties in the control rod channel, based on control rod position.
- Deploy a control rod and fluidic diode compatible model in Pronghorn 2-D.
- Perform consistent simulations between the Pronghorn/Griffin and SAM/Griffin LOFC models with consistent boundary conditions or modeling assumptions.
- Improve barrel and vessel temperature models.
- Add a gamma heating source to structures and components from the Griffin calculation.
- Develop a multi-channel core model in SAM, and compare the performance with the 2-D porous medium models. Compare the performance of the multi-channel model with PKE to the 2-D porous medium model and 2-D spatial kinetics model for selected reactor transients.

- Improve the secondary loop model with the steam generator component included.
- Develop an alternative RCCS model without the cooling of the water loop and simulate the boil-off scenario.

Some events that may be of interest, and where 2-D or 3-D modeling can provide important insights, are as follows:

- LOFC with delayed trip actuation from RPS
- ULOFC with better neutron sources to improve predictions of re-criticality
- Reactivity insertion events with concurrent pump trip
- Asymmetric flow blockage
- Seismic event
- Loss of ultimate heat sink
- Increase in heat removal (overcooling).

6. REFERENCES

[1] Satvat, N., Sarikurt, F., Johnson, K., Kolaja, I., Fratoni, M., Haugh, B., and Blandford, E. (2021) Neutronics, thermal-hydraulics, and multi-physics benchmark models for a generic pebble-bed fluoride-salt-cooled high temperature reactor (FHR). *Nuclear Engineering and Design,* **384**, 111461.

[2] Kairos Power LLC, Hermes Non-Power Reactor Preliminary Safety Analysis Report. Technical Repor HER-PSAR-001, Non-proprietary (2021).

[3] Zhao, H., Fick, L., Heald, A., Zhou, Q., Richesson, S., Sutton, N., and and, B. H. (2023) Development, Verification, and Validation of an Advanced Systems Code KP-SAM for Kairos Power Fluoride Salt–Cooled High-Temperature Reactor (KP-FHR). *Nuclear Science and Engineering,* **197**(5), 813–839.

[4] EPRI, Uranium Oxycarbide (UCO) Tristructural Isotropic (TRISO) Coated Particle Fuel Performance: Topical Report EPRI-AR-1(NP). Research Report 3002019978, Electric Power Research Institute (2020).

[5] Hasting, P. (2022) Presentation Materials for Kairos Power Briefing to the Advisory Committee on Reactor Safeguards, Kairos Power Subcommittee, on Design Overview for the Hermes Non-Power Reactor. In *KP-NRC-2204-007* Kairos Power LLC.

[6] Chrono, P. Chrono: An Open Source Framework for the Physics-Based Simulation of Dynamic Systems. http://projectchrono.org Accessed: 2016-03-07.

[7] Leppänen,, J. Development of a New Monte Carlo Reactor Physics Code PhD thesis Helsinki University of Technology (2007).

[8] Kairos Power LLC, Postulated Event Analysis Methodology. Technical Repor KP-TR-018-NP, Non-proprietary (2021).

[9] Wang, Y., Prince, Z. M., Park, H., Calvin, O. W., Choi, N., Jung, Y. S., Schunert, S., Kumar, S., Hanophy, J. T., Labouré, V. M., Lee, C., Ortensi, J., Harbour, L. H., and Harter, J. R. (2025) Griffin: A MOOSE-based reactor physics application for multiphysics simulation of advanced nuclear reactors. *Annals of Nuclear Energy,* **211**, 110917.

[10] Novak, A., Carlsen, R., Schunert, S., Balestra, P., Reger, D., Slaybaugh, R., and Martineau, R. (2021) Pronghorn: A Multidimensional Coarse-Mesh Application for Advanced Reactor Thermal Hydraulics. *Nuclear Technology,* **207**, 1015–1046.

[11] Williamson, R. L., Hales, J. D., Novascone, S. R., Pastore, G., Gamble, K. A., Spencer, B. W., Jiang, W., Pitts, S. A., Casagranda, A., Schwen, D., Zabriskie, A. X., Toptan, A., Gardner, R., Matthews, C., Liu, W., and and, H. C. (2021) BISON: A Flexible Code for Advanced Simulation of the Performance of Multiple Nuclear Fuel Forms. *Nuclear Technology,* **207**(7), 954–980.

[12] Hu, R., Zou, L., O'Grady, D., Mui, T., Ooi, Z. J., Hu, G., Cervi, E., Yang, G., Andrs, D., Lindsay, A., Permann, C., Salko, R., Zhou, Q., Fick, L., Heald, A., and and, H. Z. (2024) SAM: A Modern System Code for Advanced Non-LWR Safety Analysis. *Nuclear Technology,* **0**(0), 1–20.

[13] Choi, N., Hanophy, J., Wang, Y., Chase, B., and Ortensi, J., "Griffin Capability Improvements in Support of Ex-core Deep-Penetration Problems". "Report" "INL/RPT-25-85358", Idaho National Laboratory (INL), Idaho Fallse, ID (United States) ("June", "2025").

[14] Blacker, T. D., Owen, S. J., Staten, M. L., Quadros, W. R., Hanks, B., Clark, B. W., Meyers, R. J., Ernst, C., Merkley, K., Morris, R., McBride, C., Stimpson, C. J., Plooster, M., and Showman, S. CUBIT Geometry and Mesh Generation Toolkit 15.1 User Documentation (2016).

[15] Sjaardema, G. D., Schoof, L. A., and Yarberry, V. R. EXODUS: A Finite Element Data Model Sandia National Laboratories (2008).

[16] Hébert, A. (2013) DRAGON5: designing computational schemes dedicated to fission nuclear reactors for space. *Proceedings of Nuclear and Emerging Technologies for Space,* **25**.

[17] Hansol Park, C. L. (2025) Extension of TRISO Double Heterogeneity Treatment in Griffin to Spherical Shell Geometry for Fluoride Salt-cooled Pebble Bed Reactor. In *M&C 2025 April 27–30, 2025, Denver, CO*.

[18] Ortensi, J., Mueller, C. M., Terlizzi, S., Giudicelli, G. L., and Schunert, S. (5, 2023) Fluoride-Cooled High-Temperature Pebble-Bed Reactor Reference Plant Model. ,.

[19] Lieberoth, J. and and, A. S. (1980) Neutron Streaming in Pebble Beds. *Nuclear Science and Engineering,* **76**(3), 336–344.

[20] Benoist, P. (1968) Streaming Effects and Collision Probabilities in Lattices. *Nucl. Sci. Eng.,* **34**, 285–307.

[21] Ortensi, J. and Balestra, P. (2022) Initial study on cross-section generation requirements for a PBR equilibrium core. In *PHYSOR 2022, Making Virtual a Reality - Advancements in Reactor Physics To Leap Forward Reactor Operation and Deployment*.

[22] Pomraning, G. C. (1984) Flux-Limited Diffusion Theory with Anisotropic Scattering. *Nuclear Science and Engineering,* **86**(4), 335–343.

[23] Kadak, A. C. and Bazant, M. Z. (2004) Pebble Flow Experiments For Pebble Bed Reactors. In *2nd international topical meeting on high temperature reactor technology, Beijing, China, 2004*.

[24] Kairos Power LLC, Reactor Coolant for the Kairos Power Fluoride Salt- Cooled High Temperature Reactor. Technical Repor KP-TR-018-NP, Non-proprietary (2019).

[25] Kairos Power LLC, Scaling Methodology for the Kairos Power Testing Program. Technical Repor KP-TR-018-NP, Non-proprietary (2019).

[26] Zou, L., Hu, G., O'Grady, D., and Hu, R. (2022) Explicit modeling of pebble temperature in the porous-media model for pebble-bed reactors. *Progress in Nuclear Energy,* **146**, 104175.

[27] Gerwin, H., Scherer, W., Lauer, A., and Clifford, I., TINTE. Nuclear calculation theory description report. Technical report, Institute for Energy Research (IEF), Forschungszentrums Jülich (Jan, 2010).

[28] Hu, R., Zou, L., Hu, G., Nunez, D., Mui, T., and Fei, T., SAM Theory Manual. Technical report, Argonne National Lab. (ANL), Argonne, IL (United States) (02, 2021).

[29] Zou, L., O'Grady, D., Hu, G., and Hu, R., Explicit Modeling of Pebble Temperature in the Porous-medium Framework for Pebble-bed Reactors Applications. Technical report, Argonne National Lab.(ANL), Argonne, IL (United States) (2021).

[30] Jaradat, M. K. M., Schunert, S., and Ortensi, J. (4, 2023) Gas-Cooled High-Temperature Pebble-Bed Reactor Reference Plant Model. ,.

[31] Miller, G., Petti, D., Maki, J., Knudson, D., and Skerjanc, W., PARFUME Theory and Model Basis Report. Report INL/EXT-08-14497 (Rev.1), Idaho National Laboratory (September, 2018).

[32] Nabielek, H., Fukuda, K., Minato, K., and Ogawa, T., Calculation of Particle Temperatures in NSRR Tests. Unpublished draft, Japanese Atomic Energy Agency (March, 1992).

[33] Fink, J. K. (2000) Thermophysical properties of uranium dioxide. *Journal of Nuclear Materials,* **279**(1), 1–18.

[34] Lucuta, P., Matzke, H., and Hastings, I. (1996) A pragmatic approach to modelling thermal conductivity of irradiated UO_2 fuel: Review and recommendations. *Journal of Nuclear Materials,* **232**(2-3), 166–180.

[35] Bokros J.C., G.B. Engle, R. J., Research on Graphite. Report GA-9099, General Atomics Corporation (1968).

[36] Olander D. R., Fundamental Aspects of Nuclear Reactor Fuel Elements. Report TID-26711-P1, National Technical Information Service (1976).

[37] General Atomics Corporation, Graphite Handbook. Report DOE-HTGR-88111, (1988).

[38] Nabielek H., Partikeln und Brennelemente für den HTR. Report KFA-HTA, (1991).

[39] Ho F.H. et al., NP-MHTGR Material models of Pyrocarbon and Pyrolityc Silicon Carbide. Report CEGA-002820, Rev 1, General Atomics Corporation (1993).

[40] Snead, L. L. and Nozawa, T. and Katoh, Y. and Byun, T.-S. and Kondo, S. and Petti, D. A. (2007) Handbook of SiC properties for fuel performance modeling. *Journal of Nuclear Materials,* **371**, 329–377.

[41] Gontard, R. and Nabielek, H., Performance Evaluation of Modern HTR TRISO Fuels. Report HTA-1B-05/90, Forschungszentrums Juelich (July, 1990).

[42] Hu, G., Zou, L., O'Grady, D. J., and Hu, R. (2023) An integrated coupling model for solving multiscale fluid-fluid coupling problems in SAM code. *Nuclear Engineering and Design,* **404**, 112186.

[43] Huxford, A., Leite, V. C., Merzari, E., Zou, L., Petrov, V., and Manera, A. (2023) A hybrid domain overlapping method for coupling System Thermal Hydraulics and CFD codes. *Annals of Nuclear Energy,* **189**, 109842.

[44] Huxford, A., Leite, V. C., Merzari, E., Zou, L., Petrov, V., and Manera, A., The Development and Application of a Hybrid Domain Overlapping Coupling between SAM and NekRS. Technical Report Project 20-19864, University of Michigan (2022).

[45] Huxford, A., Zou, L., Hu, R., Petrov, V., and Manera, A. (2024) Validation of a hybrid domain overlapping coupling between SAM and CFD against the TALL-3D transients. *Nuclear Technology,* pp. 1–18.

[46] Zou, L. and Hu, R., Recent SAM Code Improvement to Heat Transfer Modeling Capabilities. Technical Report ANL/NSE-19/46, Argonne National Lab.(ANL), Argonne, IL (United States) (2019).

[47] Zou, L., Hu, G., and Hu, R. (2020) Code Enhancement to SAM Multi-scale/multi-dimensional Heat Transfer Modeling Capabilities. In *American Nuclear Society Virtual Winter Meeting (Chicago, IL, US, 11/16/2020-11/19/2020)*.

[48] Gaston, D. R., Permann, C. J., Peterson, J. W., Slaughter, A. E., Andrš, D., Wang, Y., Short, M. P., Perez, D. M., Tonks, M. R., Ortensi, J., Zou, L., and Martineau, R. C. (2015) Physics-based multiscale coupling for full core nuclear reactor simulation. *Annals of Nuclear Energy,* **84**, 45–54 Multi-Physics Modelling of LWR Static and Transient Behaviour.

[49] Cheng, P. and Hsu, C. (1986) Fully-developed, forced convective flow through an annular packed-sphere bed with wall effects. *International Journal of Heat and Mass Transfer,* **29**(12), 1843–1853.

[50] Wakao, N. and Funazkri, T. (1978) Effect of fluid dispersion coefficients on particle-to-fluid mass transfer coefficients in packed beds: Correlation of sherwood numbers. *Chemical Engineering Science,* **33**(10), 1375–1384.

[51] Yagi, S. and Wakao, N. (1959) Heat and mass transfer from wall to fluid in packed beds. *AIChE Journal,* **5**(1), 79–85.

[52] Van Antwerpen, W., du Toit, C., and Rousseau, P. (2010) A review of correlations to model the packing structure and effective thermal conductivity in packed beds of mono-sized spherical particles. *Nuclear Engineering and Design,* **240**(7), 1803–1818.

[53] Ausschusses, K., K., Reactor Core Design of High-Temperature Gas-Cooled Reactors—Part 3: Loss Pressure Through Friction Pebble Bed Cores. Technical report, Nuclear Safety Standards Commission, Salzgitter, Germany (1981).

[54] Adams, B., Bohnhoff, W., Dalbey, K., Ebeida, M., Eddy, J., M.S., E., Hooper, R., Hough, P., Hu, K., Jakeman, J., et al., Dakota 6.21.0 Documentation. Technical Report SAND2024-154920, Sandia National Laboratories (November, 2024).

[55] Mui, T., Hu, R., and Zhang, G. (2019) Uncertainty Quantification on SAM Simulations of EBR-II Loss-of-Flow Tests. In *International Topical Meeting on Nuclear Reactor Thermal Hydraulics (NURETH-18)*.